Electrospinning des polysaccharides photo-activables : vers des nanomatériaux verts intelligents entraînés par la lumière du soleil

Hamed Ahmadi-Nohadani

THÈSE

Pour obtenir le grade de

DOCTEUR DE L'UNIVERSITÉ GRENOBLE ALPES

École doctorale : CSV- Chimie et Sciences du Vivant
Spécialité : Sciences des Polymères
Unité de recherche : CEntre de Recherche sur les MAcromolécules Végétales

Electrospinning des polysaccharides photo-activables : vers des nanomatériaux verts intelligents entraînés par la lumière du soleil

Electrospinning of Light-Harvesting Polysaccharides: Towards Sunlight-Driven Smart Green Nanomaterials

Présentée par :

Hamed AHMADI NOHADANI

Direction de thèse :

Issei OTSUKA Université Grenoble Alpes	Directeur de thèse

Rapporteurs :

Thomas HEINZE
PROFESSEUR, Friedrich-Schiller- Universität Jena
Tatiana BUDTOVA
DIRECTRICE DE RECHERCHE, Mines Paris Tech

Thèse soutenue publiquement le **16 décembre 2022**, devant le jury composé de :

Issei OTSUKA CHARGE DE RECHERCHE HDR, CNRS délégation Alpes	Directeur de thèse
Thomas HEINZE PROFESSEUR, Friedrich-Schiller- Universität Jena	Rapporteur
Tatiana BUDTOVA DIRECTRICE DE RECHERCHE, Mines Paris Tech	Rapporteure
Kenji TAJIMA PROFESSEUR ASSOCIE, Hokkaido University	Examinateur
Gérard MORTHA PROFESSEUR DES UNIVERSITES, Grenoble INP	Président

To Mom :

Now I understand why you always encouraged me to be strong.

You knew the day would come where I would need the strength to bear your loss…

Acknowledgement

First and foremost, I am humbled to have Drs Thomas Hienze, Tatiana Budtova, Frédéric Bossard, Gérard Mortha, and Kenji Tajima as the jury members of my thesis and I thank them for having accepted this role. I would like to express my deepest gratitude to Dr. Issei Otsuka for his supervision during these three years of hard work. Without his insights and helps, this work would have been undone. Thank you Issei!

I am eternally grateful for the wonderful and beloved family that supports and motivates me. My dear father Dr Syrus Ahmadi-Nohadani, my brother Mahmoud, Maryam, Nafas, and my sweet love Mona.

I would like to extend my gratitude to Drs Gérard Mortha, Michael Holzinger, and Anna Szarpak, my CSI committee members whose helpful ideas and suggestions allowed me to develop a better understanding of the project. My sincere thanks go to Pr. Redouane Borsali for hosting me in A2G group at CERMAV-CNRS and giving me this wonderful opportunity. My thanks to Drs. Anne Imberty, Laurent Heux, and to Mme Isabelle Caldara, the administration board of our lab for their support. I thank Mmes Martine Morales, Sandrine Coindet, Alyssa Arnoux, Mrs Patrick Perez and Laurent Chausse for their technical and logistic support. I equally thank Dr Guy Royal and Mme Magali Pourtier of EDCSV doctoral school of Grenoble Alpes University for their support.

Furthermore, I wish to express my thanks to Sonia Ortega-Murillo (WCA and TGA), Christine Lancelon-Pin (Microscopy), Karine Grogy and Arielle Le-pellec (UV-induced photo-actuation analysis, Isabelle Jeacomine (NMR), Pierre Sailler (Tensile and DSC), Yu Ogawa (Solid state NMR), Jean-Luc Putaux, Yoshiharu Nishiyama, Isabelle Morfin (XRD), Christopher J

Barrett, Christophe Travelet, and Robert Pecora (Proof-reading) for their technical and scientific support during this work.

I can never forget the teachings of my old masters and teachers, Drs Ramin Khajavi, Amin meftahi, Omid Saligheh, Reza Akbari-Bengar, Somayeh Alibakhshi, and Master Mehdi Shaeri; thank you from the depth of my heart!

Having enthusiastic friends and colleagues who encourage you and push you to your limits is a blessing. For this blessing, I thank Drs Sami Halila, Franck Dahlem, and Raphael Michel, Agnieszka Janowska of Labex Arcane, Eric Bayma and Laurine Buon of PCANS, Patricia, Robin, Hong, Steve, Kritika, Armelle, Lawrencia, Dorcas, François, Mous, Maxime, Aicha, Kamilla, Bing, Julie, Sylvie, Maiia, Morane, Clarisse, Claire, Mumtaz, Elizangela, Daria Poshina, Jade, and Lama. And how can I forget about my good ol' mates, Diako (Zhazzab), Mahdi, Mohsen (Mohito), Mehdi (Ghanāti), Sadjad, Amin, Peyman, Mahsa, Adé et Ben, Mohammad et Negar, Rory, and Sophie.

At last, I am overjoyed for the opportunity of training at Grenoble Muay Thai club through blood, sweat, and tears with Grand-Master Bio Rassavong, David, Jean-Claude, Enos, Sébastien, Samuel, Thomas, Etienne, Sisou, Jérémy, Marie-Alix, Alex, Christine, Philippe, Cyril, Eddy, Romain, Mous, Karim, Guillaume, and Sylvain.

Long story short; thank you for being here with me!!

List of abbreviations

[AMIM]Cl	1-Allyl-3-methylimidazolium chloride
[BMIM]Cl	1-butyl-3-methylimidazolium chloride
AB	Azobenzene
AGU	Anhydroglucose unit
ATR-FTIR	Attenuated Total Reflectance-Fourier Transform InfraRed
Azo dye	4-(Phenylazo)benzoyl chloride
Azo-Cel	(2,3,6-*O*-tri-*p*-phenylazobenzoyl)cellulose
bp	Boiling point
CA	Cellulose acetate
CD	Cyclodextrin
DCM	Dichloromethane
DMAc	*N*,*N*-Dimethylacetamide
DMF	*N*,*N*-Dimethylformamide
DSC	Differential Scanning Calorimetry
ES	Electrospinning
EtOH	Ethanol
MeOH	Methanol
NMR	Nuclear Magnetic Resonance
r.t.	Room temperature

SEM	Scanning Electron Microscopy
TA	Thermally annealed
TGA	Thermogravimetry Analysis
THF	Tetrahydrofuran
UGA	Université Grenoble Alpes
UV-Vis	Ultraviolet-visible
vp	Vapor pressure
w.p.	Wood pulp
WCA	Water Contact Angle
XRD	X-Ray Diffraction

Table of contents

Chapter I : General Introduction

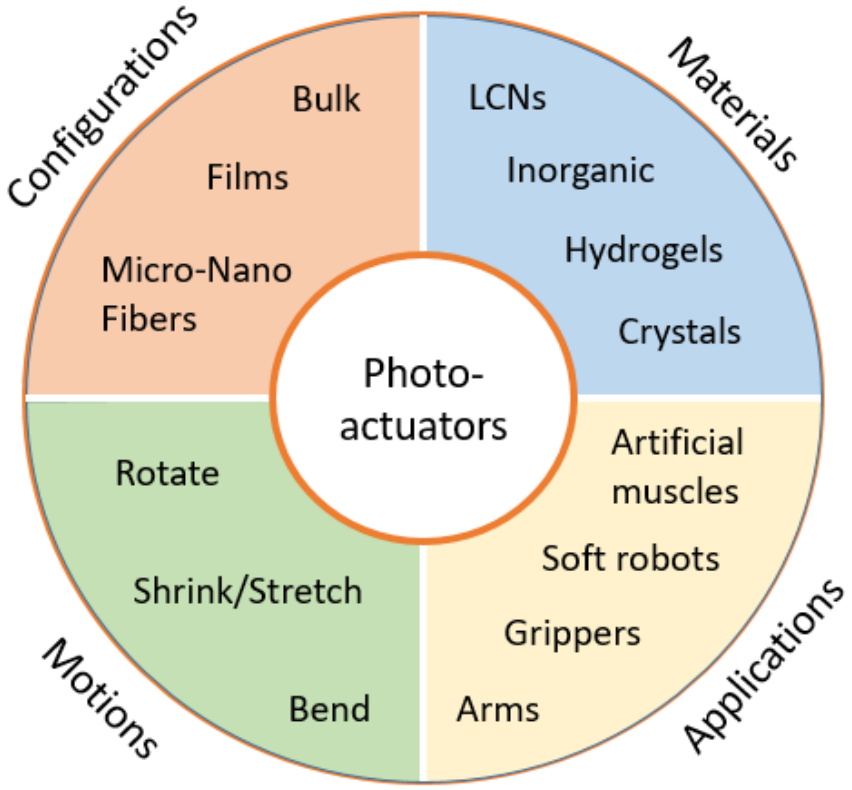

A presentation of photo-actuators [1].

I.1. State of the Art

Scientists have always aspired to produce high-tech structures to be used in optoelectronics, sensor technology, catalysis, filtration, and medicine. This has focused more recent attention to electrospinning[2–5], a well-established method of nanofibrous textile fabrication. The high specific surface area of electrospun nanofibrous textiles arising from the nanoscale interstitial spaces between the nanofibers makes them a promising scaffold to filter micro-scale biological and chemical contaminants. In addition to this effect of nano-size structure, a very important characteristic of the electrospun fabrics is that their morphology (*e.g.* the diameter and orientation of the fibers) can be controlled simply by adjusting technical electrospinning parameters such as solvent, concentration, solution feed rate, electric field, etc. and by using special electrodes (*e.g.*, a program-moving rotative electrode). Thanks to this feature, electrospun fabrics possessing superior mechanical resistance, *i.e.*, high tensile strength and Young's modulus, have been obtained by optimizing the diameter of the fibers and aligning them in desirable directions.[6–8]

Currently, raw materials of electrospun fabrics include bio-based polymers and are not limited to fossil fuel-based polymers,[9,10] and electrospun fabrics made of polysaccharides and their derivatives are one of the most rapidly growing product markets for various biomedical applications such as drug delivery, tissue engineering, wound dressing, biosensors, etc.[11–13] In addition, polysaccharides, notably cellulose, can offer robust scaffolds of smart materials thanks to their inherently superior mechanical properties.[14–18]

In this context, we are developing new types of smart cellulosic fabrics via electrospinning, aimed at diverse applications including membrane filters for efficient resolution of biologically essential chiral molecules,[19] as well as photo-responsive materials,[20] that are the main targets of this study. Among various stimuli-responses of photo-responsive materials,[21–23] special attention

has been paid to their light-driven deformation. This photo-actuation behavior can be precisely and remotely controlled without any physical connections such as electrical cables that are necessary for other types of actuation, for instance, with piezoelectrics. Azobenzene (AB) - contained polymeric materials [24–26] have been widely studied for their photo-actuation behavior that originates from the *cis*/*trans* geometric photo-isomerizations of the AB moiety at the molecular level, that can be amplified cooperatively to induce macroscopic deformations of the materials. Notably, liquid crystal polymers (LCPs) containing AB derivatives as their mesogenic pendant groups have demonstrated fast stimuli-response speeds and large deformation extents, which are enhanced by the cooperative nature of liquid crystal ordering.[27–32] In principle, the *trans* isomer of AB having a rod-like shape stabilizes the structure of liquid crystal phase, while the *cis* isomer having a bent-shape tends to destabilize the phase.

I.2. Photo-responsive materials

The desire to create materials and devices that replicate the skills and flexibility of living organisms has its roots in appreciation of nature's beauty. Animals have evolved to be extremely efficient and useful, making use of external conditions to initiate lifeforms activities. For example, it is worthy to note how ants can move while transporting goods and how soft aquatic creatures can move in a wide range of ways. Soft robotics aids mankind to achieve this dream. As opposed to hard robots, which have rigid components that restrict the flexibility and variety of devices, soft robots, which are entirely made of responsive polymers, more closely resemble living, soft-bodied animals and are more suited for interacting with people[33]. Stimuli-responsive polymers that undergo macroscopic deformations in response to external stimuli are of high-relevance for relieving soft robots of dependence on external and remote on-board control systems[34]. Magnetic

fields and light have mainly shown to be the most widely used stimuli for regulating such mechanical motions by providing distant, precise, and undamaging actuation techniques, with light having the benefit of not requiring large external magnetic configurations[35].

Researchers have dedicated significant amount of time and energy into developing novel materials with custom-designed molecular configurations. Liquid crystalline polymers (LCPs) are potentially the best candidate to develop light-controllable soft robotics because they demonstrate photo-deformation and allow creation of light–driven soft actuators by combining the entropic elasticity of polymeric elastomers with the potential to undergo reversible structure change behavior of liquid crystals (LCs)[36,37]. They are also ideal because of their ability of light-induced actuation in both wet and dry environments, as well as their ability to create molecular alignments inside the LC-matrix[38]. A foundation was established through numerous studies for the use of comb-shaped LCPs as new photoactive materials for optics, optoelectronics, photonics, holography, display technology, and telecommunication systems through the further development of such studies, which led to the commercial production of high-strength fibers and self-reinforced plastics based on LCPs with main-chain mesogenic groups[39–43]. Mesogens are substances with liquid crystal characteristics that when gathered together, they construct a liquid-crystalline network[44]. The physical properties of LC materials are similar to those of ordered crystalline solids and isotropic liquids. These materials retain a fluid-like capacity to flow while retaining a degree of molecular order when in the LC state, as illustrated in Figure I.1.

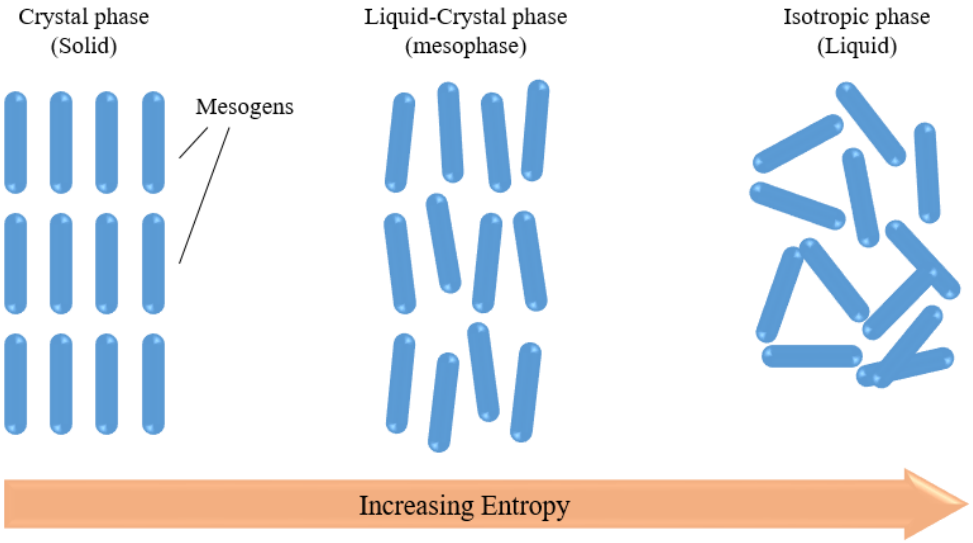

Figure I.1. Three states of a typical LCP.

LCPs can also include photochromic compounds. A photochromic compound is a chemical that when exposed to different wavelengths of light, undergoes a reversible change between two states of A and B. This effect is called photochromism[45]. Figure I.2 illustrates this effect.

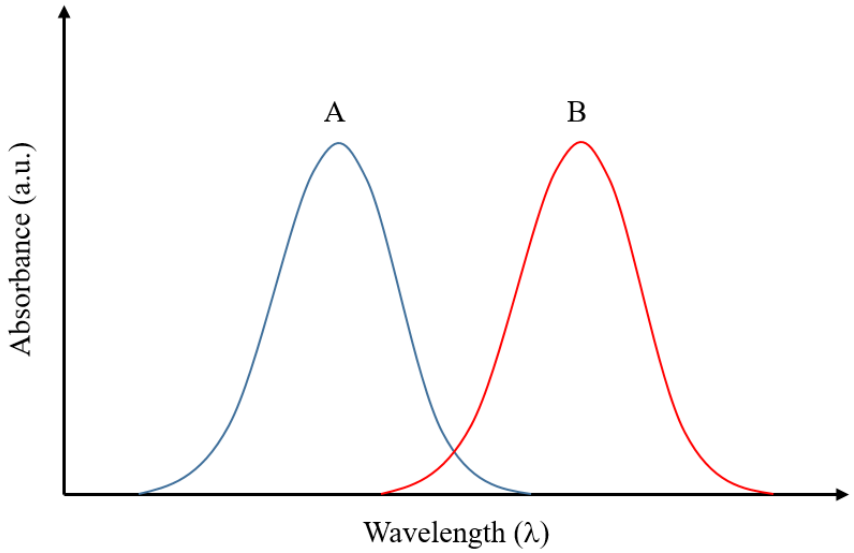

Figure I.2. Absorption spectra of the two states of A and B for a photo-switch[45].

Depending on the respective thermal stabilities of the two isomers, there are two different types of evaluating photo-switches. The first group defined as T-type photochromic compounds, are photos-witches with low thermal threshold that are able to be thermally isomerized from the metastable to the stable state; meaning that the thermally unstable isomer frequently transforms back into the thermodynamically stable state over a period of time that could be ranging from a milliseconds to several minutes. The second group is defined as P-type photo-switches whose both isomers are kinetically stable and their thermal threshold is relatively high. Therefore, only light irradiation can interconvert them[46,47].

I.3. Photochromic compounds

Apart from AB, there are other photochromic molecules that demonstrate photoresponsivity. Diarylethene, spiropyran[48], iminothioindoxyls, indigos, hemithioindigos, hydrazones, stilbene[49], and fulgides[47] are some of the most widely known photochromic molecules. Scheme I.4 illustrates the photo-isomerization mechanisms of these mesogenic molecules.

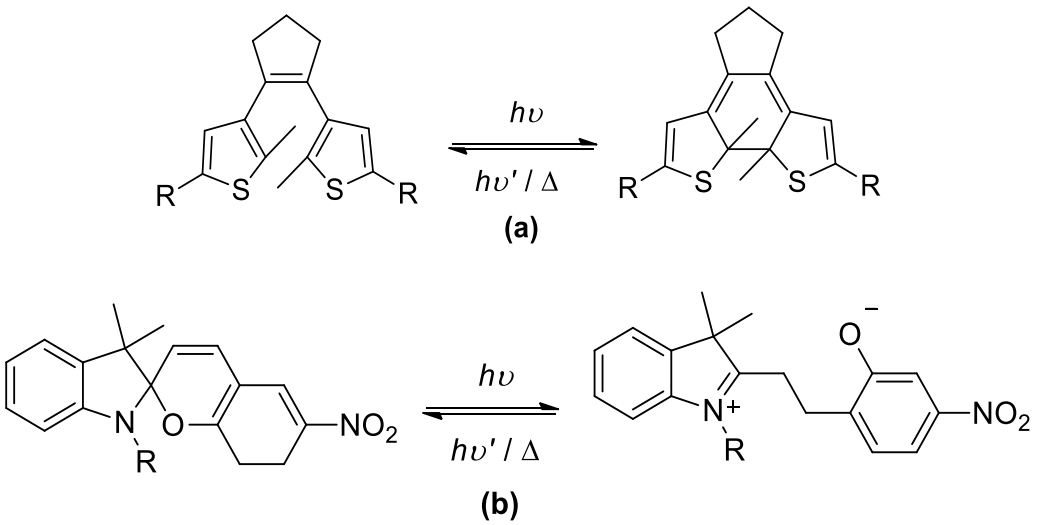

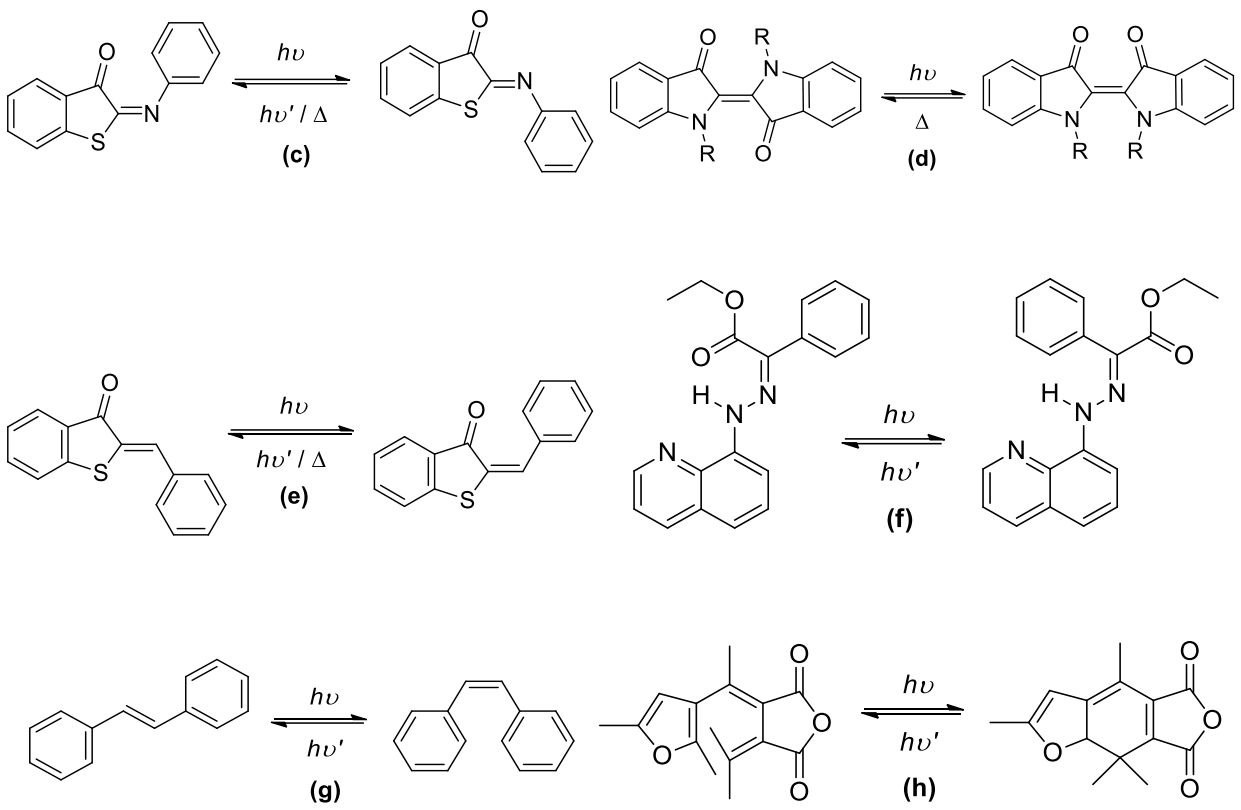

Scheme I.4. Some of the most renowned photochromic molecules that demonstrate photo-responsive behavior: (a) diarylethene, (b) spiropyran[48], (c) iminothioindoxyl, (d) indigos, (e) hemithioindigo, (f) hydrazones, (g) stilbene[49], and (h) fulgides[47].

Currently, some of these photo-switches are being studied for medicinal applications, and the researchers aspire to maximize the behavioral difference between the two isomers of the desired compound, *i.e.* the irradiated and non-irradiated states[47]. As AB is the most studied photochromic compound, in this study the main focus will be on its behaviors and the potentials that this compound offers, *e.g.* the development of artificial muscles[50], once it is functionalized with cellulose.

I.4. Azobenzene

One of the most renowned mesogenic structures that counts as a photochromic compound is AB. AB is an aromatic compound where two phenyl rings are connected together by an azo bond (-N=N-). By functionalizing the aromatic rings with different compounds, it is possible to vary the geometry and the properties of electron withdrawing/donating of a vast class of compounds. This class of compound is often referred to as "ABs" or simply "azos"[51]. Scheme I.1 presents some examples of ABs.

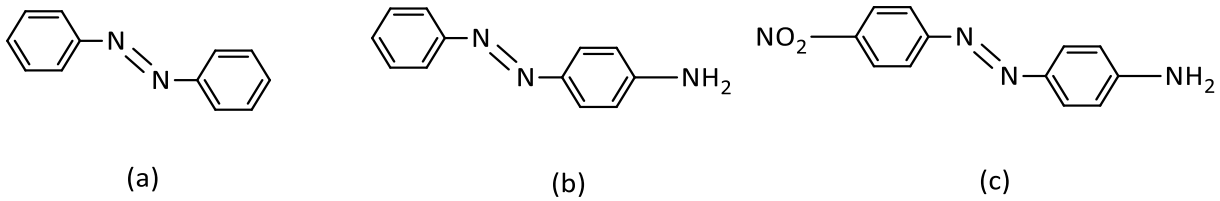

Scheme I.1. Different classes of AB compounds: a) the AB class, b) the aminoazobenzene class, c) the pseudo-stilbene class[51].

ABs hold various spectroscopic features, yet it is helpful to examine them in broad terms based on their photochemistry. The π-conjugated system particularly produces significant electronic absorption in the UV and/or visible sections of the light spectrum. This spectrum may be adjusted using the ring-functionalization pattern, *i.e.* functionalizing AB derivatives onto polymer backbones and creating photo-responsive materials. ABs can display LC phases in both polymeric and small-molecule forms [52,53]. ABs share a common behavior, that is the efficient and reversible photo-isomerization, which happens when a photon in absorbed within the absorption band. Scheme I.2 presents this photo-isomerization mechanism.

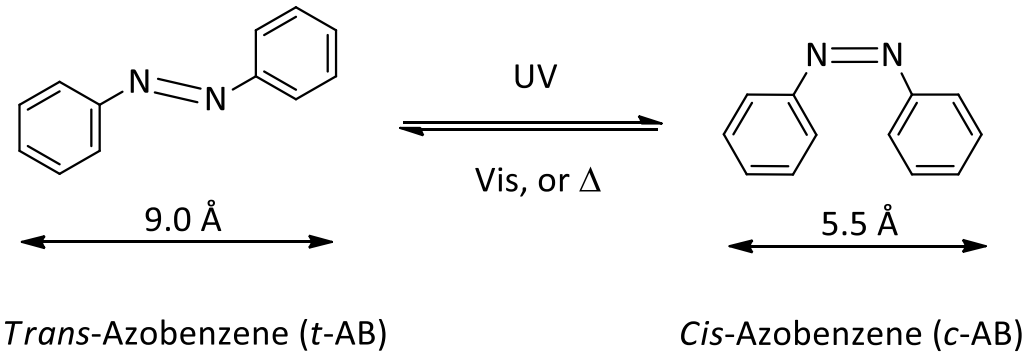

Scheme I.2. Photo-isomerization mechanism of AB [51].

AB is usually consisted of *trans* isomers at a stable state and under the visible light (*t*-AB). The molecule undergoes *trans*-to-*cis* photo-isomerization upon photon absorption and emerges as *c*-AB. The *c*-AB restores back to *trans* state by either thermal interference or irradiation of visible light [51]. There are 4 proposed possible theories for the photo-isomerization mechanism of AB, *i.e.* inversion, rotation, inversion-assisted rotation, and concerted inversion. The inversion process causes one N=N-C angle to grow to 180°, whereas the C-N=N-C dihedral angle remains constant at 0°, resulting in a transition state containing one sp hybridized azo-nitrogen atom. For the rotational theory to take place, the π bond of N=N linkage must break to permit the existence of N-N bond, which allows an increase of C-N-N-C dihedral angle while the N-N-C angle remains constant at 120°. Large changes in the C-N=N-C dihedral angle and lesser but still considerable changes in the N=N-C angles occur concurrently in inversion-assisted rotation. At last, for photo-isomerization by way of concerted inversion, both N=N-C bond angles must rise to 180 degrees in order for isomerization to take place that creates a linear transition state. It is imperative to note that while the other three theories include polar transition states, the transition state created by concerted inversion has no net dipole moment [54–57]. Scheme I.3 summarizes all 4 pathways.

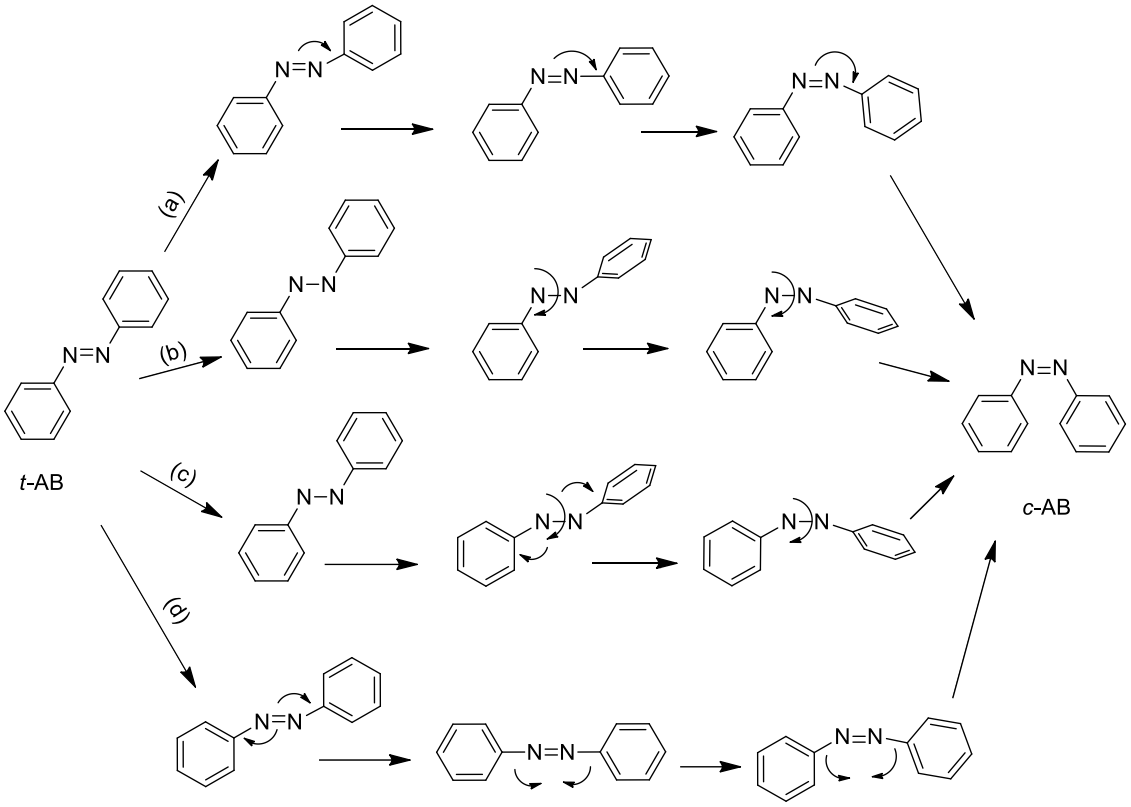

Scheme I.3. Possible theories of photo-isomerization mechanism of AB. a) Inversion, b) rotation, c) inversion-assisted rotation, and d) concerted inversion [58].

AB was first discovered and discussed in 1834 ,[59] and later in 1937, G. S. Hartley presented a research about the effects of light irradiation on the conformation of N=N linkage[60,61]. He noted an inconsistency in absorbance measurements of AB when it was irradiated by light, and reported the result of this finding as an evidence of the existence of *c*-AB. Hartley was able to extract and isolate *c*-AB by employing solvent extraction methods, notably acetone. From that point forward, a significant number of research has elevated AB one of the most renowned photo-switches [62–66]. As described above, AB demonstrates photochromism and in consequence, a shift of absorbance in regard to wavelength takes place.

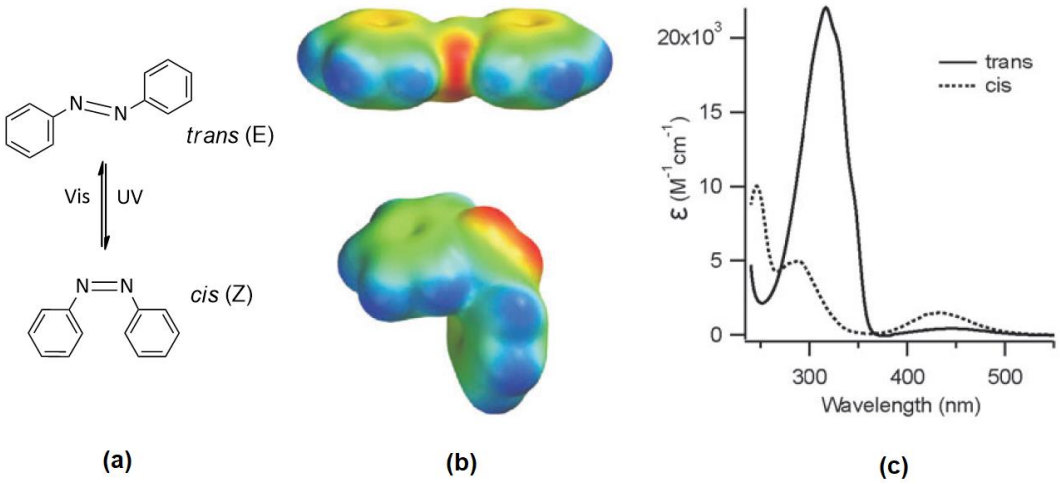

Figure I.3. (a) The *trans* and *cis* isomers of AB. (b) Computer-modelled *t*-AB and *c*-AB. Space-filling models are colored by electrostatic potential (red is negative and blue is positive). (c) Electronic absorption spectra of the *trans* and *cis* isomers of AB dissolved in EtOH[66]. Copyright 2011, Chemical Society Reviews.

As illustrated in Figure I.3, the *t*-AB isomer exhibits a significant absorption band corresponding to π-π* electron transition of Azo bond around 320 nm, while demonstrating a weak absorption band corresponding to n-π* transition band of Azo bond around 440 nm. Once irradiated by UV light and undergoing *trans*-to-*cis* photo-isomerization, the *c*-AB isomer then shows a stronger n-π* electron transition around 440 nm, but a weaker π-π* transition band at 280 nm, and a new peak at 250 nm. In the absence of light, the *t*-AB isomer predominates over the *c*-AB by 99.99 % [65] because its enthalpy of isomerization is at 49.1 ± 1.0 kJ/mol [67] (This is the enthalpy of isomerization, aka the difference between *t*-AB and *c*-AB that shows the **t**-AB predominates over the *c*-AB).

There are several important points that must be taken into account when discussing the photoresponsivity of AB-functionalized materials. Firstly, it is essential that the AB-functionalized material must be connected to AB molecules, in a way that this connection alters its functionality. This effect can rely on a number of variables, including the location and the kind of material that

the AB molecule is linked to (for example, to a protein), as well as the AB derivative employed. Secondly, irradiation results in a photo-stationary state with a maximum of about 80% *cis* or about 95% *trans* because the absorption spectra of the trans and cis isomers heavily overlap. However, almost 100% of the *trans* isomer is produced by thermal *cis*-to-*trans* relaxation. Therefore, if one wants to induce more significant fold-changes in the *cis* isomer, it could be desirable to utilize thermal relaxation to reset the switch. At last, the light wavelength at which the photo-isomerization occurs must be compatible with cells and tissues, if the photo-responsive behavior is sought to be developed *in vivo*. Longer wavelengths of light are less absorbed by other biomolecules in the cell, allowing them to more readily pass through cells and tissues (for example, Nicotinamide Adenine Dinucleotide + Hydrogen (NADH)). The absorption wavelength may need to be red-shifted since unaltered AB photo-isomerizes in the near UV area[66].

ABs are robust compounds that can be incorporated into a diverse range of different materials. They are notable known for their ability to be implanted inside a matrix for increased stability and control, or form covalent bonds with polymers. Numerous studies has been conducted with a focus on both amorphous and LC systems of AB materials, and they show beneficial applications for self-assembled superlattices and monolayers, sol-gel silica glasses, and biomaterials. Because the AB is adequately non-reactive, it can be incorporated into a variety of synthesis techniques with different other compounds, including CDs, proteins, crown ethers, and 3D polycyclics[51,68–78]. As mentioned above, AB chromophores can either be incorporated into LCPs (by crosslinking), or be functionalized onto the main chain. This will allow the LCP to demonstrate photoresponsivity and become a photoactuator. Figure I.4 presents an example of an LCP film undergoing *trans*-to-*cis* photo-isomerization upon UV light irradiation.

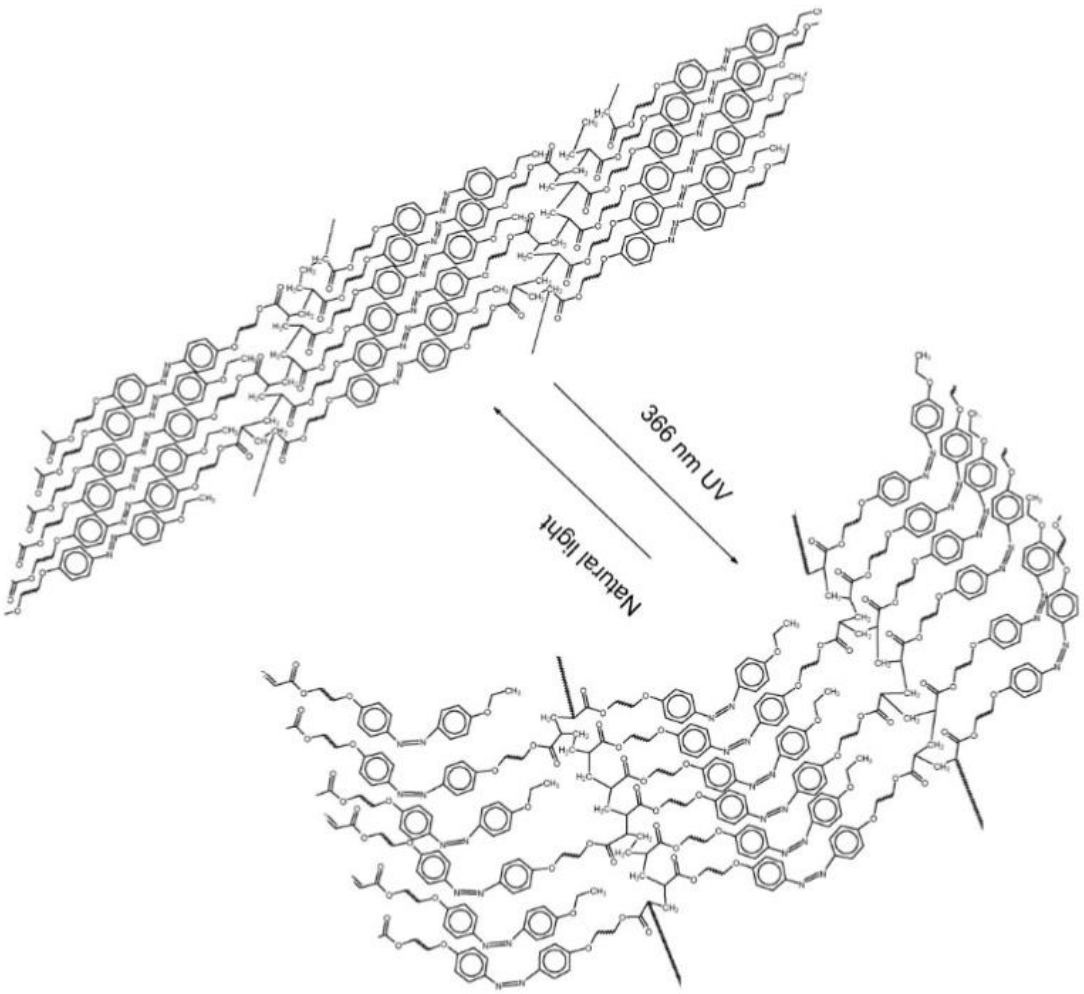

Figure I.4. A schematic representation of the shape deformation of an LCP film produced by AB chromophores undergoing *trans*-to-*cis* photo-isomerization, hence destroying the LCN [79]. Copyright 2009, Macromolecular rapid communications.

I.5. Applications of AB

ABs can be utilized in a wide range of applications, naming biological imaging[80], cell attachment/cell adsorption[81], photo-pharmacology[82], controlled release/drug delivery[83], and bio-macromolecule regulation [84].

In 2018, Zhao and colleagues [80] proposed a successful control technique for NIR modulation on the host-guest interaction between AB-modified lanthanide upconversion

nanoparticles (UCNP@Azo) and β-cyclodextrin (β-CD)-modified down-conversion nanoprobes (DCNM@ β-CD) that allows assembly and disassembly of nanoparticles in the body of mice. When exposed to 980 nm NIR light, UCNPs can transform NIR into UV and blue light, resulting AB molecules to isomerize. Due to a tissue penetration depth of a few centimeters, DCNP may reach an effective emission of 1060 nm in the second NIR region (NIR-II, 1000-1700 nm) under 808 nm NIR irradiation.

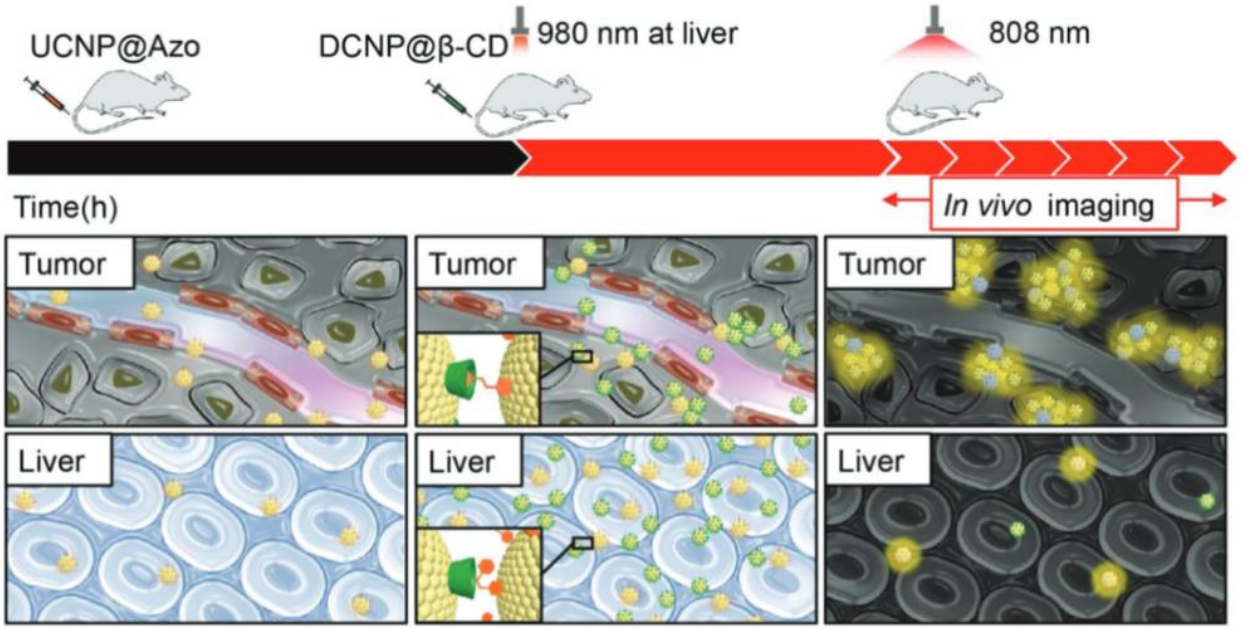

Figure I.5. Nanoparticle assembly caused by supramolecular recognition and disassembly modulated by 980 nm NIR. Copyright 2018 Advanced Materials [80].

As a result, auto-fluorescence imaging with a resolution of 10 m beneath tissue is projected to be used for *in vivo* fluorescence imaging. To achieve *in vivo* nanoparticle formation and NIR light-regulated breakdown, the Azo/β-CD host-guest supramolecular engineering technique was employed and this strategy allowed for an increase of approximately four times greater of the buildup contrast agent at the tumor, comparing to the single-injection approach.

Zhang et al., in 2017 [85] developed photo-switchable self-assembled monolayers (SAMs) on gold electrodes using sugar (galactose/mannose)-decorated AB derivative ligands, presented in Figure I.6. AB was utilized to link the monosaccharides together, one of which was galactose, that could be preferentially coupled with peanut agglutinin (PNA) to engage with the asialoglycoprotein receptor (ASGPr) of Hep-G2 cells. The other employed monosaccharide, mannose, was used to exclusively connect conconavalin A (Con A) and eventually engage with the mannose receptor (MR) on the macrophage cells. It is worthy of noting that gold electrodes were modified using the resultant galactosyl-mannosyl-tethered AB ligands.

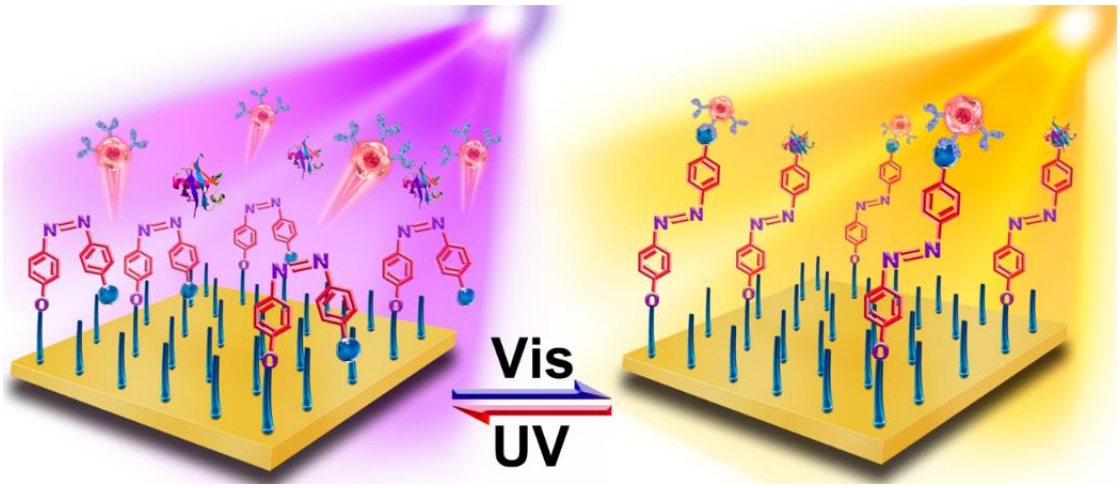

Figure I.6. Schematic representation of photo-switchable self-assembled monolayers (SAMs) on gold electrodes using sugar (galactose/mannose)-decorated AB derivative ligands. Copyright 2017 American Chemical Society [85].

Regarding the photo-pharmacological application of AB-containing materials, Broichhagen and colleagues in 2015 [86] reported their results of a study on a novel incretin mimetic with photo-switching properties, made of glucagon-like peptide-1 receptor (GLP-1R) agonist liraglutide. They employ LirAzo, a peptidic substance that has an AB molecule inside of it. The *trans*-LirAzo is primarily engaged in calcium influx, whereas the *cis*-LirAzo promotes the synthesis of cAMP. LirAzo may also enable photo-control of insulin secretion, which is why it

was incubated with mouse islets before they were either exposed to darkness or light (λ = 350 nm). The *cis*-LirAzo isomer increased the amount of insulin secreted in response to glucose in a way similar to Lira (approximately 2.5-fold), while *trans*-LirAzo was far less efficient (almost 1.4-fold). As a result, LirAzo achieves optical control of insulin secretion and survival of the cells. Figure I.7 presents an overall scheme of this procedure.

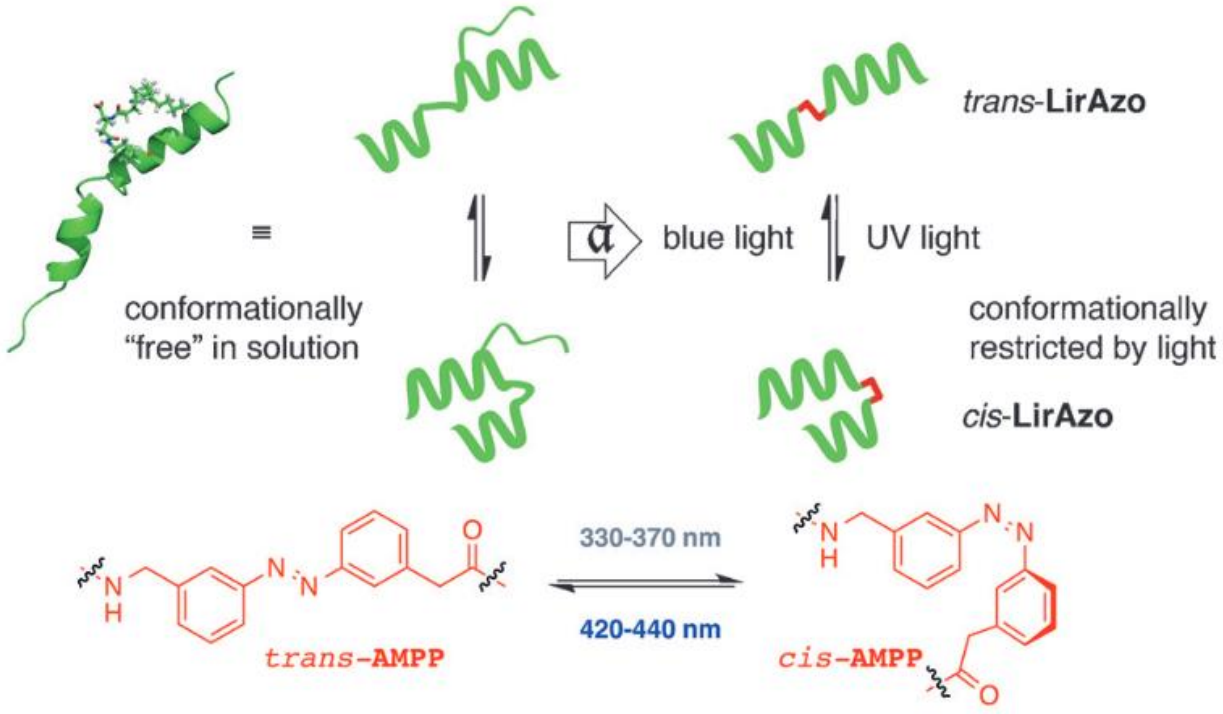

Figure I.7. Design and primary structure of LirAzo. a) The liraglutide NMR structure served as template for the synthesis of LirAzo, which differs in the placement of AMPP (red) between the helices. b) cis-AMPP and trans-AMPP manifest upon UV and blue light irradiations respectiveley. Copyright 2015 Angewandte Chemie International, published by Wiley-VSH [86].

The control of drug release is of utmost importance to insure a patient receives a more appropriate medical service. The main objective of a drug controlled release system's therapeutic use is to sustain a medication's effective concentration within the body even after inconsistent drug administration. This is accomplished *via* continuous release of a controlled release system, where

the drug can be locally administered to the ill organ or cells, thanks to a well-established drug delivery system. ABs have proven to be good candidates for drug delivery purposes, since the changes in their structures caused by UV/vis light irradiations, lead to eventual structural changes of the controlled drug delivery system [86]. Chi and colleagues in 2015 [83] reported their results on the water-soluble thermally-responsive pillar[7]arene (WP7) which acts as host and interacts with the AB derivatives as guest.

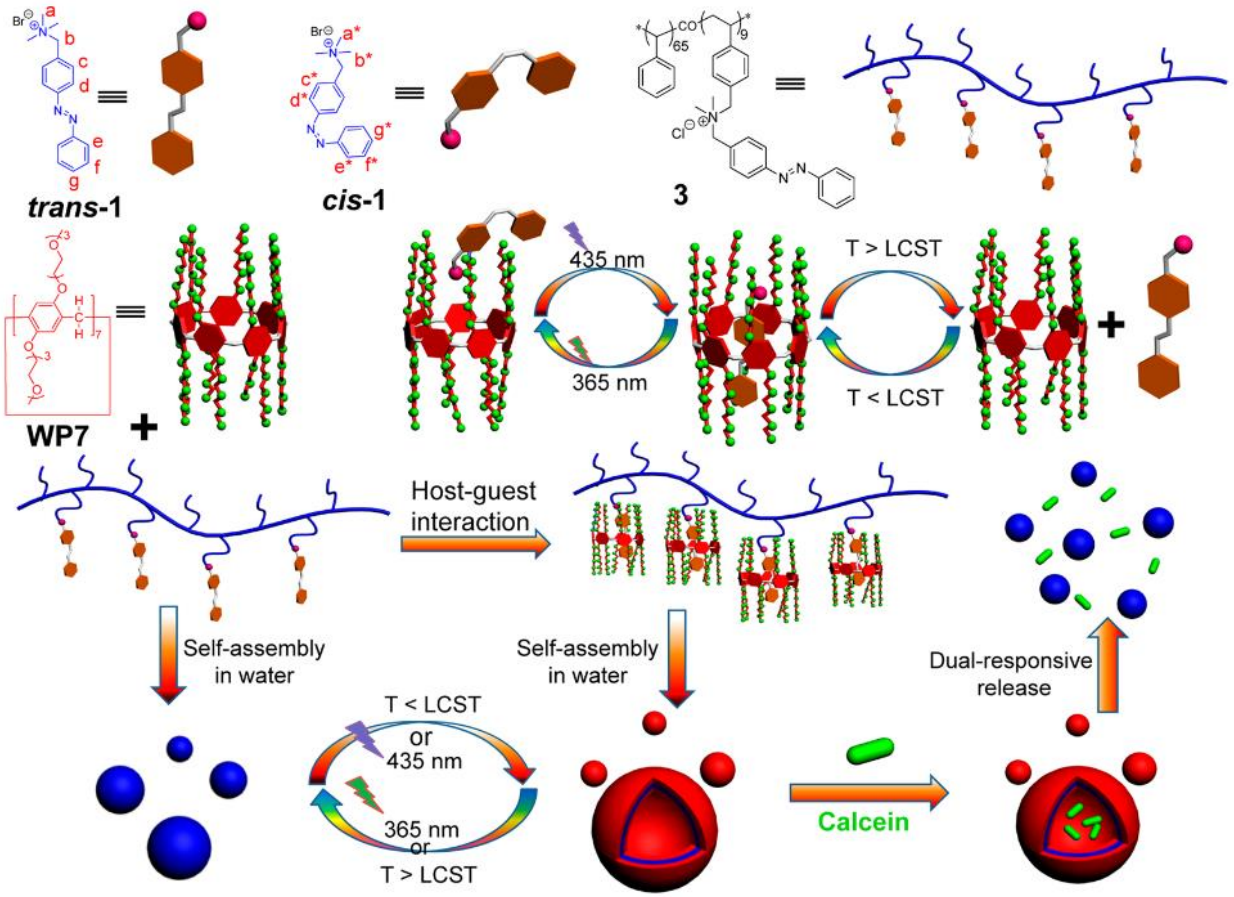

Figure I.8. Controlled release mechanism of dual-responsive assembly and disassembly of host-guest interaction of WP7 with AB [83]. Copyright 2015 Journal of the American Chemical Society.

The AB derivative can enter the cavity of WP7 when the temperature is below the Lower Critical Solution Temperature (LCST) of 60 °C, thus permitting the formation of hydrogen bonds.

This well-structured molecule can self-assemble when it comes in contact with water, resulting in a formation of a vesicle. The hydrogen bond is broken when the temperature exceeds LCST, which causes the vesicle molecules to disintegrate. The AB derivative undergoes a *trans*-to-*cis* photo-isomerization when exposed to UV light (λ = 365 nm), which leads to the disassembly of the vesicle molecules and a release of chemicals that were within. This thermal treatment causes an explosive release of calcein molecules. It is reported that a total amount of 90 % of calcein molecules are released after 10 h of thermal treatment. However, this release of calcein molecules is rather slower (at 70 % release rate) when the system is exposed to UV light for 10 h. Figure I.8 illustrates an overall scheme of this process.

The development of methods to create stimuli-responsive nano-devices based on bio-macromolecules, such oligonucleotides, peptides, and macromolecules containing carbohydrates, has attracted a lot of interest in light of recent developments in the field of bio-macromolecule regulation. AB particularly exhibits exceptional application potential in light-driven structural modulation of bio-macromolecules as a photo-responsive compound, which is why the bio-macromolecules that are functionalized with AB can show changes in physical and chemical properties, caused by the demonstrate stimuli-responsive behavior of functionalized AB[87]. For example, AB is regarded as one of the most prevalent molecular switches designed to regulate the DNA and oligonucleotides. The construction or disassembly of the hairpin structure created by the self-complementary sequence can be controlled by switching between the cis/trans isomers of AB inserted into the phosphate backbone[84]. Wang and colleagues in 2019 [88] proposed a model of allosteric (*i.e.* relating to a change in the shape and/or activity of a protein[89]) light-responsive nano-switch and employed AB to alter the conformation of two DNA hairpins. In their study they revealed that It is possible for a DNA hairpin (designated as H#1) to link with a thrombin DNA

aptamer when it exhibits a stem-loop shape and comprises a single-stranded DNA aptamer sequence. The unpaired portion of H#1 becomes more stiff as a result of the repression sequence (RES) joining with one of the DNA hairpins (designated as H#2), making it impossible for H#1 to maintain the stem-loop shape necessary to bind the thrombin target. When a PTG molecule (a particular photosensitive AB derivative) is introduced into RES, the PTG undergoes *trans*-to-*cis* photo-isomerization in response to UV light irradiation, which separates RES from H#2, resulting in a binding of H#1 to thrombin. A decrease in the enzyme activity marks the end of the process. Figure I.9 represents an overall mechanism of this process.

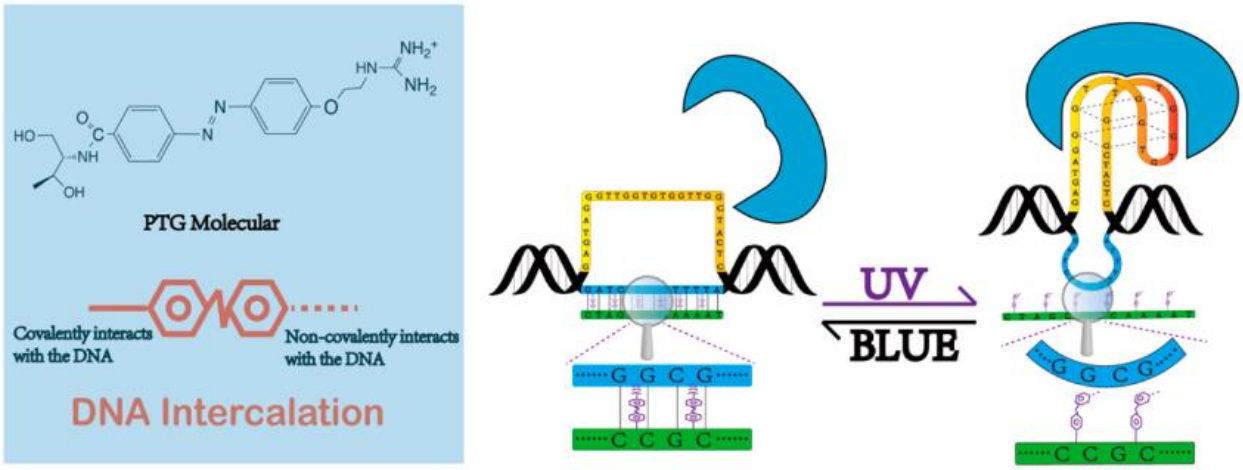

Figure I.9. A model of allosteric light-responsive nano-switch and employed AB to alter the conformation of two DNA hairpins [88]. Copyright 2019 American Chemical Society.

Apart from the abovementioned applications of AB-containing materials, AB can be employed to develop photo-mechanical azo materials, notably azo monolayers and coatings, amorphous azo polymers, and azo-LCPs[51]. Ikeda and colleagues developed a model of stimuli-responsive LC elastomers (LCEs) and LC gels (LCGs) in solution over a course of numerous studies[27,28,90]. They demonstrate that AB-containing materials not only can show one-dimensional movements, but two dimensional movements as well.

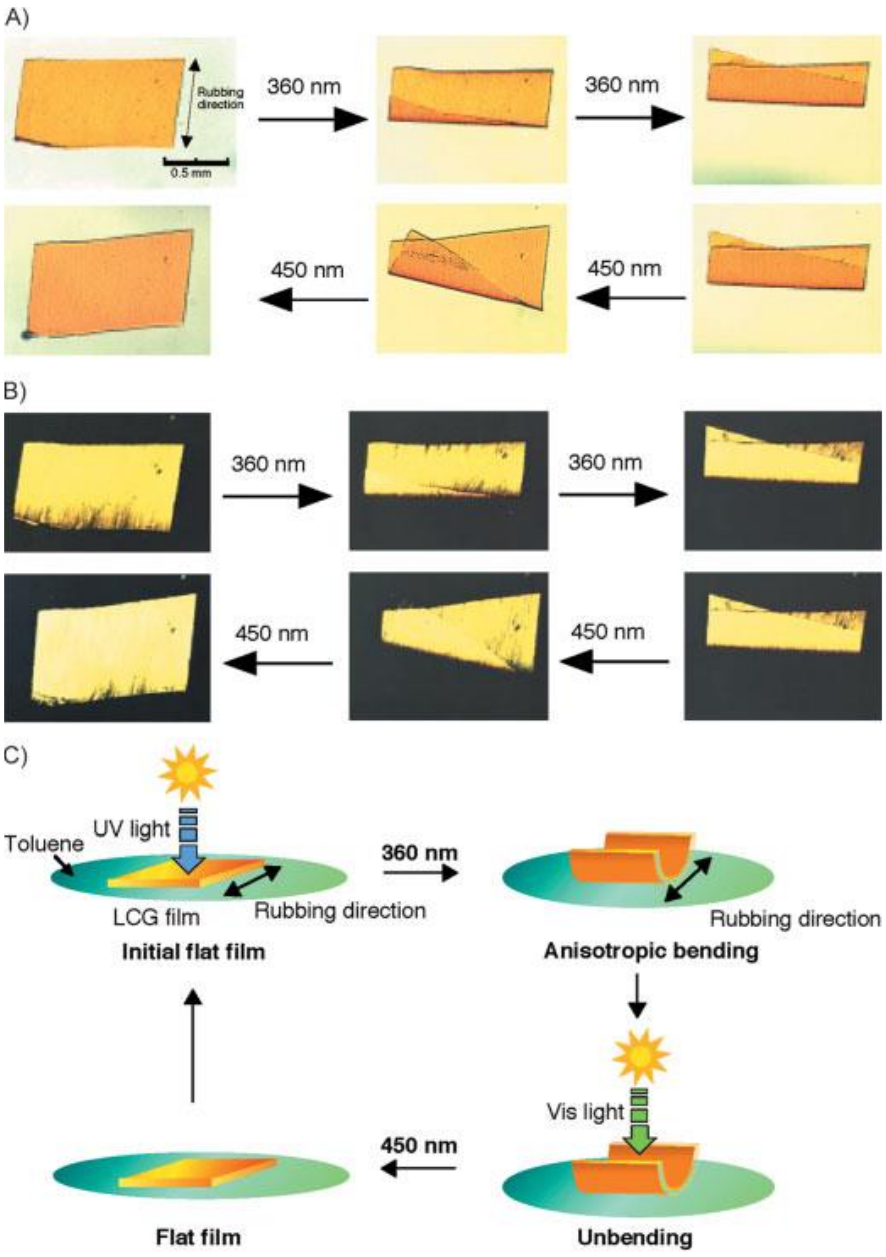

Figure I.10. Bending and unbending behavior of LCG films in toluene. a) Pictures taken during bending and unbending processes. b) Polarized pictures observed during bending and unbending processes. c) Overall schematic illustration of anisotropic bending and unbending behavior of the LCG film [27]. Copyright 2003 Wiley Online Library.

As illustrated in Figure I.10, The LCE film was seen to bend in the direction of the incoming UV light's irradiation along the rubbing direction, and upon exposure to visible light, the bent film returned to its original unbent condition. Essentially, altering the wavelength of the

irradiated light was sufficient to reverse this bending and unbending behavior. The bending once again occurred when the film was rotated 90 °, showing that the bending can be anisotropically prompted, as long as it is along the alignment layers' rubbing direction. Due to the fact that the attenuation coefficient of the AB moiety at around λ = 360 nm is high, more than 99 % of the light photons are absorbed within 1 µm of the surface of the product, resulting in a *trans*-to-*cis* photo-isomerization of the AB moieties on the surface, while the *t*-AB moieties in the bulk of the film stay untouched. Consequently, only the surface layer experiences a change of volume, which leads to a far from ideal bending of the material in the direction of the incoming light's irradiation. This phenomenon is called the anisotropic bending behavior[27].

In 2003, Li and colleagues [91] reported their results on the use of initiator to photo-polymerize monodomain nematic AB side-on elastomers, where the Mesogens were parallel to the long axis of the film. When aligned nematic AB monomers were used for the photopolymerization process in standard LC cells, thin films of these LCEs displayed rapid photo-chemical contraction in less than a minute, up to 18% under UV light irradiation, and a stagnant thermal reverse reaction in the dark. Figure I.11 displays their result.

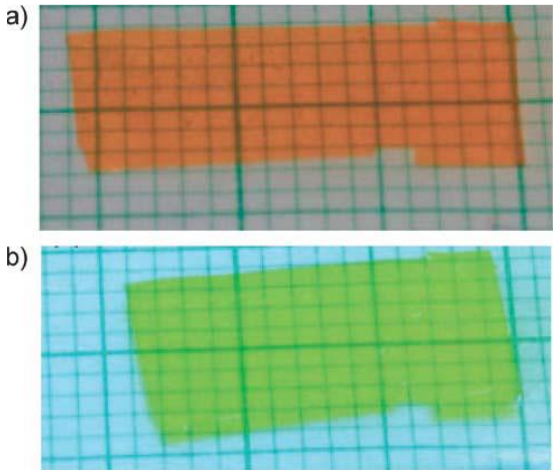

Figure I.11. Images of the photo-deformation of Li and colleagues' AB-CLCP: (a) before UV irradiation, and (b) under UV irradiation [91]. Copyright 2003 Wiley Online Library.

Camacho-Lopez and colleagues in 2004 [92] showed that an LCE sample's mechanical deformation responding to uneven irradiation by visible light increases significantly, when AB dyes are dissolved into it and a bending of over 60 ° was observed. Such a dye-doped LCE sample floating on water responds to an overhead laser beam by "swimming" away from it in a manner similar to a flatfish (Figure I.12).

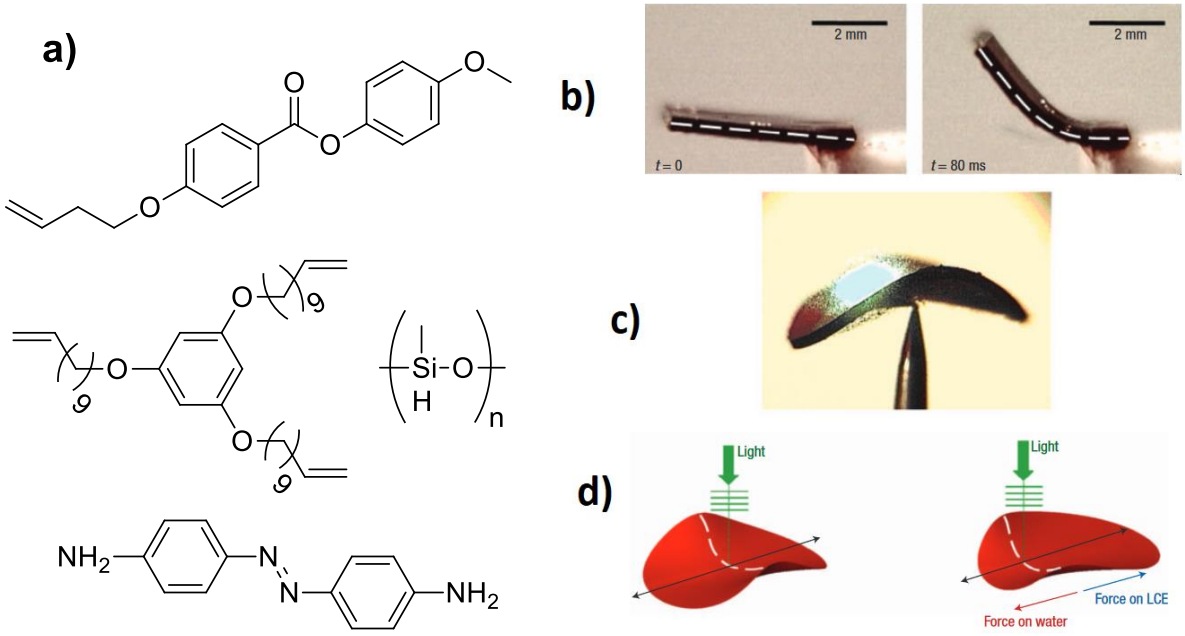

Figure I.11. a) Chemical structures of the nematic LCE and dye. b) Photo-mechanical response of the swimming CLCP sample. c) The shape deformation of a CLCP sample after exposure to λ = 514 nm light. d) Schematic presentation of the mechanism showing the locomotion of the dye-doped CLCP sample [92]. Copyright 2003 Wiley Online Library.

In a more recent study, Wang and colleagues in 2020 [93] succeeded in creating a photo-responsive LCP organogel that contains and AB group in its main polymer chain and could be created via π-π interactions of AB with hydrogen bonds of the pendant amide group. Under un extremely low intensity UV irradiation, the Azo-mLCP gelator exhibited rapid *trans*-to-*cis* transformation in solution. Additionally, when approximately half of *t*-AB converted to *c*-AB, the

effectively reversible gel-to-sol transition could be initiated. While the effective photo-mechanical effect was attributable to the imperfect trans-to-cis conversion method, the good mechanical characteristic of the organogel was strongly associated to the insertion of the main-chain LCP gelator.

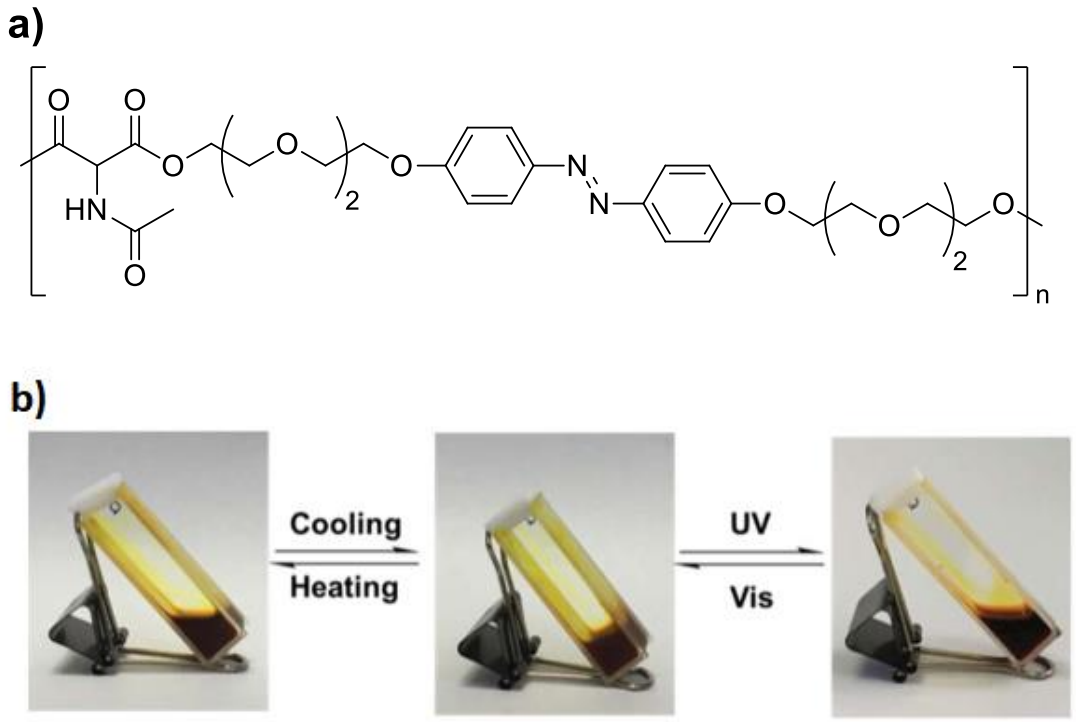

Figure I.12. a) Chemical structure of Azo-mLCP. b) Dual stimuli-responsive behaviors of the organogel with 8 wt% Azo-mLCP in dioxane [93].

Previously, the synthesis, the *cis*/*trans* geometric photo-isomerizations of the AB moiety in solution state, and the electrospinnability (under specific conditions) of Azo-Cel was reported [20]. The AB-functionalized cellulose (Azo-Cel) reported by Otsuka&Barrett, demonstrates reversible photo-responsivity upon UV and visible light irradiations and their rates of conversion (Figure I.13).

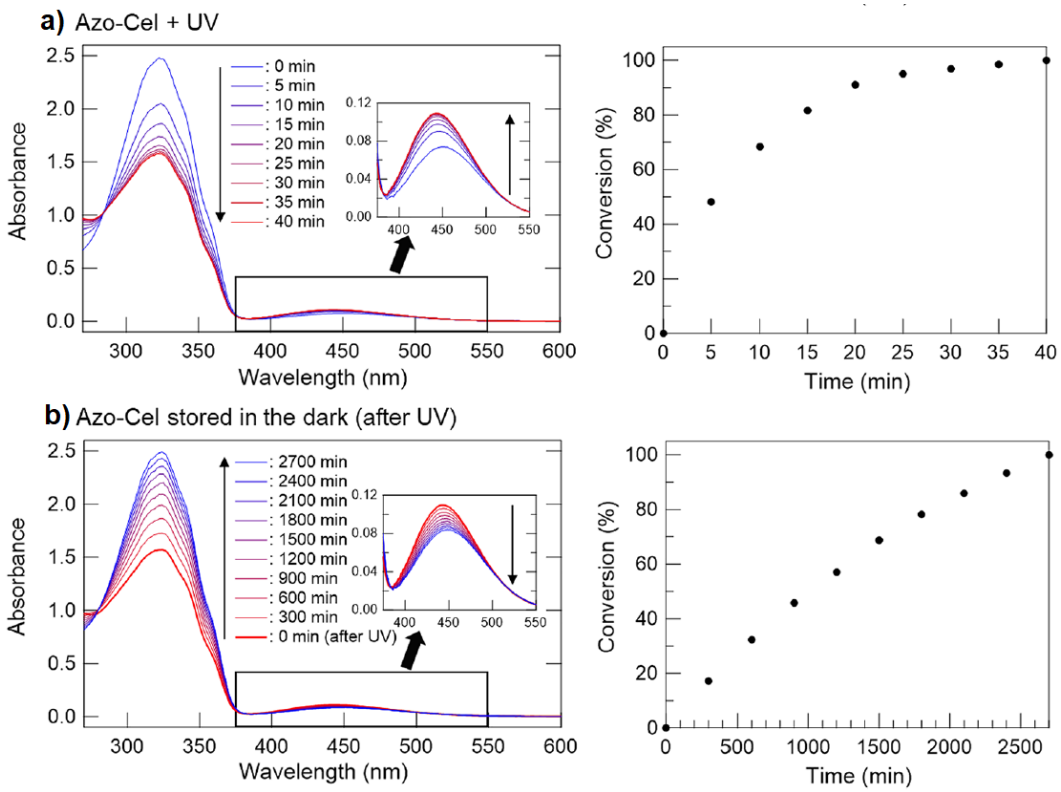

Figure I.13. Reversible photo-responsivity of Azo-Cel upon UV and visible light irradiations. a) Azo-Cel in THF upon UV light irradiation. b) Azo-Cel stored in the dark at r.t. after UV light irradiation [20]. Copyright 2019 Cellulose.

In this thesis, the electrospinning conditions of Azo-Cel are optimized to form a strong self-standing fabric that exhibits both light-driven wettability changes and asymmetric photo-mechanical bending deformations. Then, the regioselectively-functionalized Azo-Cel is synthesized and its electrospinnability as well as photo-responsivity is studied. Current knowledge of photo-actuators does not propose a clear way of producing more robust photo-actuator and how to mass-produce such products. The self-standing Azo-Cel textile is one of the very few types of photo-actuators that is made of micro/nanofibers, making it more robust than thin films (the conventional material in literature).

Chapter II : Synthesis and Material Characterization of Azo-Cel

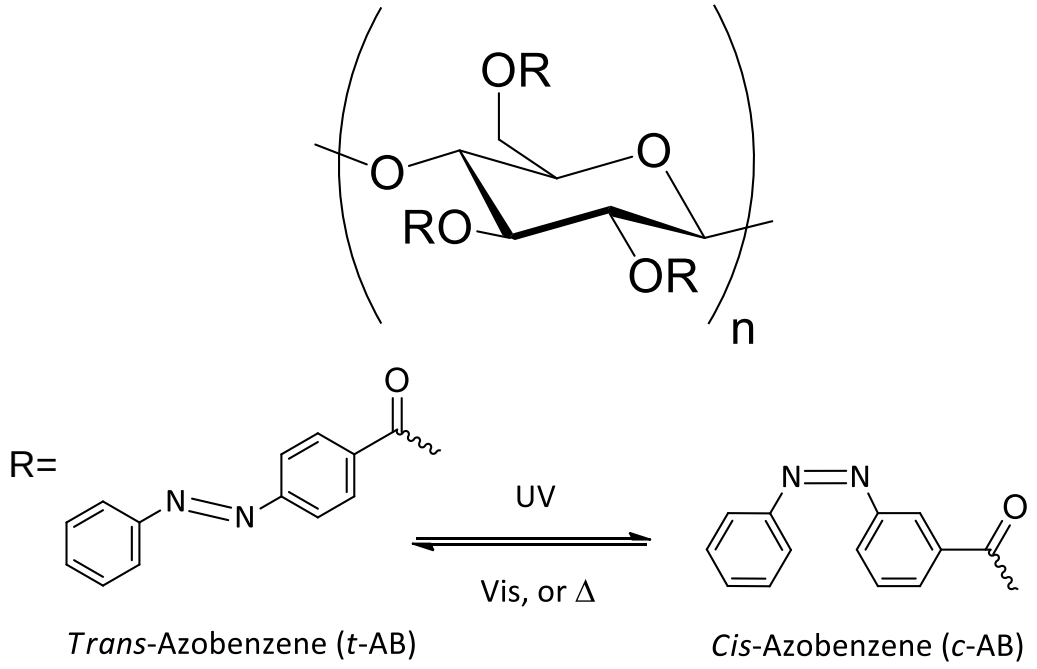

II.1. Introduction

The synthesis, manipulation, and modification of nanomaterials with clearly defined structures and applications have attracted considerable interest in nanoscience and nanotechnology, due to the numerous potential uses they have [90,91]. One of these applications is functionalization of polymers that contain photochromic moieties such as AB, spiropyran, and stilbene [96–98]. One of the most prevalent basic materials produced from biomass and renewable forestry resources is cellulose, which is a polysaccharide constituted of a linear chain of a few hundred to several thousands of β (1→4) connected D-anhydroglucose units [99,100]. The focus has been on their superior qualities as biocompatible, biodegradable, and bioactive[101] natural materials as well as their potential as petrochemical substitutes [102]. Cellulose-based polymers are ideally suited to develop stimuli-responsive materials and researchers have dedicated a lot of attention to them for their ability to demonstrate stimuli-responsive and more precisely, photo-responsive changes attributed to their physical properties by changing their surrounding environment [103].

In this chapter the synthesis and characterization of AB-functionalized cellulose: (2,3,6-*O*-tri-*p*-phenylazobenzoyl)cellulose (Azo-Cel) is thoroughly discussed, which is the main utilized product of this PhD project. This section firstly focuses on the background and introduction of utilized materials, as well as the analysis of the product. The methods of analysis and measurements for Azo-Cel polymer powder include: Attenuated Total Reflection Fourier Transform Infrared Spectroscopy (ATR-FTIR), Ultraviolet-visible (UV-vis) spectral analysis, solid state and liquid state Nuclear Magnetic Resonance spectroscopy (NMR), X-ray diffraction (XRD), Thermogravimetry analysis (TGA), and Differential Scanning Calorimetry (DSC).

II.2. Experimental

Materials

Microcrystalline cellulose (MCC: Avicel PH-105; derived from wood pulp; ~20 μm particle size) was purchased from FMC BioPolymer Co. and vacuum dried for 24 h at 60 °C prior to use; same procedure was applied to MCC Avicel PH-101 that was purchased from Serva Co. (derived from wood pulp; ~50 μm particle size). 4-(Phenylazo)benzoyl chloride (≥ 98.0%) was purchased from Tokyo Chemical Industry Co. and used as received. Cellulose acetate (CA: $M_n \approx$ 30,000; calculated DS ≈ 2.5), 1-butyl-3-methylimidazolium chloride ([BMIM]Cl: 98%), *N*,*N*-dimethylacetamide (DMAc: ≥ 99.8%) and polyethylene oxide (PEO: $M_v \approx$ 400,000) were purchased from Sigma Aldrich Co. and used as received. Acetone (≥ 99.8%), tetrahydrofuran (THF: ≥ 99.8%), dichloromethane (DCM: ≥ 99.8%), *N*,*N*-dimethylformamide (DMF: ≥ 99.8%), and anhydrous pyridine (≥ 99.8%) were purchased from BioSolve Chimie Co. and used as received. Anhydrous pyridine and [BMIM]Cl were kept in MBRAUN® Workstation LABstar Eco glovebox that is filled with nitrogen gas (Gas purifier MB10G) to avoid moisture absorption (Figure II.1). A MedlineScientific® Jeio Tech OV-11 28 Litre vacuum oven was also utilized to dry polymer powders and fabrics overnight at temperatures ranging from 60 to 100 °C.

Figure II.1. MBRAUN® Workstation LABstar Eco glovebox.

Methods

Azo-Cel was synthesized according to previously reported methods [104,105] with minor modifications *via* esterification of MCC and 4-(phenylazo)benzoyl chloride (Scheme II.1). 1.12 g of MCC (Avicel PH-105 from FMC) was dispersed and dissolved into 100 mL of anhydrous pyridine at 100 °C. 5.00 g of 4-Phenylazobenzoyl chloride (3.3 mol equiv. to 1 mol anhydroglucose units (AGU) of cellulose) was dissolved into 100 mL of anhydrous pyridine at 100 °C as well, and then it was poured in one portion into the mixture of cellulose in pyridine. The reaction was carried out at 100 °C for 48 h at constant stirring, after which the reaction was stopped and the mixture was precipitated into an excess amount of ethanol and the precipitate was filtered. The product was purified using Soxhlet extractor with acetone for 48 h at 70 °C and vacuum dried at 70 °C for 24 h to yield a dark red-colored solid (4.21 g, 79.0% yield calculated based on the starting MCC).

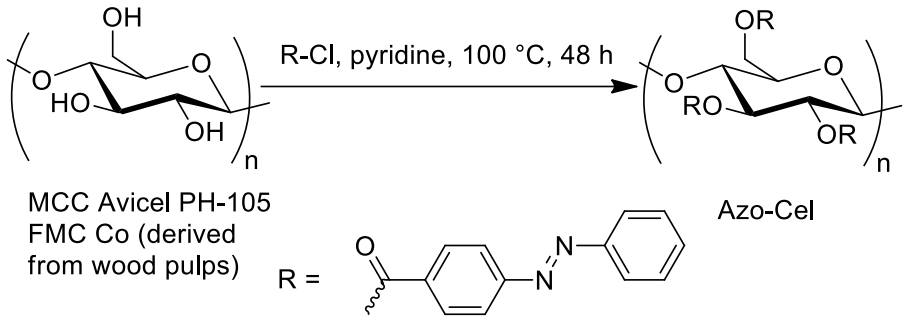

Scheme II.1. Synthesis of Azo-Cel *via* esterification of MCC and 4-phenylazobenzoyl chloride.

The ATR-FTIR spectra were obtained using a PerkinElmer 'Spectrum Two' spectrometer (Figure II.2). For each measurement either the polymer powder or the fabric would be placed in such a way that the surface of the product and the ATR crystal faced each other. The infrared light first goes through a crystal, then reflects at the crystal-sample interface and then it travels to the ATR-FTIR detector. Part of the infrared light goes through the sample and gets absorbed during this process of internal reflection, becoming the evanescent wave. The refractive index difference

between the sample and the ATR crystal determines the penetration depth of the evanescent wave into the sample [106]. The absorbance curves were acquired by PerkinElmer Spectrum software.

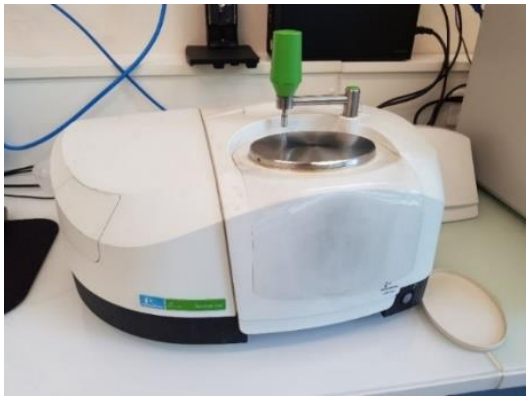

Figure II.2. ATR-FTIR spectrometer PerkinElmer 'Spectrum Two'.

The ^{1}H and ^{13}C spectra were recorded on Bruker Ultrashield 400 MHz instrument. The ^{13}C Cross-polarization/Magic angle spinning (CP/MAS) experiments were performed with a Bruker Avance III 400 MHz spectrometer that operated at 100.6 MHz. Each specimen was packed into a zirconia specimen rotor, which would spin at 12 kHz at 2 ms cross-polarization contact time Figure II.3 illustrates the instruments.

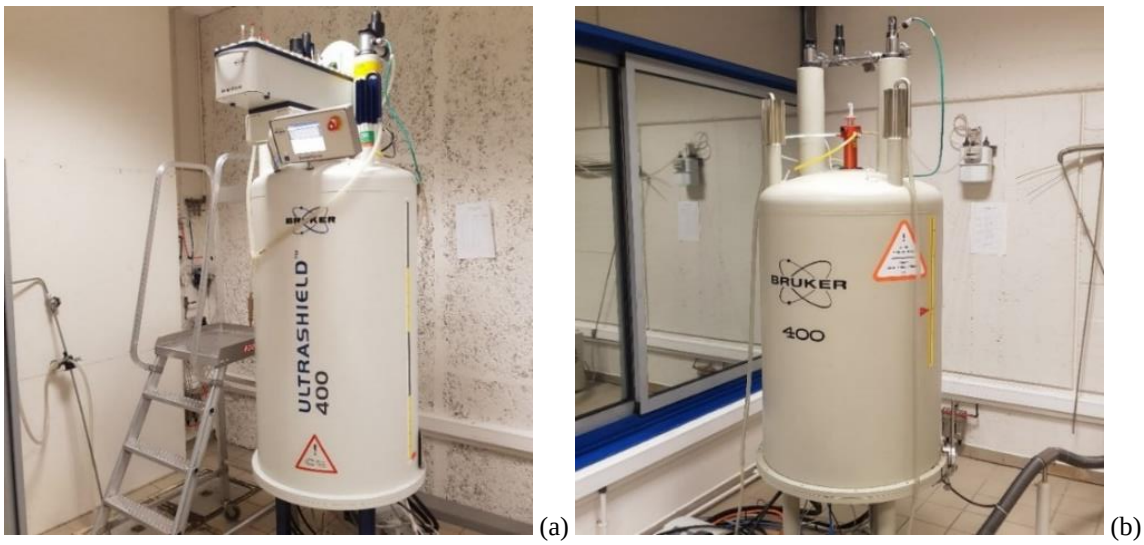

(a) (b)

Figure II.3. a) Bruker Ultrashield 400MHz NMR instrument used for liquid-state characterizations, and b) Bruker Avance III 400 MHz NMR instrument used for solid-state characterizations.

For ^{1}H NMR analysis, 5 mg of the sample was dissolved into 600 µL of a deuterated solvent suited for the analysis. The measurements were carried out at room temperature or at 80 °C (in case of trityl cellulose in DMSO-d_6) at 256 scans. For ^{13}C NMR analysis, 40 mg of the sample was dissolved into 600 µL of a deuterated solvent sited for the analysis. The measurements were carried out at room temperature or 80 °C (in case of trityl cellulose in DMSO-d_6) at 12,000 scans. Both ^{1}H and ^{13}C NMR spectra were acquired and treated on Bruker TopSpin® software.

The UV-vis adsorption spectra of Azo-Cel and Azo dye solutions in THF were measured by Varian® Cary 50 bio spectrophotometer (Figure II.4) at room temperature. For Azo dye, solutions of 0.015 g/L in THF were prepared; yet Azo-Cel solutions were prepared with the concentration of 0.03 g/L in THF. The UV-vis absorption spectra of the samples in a quartz cell with 1 mm path length were then measured by using Varian® Cary 50 bio spectrophotometer and the data was treated using Varian® Scan software.

Figure II.4. Varian® Cary 50 bio spectrophotometer [107].

TGA analysis was carried out by Setaram® TGA 92-12 thermogravimeter (Figure II.5). For each experiment, 20 mg of the sample (pre-dried at 70 °C under vacuum overnight) was placed inside a ceramic beaker and placed inside the thermogravimeter. The product would be conditioned at 20 °C for 300 s, and then heated to 500 °C under N_2 atmosphere at 10 °C/min heating speed. The data was analyzed *via* KaleidaGraph software.

Figure II.5. Setaram® TGA 92-12 instrument.

DSC analysis was carried out using a TA Instruments Q200 apparatus (Figure II.6). For each experiment, ca. 20 mg of the sample (pre-dried at 70 °C under vacuum overnight) was put inside an aluminum pan and sealed. The sample was firstly conditioned at 25 °C for 300 s then heated at 10 °C/min heating speed to a temperature slightly below the degradation temperature (T_d) determined by the TGA analysis, then kept for 60 s. After that, the sample was cooled down to 25 °C at 10 °C/min cooling speed. The same cycle of heating and cooling was repeated as the

second heating/cooling processes. The DSC chamber was filled with N_2 gas throughout the entire analysis. The data was analyzed by using TA Data Analysis software.

Figure II.6. TA Instruments Q200 DSC apparatus.

II.3. Results and Discussion

The chemical structure of Azo-Cel was characterized by ATR-FTIR and NMR analyses. Figure II.7 represents the ATR-FTIR spectra of Azo-Cel (shown in blue) and MCC (shown in red) for comparison. A broad absorption signal between 3500 and 3000 cm^{-1} for MCC corresponds to the stretching vibration of –OH groups. The absence of this signal at the same region on the spectrum of Azo-Cel, as well as the presence of three new signals for the absorption bands of C=O (1723 cm^{-1}), C=C (1603 cm^{-1}), and C–O (1258 cm^{-1}) that are corresponding to stretching vibrations of ester linkage (C=O and C–O) and aromatic group, strongly suggest the successful functionalization of cellulose with AB group *via* esterification.

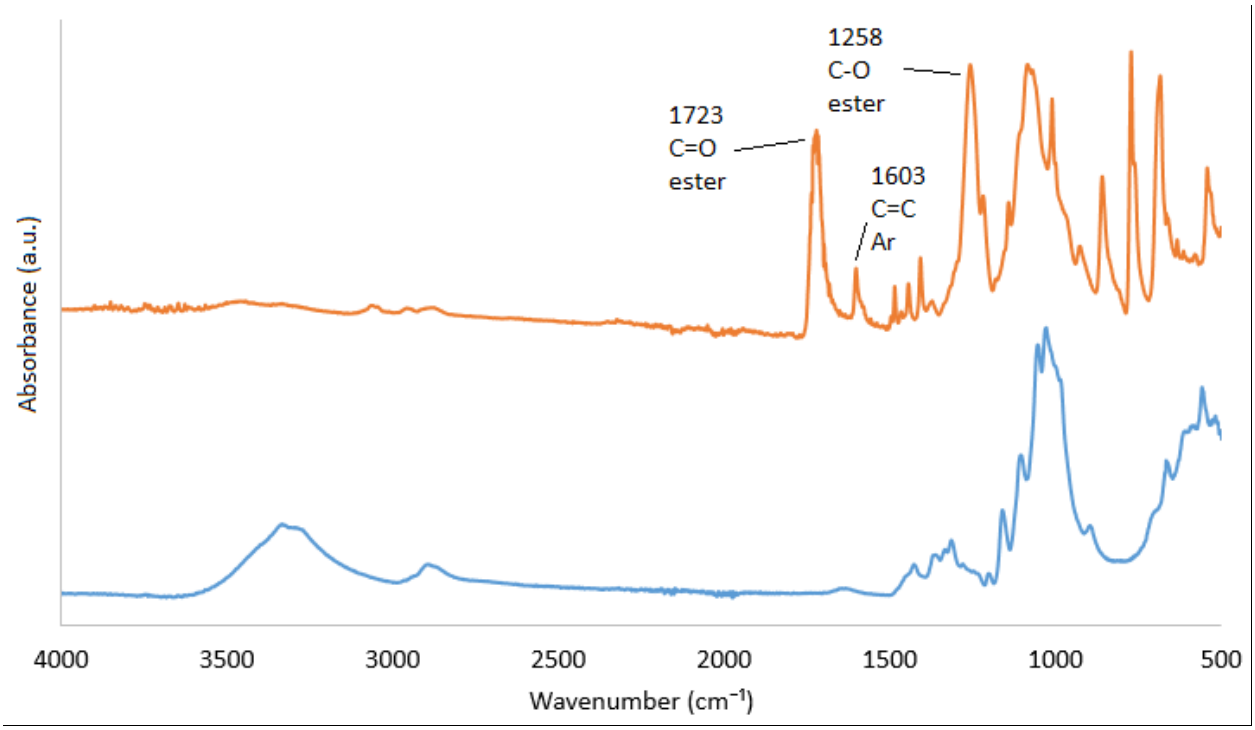

Figure II.7. ATR-FTIR spectra of Azo-Cel (orange) and MCC Avicel PH-105 (blue).

Azo-Cel was then characterized by NMR spectroscopy. For ^{1}H and ^{13}C liquid state NMR characterizations, respective solutions in $CDCl_3$ were prepared according to the previous sub-chapter. Figure II.8 represents the ^{1}H, ^{13}C, and ^{13}C CP/MAS spectra of Azo-Cel.

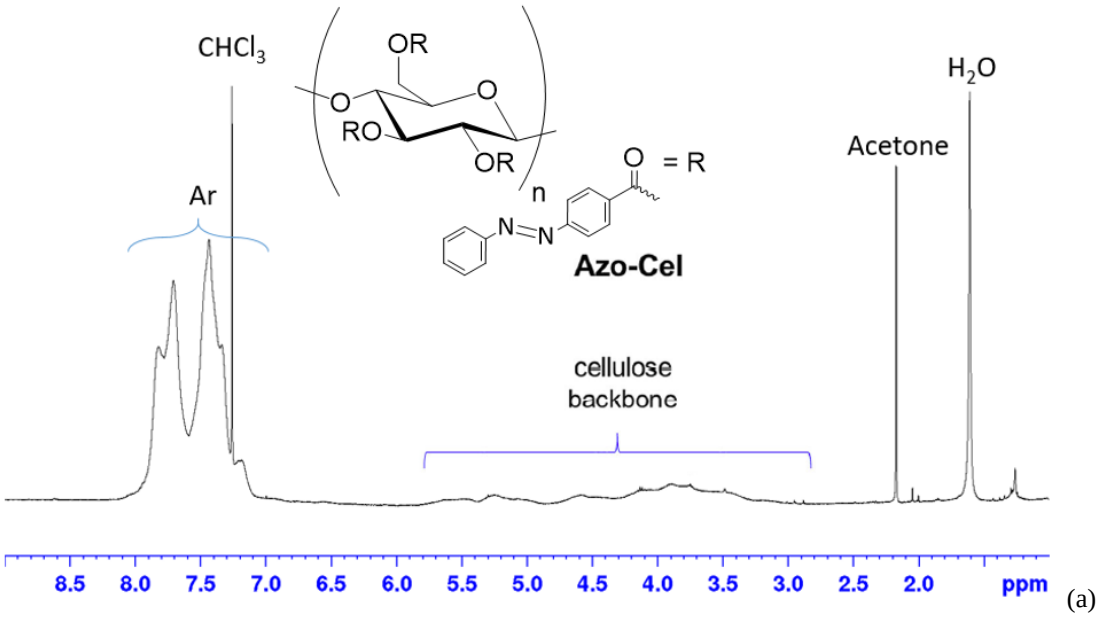

(a)

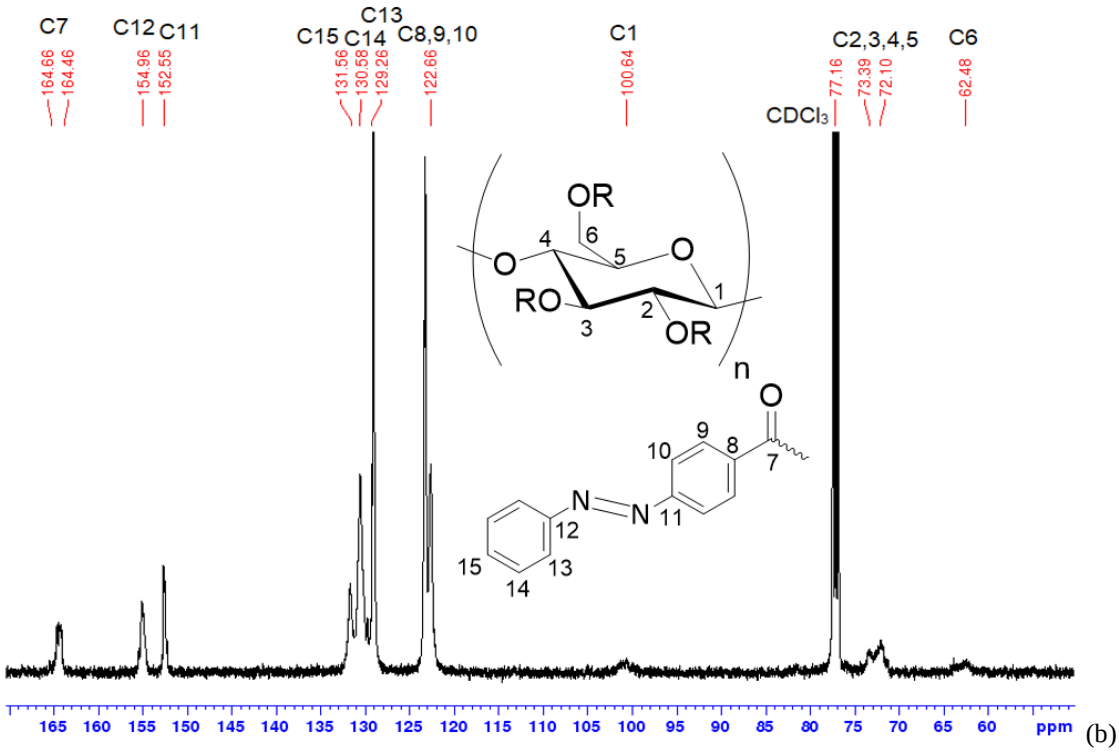

(b)

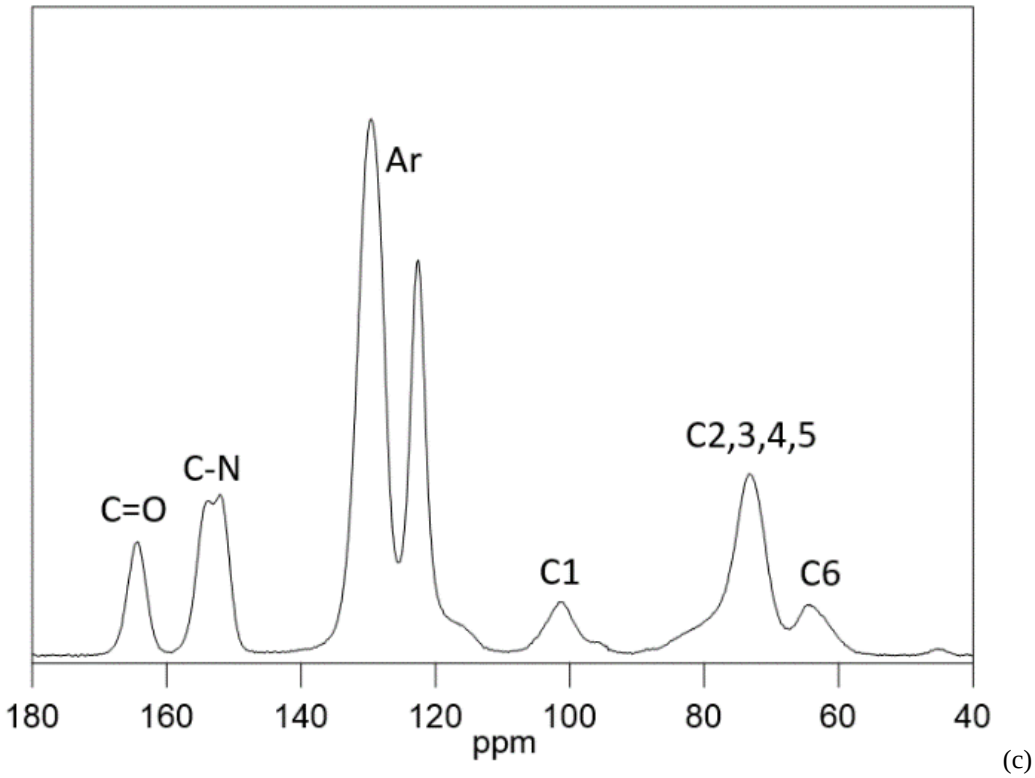

(c)

Figure II.8. a) ^{1}H NMR and b) ^{13}C NMR spectra of Azo-Cel in $CDCl_3$. c) ^{13}C CP/MAS solid-state NMR spectrum of Azo-Cel.

As shown in Figure II.8 a, the broad signal between 8.1 – 7.1 ppm corresponds to the aromatic protons of the AB moiety of Azo-Cel, accompanied by a broad signal around 5.8 – 2.7 ppm corresponding to the cellulose backbone protons. Results of ^{13}C NMR spectrum are in line with the reported results by Otsuka&Barrett [20], meaning new signals corresponding to Azo side groups have appeared on the NMR spectrum. On the ^{13}C CP/MAS NMR spectrum presented in Figure II.8 c, the broad band between 150 and 160 ppm belongs to the azo double bond, while the band between 160 and 168 ppm represents the ester linkage. From these results which are in good agreement with our previous Azo-Cel sample [20], the obtained product (IOC 1-260) was identified as Azo-Cel.

Azo-Cel product has almost 3 Azo side groups to 1 AGU (DS = 2.83 calculated by elemental analysis), that are chromophores and should respond to light stimuli. Therefore, the UV absorption spectral behaviors of Azo dye (4-(phenylazo)benzoyl chloride) and Azo-Cel in THF were studied by UV-vis spectral analysis (Figure II.9).

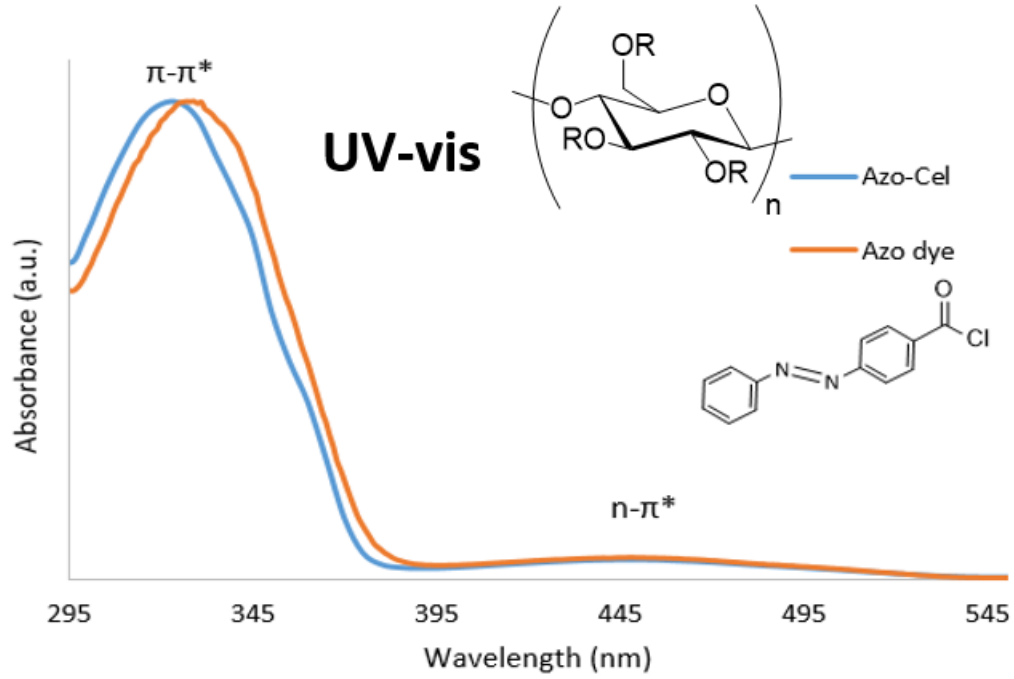

Figure II.9. UV-vis spectra of Azo dye and Azo-Cel.

The strong absorption bands between 300 and 380 nm corresponds to the π-π* electron transition of AB functional groups (λ_{max} = 324 nm for Azo-Cel and λ_{max} = 331 nm for Azo dye); whereas the weak broad absorption bands between 400 and 500 nm belongs to the n-π* electron transition of the AB moiety in the compound (λ_{max} = 445 nm for Azo-Cel and λ_{max} = 449 nm for Azo dye). A subtle shift in wavelength was observed between the two spectra of Azo-Cel and azo dye and the shift is more visible around 340 nm region where the π-π* electron transition of AB functional groups appear. It was estimated that this hypsochromic effect was due to the state of AB groups neighboring each other alongside the cellulose backbone, therefore resulting in a π-π stacking interaction that increases the electron density of the AB groups [20].

T_d of Azo-Cel was determined from the TGA curve shown in Figure II.10 with that of MCC for comparison.

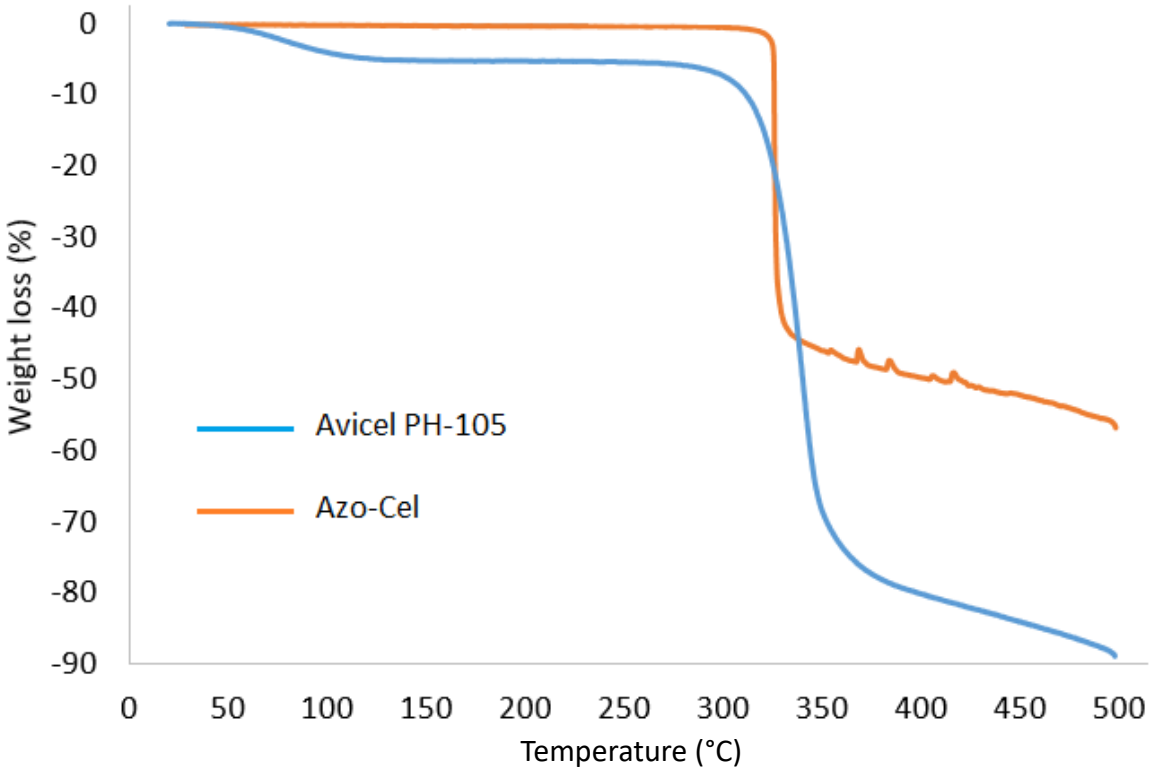

Figure II.10. TGA traces of MCC Avicel PH-105 (blue) and Azo-Cel (orange).

T_d of Azo-Cel was determined to be 286 °C, which was the temperature at which the polymer chains start to degrade, whereas the T_d of MCC was found to be 247 °C. This increase of T_d is due to the incapacity of Azo-Cel polymer chains to form inter/intramolecular hydrogen bonds that influence the thermal properties [108–113].

Figure II.11 illustrates the DSC profile of Azo-Cel. The graph shows a T_g at around 175 °C for Azo-Cel during the second cycle of heating, but no change of Heat Flow for cellulose.

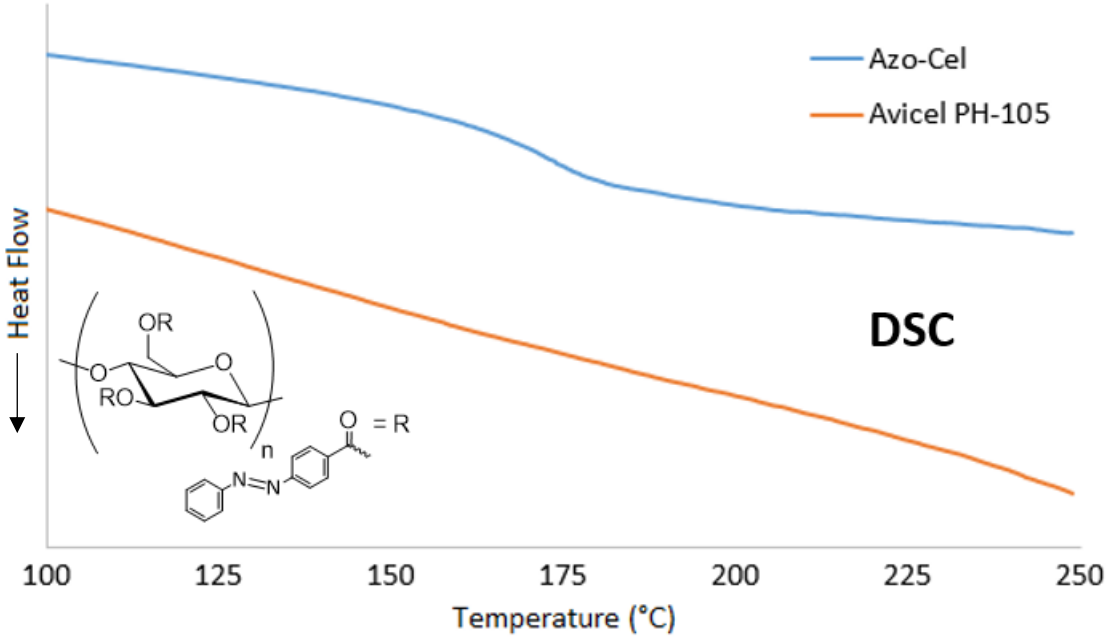

Figure II.11. DSC trace of Azo-Cel during the second heating cycle compared to starting cellulose.

II.4. Conclusion

Azo-Cel was successfully synthesized and its chemical structure was identified *via* ATR-FTIR and NMR analyses. UV-vis analysis of Azo-Cel showed that the AB moieties in the product are mostly consisted of *trans* isomers and a blue shift occurred after functionalizing MCC with azo dye. Td and Tg of Azo-Cel were found by TGA and DSC methods, respectively.

Chapter III : Electrospinning of Azo-Cel

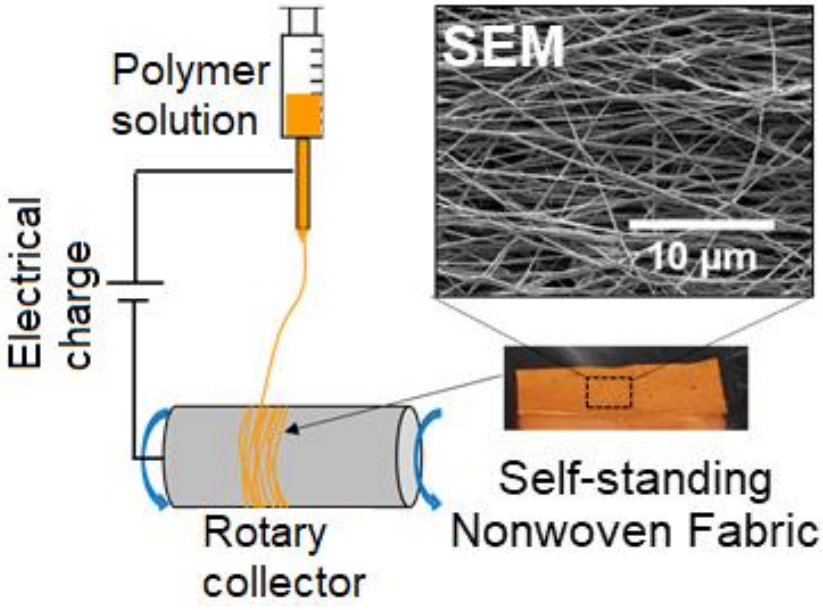

III.1. Introduction

Electrospinning is a versatile and simple method of continuous fiber production that uses strong electric fields to draw polymer solutions or melts with nano/micro scale diameters [114]. With this method, even complex structures such as core-shell, hollow, and porous nanofibers can be obtained [115]. A suitable solution that is able to fully solubilize the polymer must be chosen to electrospin micro/nanofibers from polymer solutions. A fine polymer-jet stretches from a droplet of polymer solution where the high voltage is applied. The jet is then collected on an electrode that is placed at a certain distance below, when the charge at the droplet surface overcomes the surface tension of the droplet. Hence, the solution is separated from the polymer because of the high tension caused by electrical charge, and the polymer threads are superimposed on the collector. It has been demonstrated that all electrospinning process variables, including the solution composition (polymer concentration and solvent ratios), applied voltage, tip-to-collector distance, and collector type, have an impact on the diameter and morphology of the resultant fiber [116]. This technique can also be used to develop advanced fibers for click chemistry, bioelectrochemical, and other various applications [117–119].

An electrospinning instrument is usually constructed of the following components:

1. Polymer placement compartment, a syringe, where the polymer solution is placed. Syringes come in various types; they can be made either of glass or polypropylene. To ensure the cleanness and precision of the polymer injection, a gas-tight syringe may be employed.
2. Tip of the needle placed right onto the syringe, where the solution is pushed out and electrical. The feed-rate explains the speed at which a certain volume of the polymer is fed to the system during a certain period of time. Feed-rate values are generally expressed by mL/h or µL/min.

3. Electricity generated that provides an electrical charge to the polymer solution, helping charge the solution and separating it from the polymer by the tension that it created, leading to evaporation and superimposition of the polymer threads on the substrate.
4. A collector (electrode) that can be flat or rotary. The flat electrode is utilized to obtain un-oriented fiber-mat, whereas the rotary electrode may be employed for better fiber alignment.
5. Other optional instruments such as a camera and a computer can be attached and inserted to the machine so that the supervision of the process could become easier. Scheme III.1 illustrates a general setup of an electrospinning apparatus.

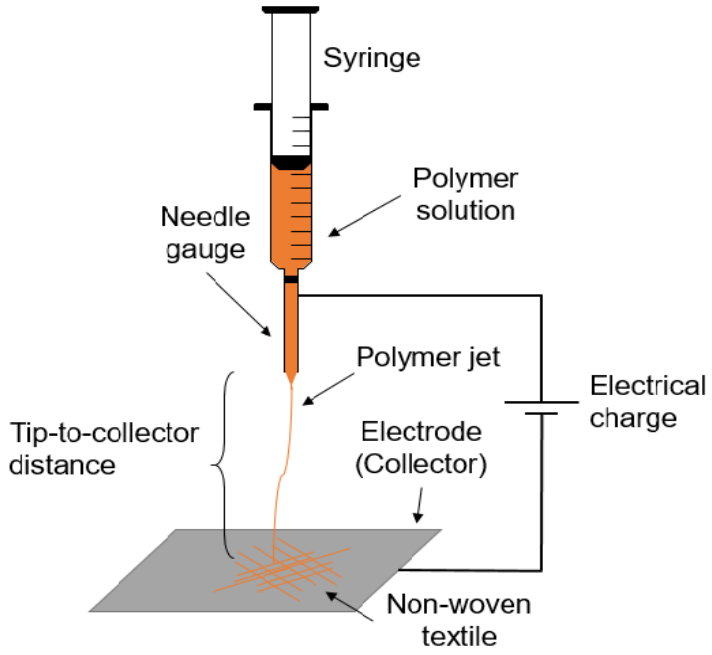

Scheme III.1. General setup of an electrospinning apparatus.

In this chapter the optimization of the electrospinning parameters such as feed rate, voltage, tip-to-collector distance, and most importantly polymer concentration and solvent ratios are discussed. The morphology of the products are studied by optical microscopy and SEM. The self-standing Azo-Cel textile was then produced by implementing the optimized parameters that are

obtained through our studies. In the same context, a self-standing textile of CA is produced and the fabric is used for a control experiment during UV-induced photo-actuation analysis.

III.2. Experimental

Materials

For this study, electrospinning was carried out by using a Fuence 'Esprayer ES-2000S2A' apparatus (Figure III.1) at room temperature (ca. 25 °C) and humidity (ca. 30%). The electrospun products were collected on two different types of metallic electrodes, namely a flat plate (20 cm × 20 cm) and a cylinder-shaped rotating drum (diameter: 10 cm; length: 15 cm) covered with Al foil. The electrodes were placed 15 cm below the tip of needle electrodes (Nordson stainless steel tips 18 GA (inner diameter = 0.84 mm) or 20 GA (inner diameter = 0.61 mm)). A high electric field (20-25 kV) was applied between the electrodes to draw polymer threads from the tip of the needle where polymer solutions were fed at various solution feed-rates (6.0-16.7 µL/min). The cylinder-shaped drum electrode was rotated at 1500 rpm to fabricate unidirectionally-aligned polymer fibers and their fabrics. To review solvents' characteristics used for electrospinning, refer to chapter II.2 *Materials* section.

Figure III.1. Electrospinning apparatus Fuence Esprayer ES-2000S2A. All functions are maneuvered by a computer that is connected to the instrument.

Methods

Self-standing Azo-Cel textile was fabricated *via* electrospinning of its polymer solution on a PEO transitory layer, on an Al foil. For this purpose, 10 mL of a PEO solution (4.5 wt% in deionized water) was first electrospun using a 20 GA needle under a 20 kV electric field at a 16.7 µL/min solution feed rate on a rotating drum electrode covered with Al foil. Then, 6 mL of an Azo-Cel solution (17 wt% in acetone/DMAc = 3/2 (v/v)) was electrospun on the same Al foil coated with the PEO textile using a 18 GA needle under 25 kV at 10 µL/min solution feed rate. Afterward, the Al foil coated with the double-layered "Azo-Cel on PEO" textile was removed from the drum electrode and cut into small pieces. The specimen was then immersed in deionized water, which is a good solvent of PEO but a non-solvent of Azo-Cel, to solubilize the PEO layer and detach the Azo-Cel layer from the Al foil without any physical pressure on the textile. After half a day, the PEO layer was completely dissolved and the Azo-Cel layer was detached from the Al foil as a floating textile that was dried under vacuum at 70 °C overnight to obtain a self-standing Azo-Cel fabric.

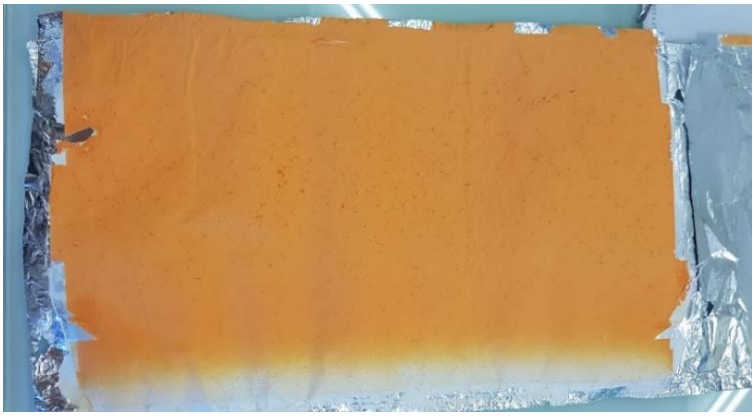
(a)

(b)

Figure III.2. a) Azo-Cel textile on PEO on Al foil. b) Self-standing Azo-Cel membrane separated and prepared for UV-induced photo-actuation analysis. The thickness of the Azo-Cel fabric (compressed form: ≈ 11 µm) was measured with a Mitutoyo Digital Vernier scale IP65.

In order to prepare self-standing CA textile for the UV-induced photo-actuation control experiment, CA was directly electrospun onto an Al foil because the electrospun CA textile did not strongly adhere to the Al foil and was easily detachable from the foil without damaging it. Therefore, 6 mL of a CA solution (17 wt% in acetone/DMAc = 2/1 (v/v)) was electrospun using a 20 GA needle 15 cm above a drum collector that would rotate at 1500 rpm covered with Al foil, under 20 kV at 10 μL/min solution feed rate. The Al foil coated with CA textile was removed from the drum electrode and cut into small pieces. The CA textile was carefully peeled-off from the Al foil using tweezers to obtain a self-standing CA fabric.


(a)
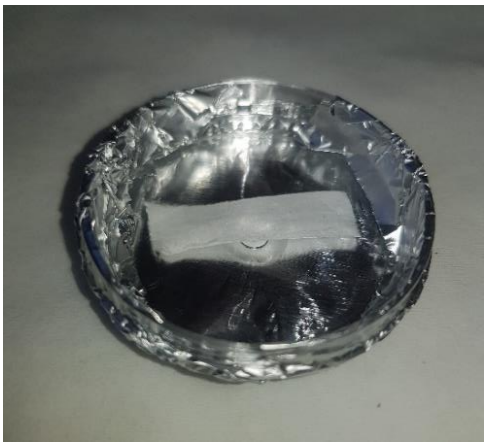
(b)

Figure III.3. a) CA textile on Al foil on rotary drum collector. b) Self-standing CA membrane prepared for UV-induced photo-actuation analysis.

III.3. Results and Discussion

During this study, over 200 electrospinning tests have been conducted in order to optimize the process parameters for Azo-Cel. During all these processes, change of parameters that can affect the morphology of the products have been investigated. These parameters include feed-rate, electrical charge, polymer concentration, the choice of solvent systems and ratios of different

solvents. For each process, a glass slide was inserted right down of the tip of the needle and on the Al foil for the optical microscopic analysis.

In a similar case, and at the beginning of this project, studied the electrospinning of CA (similar polymer as Azo-Cel, having AGUs as polymer backbone and acetyl side groups) in different solvent systems was studied to acquire a basic understanding of the process, as well as the effects of solvent systems on the morphology of products. Table III.1 describes the CA solutions prepared in detail.

Table III.1. CA solutions for electrospinning and study of solvent systems.

Number	Solvent system	Solvent ratio	Polymer concentration (wt%)	Reference
1	DCM/MeOH	4/1 v/v	12	Celebioglu et al., 2014 [120]
2	Acetone/DMSO/Acetic acid	62/31/7 wt%	18	Nicosia et al., 2016 [121]
3	Acetone/DMAc	3/2 wt/wt	20	Inukai et al., 2018 [122]
4	Acetone/DMAc	2/1 v/v	17	Tidjarat et al., 2014 [123]
5	DCM/Acetone	3/1 v/v	7.5	Ma et al., 2017 [124]
6	DCM/DMF	9/1 v/v	10	Otsuka & Barrett 2019 [20] *
7	DCM/DMF	7.5/2.5 v/v	10	Otsuka & Barrett 2019 [20] *

* Originally the electrospinning of "Azo-Cel" in DCM/DMF was discussed in this source, but in the current study CA replaced Azo-Cel to compare solvent systems together regarding a single polymer.

Electrospinning of each product was carried out according to its literature reference. Product number 1 was prepared by injecting the solution from a 20GA needle gauge at 15 kV electrical field, and at 16.7 µL/min (1 mL/h) feed-rate 10 cm above a flat collector covered with Al foil, presented in Figure III.4 a. Using a rotary drum collector showed an improvement of fiber alignment as described in Figure III.4 b.

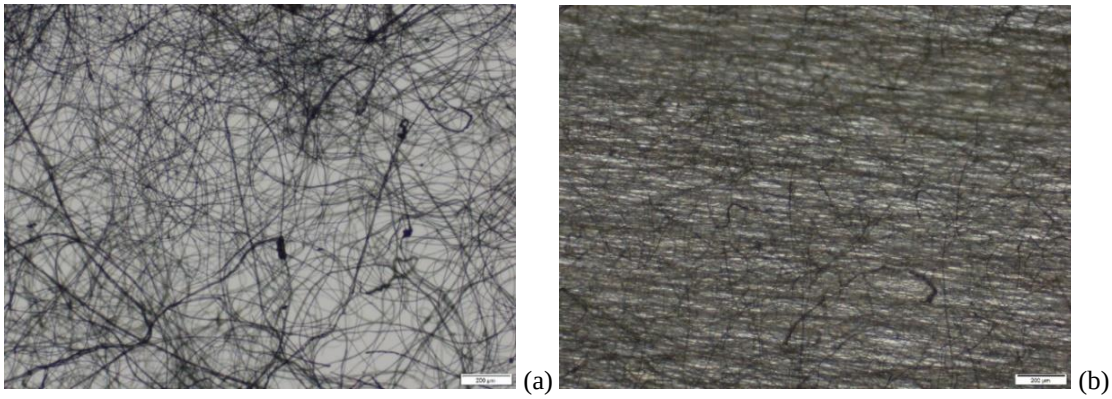

Figure III.4. Optical micrographs of CA electrospun product no.1. a) randomly-assembled fibers collected on a flat electrode and b) fibers gathered on a drum rotary electrode with 3000 rpm rotational speed. (Scale bar for both images = 200 µm).

During both electrospinning processes the polymer was aggregated at the tip of the needle, and after a while the aggregates were projected onto the surface of the collector due to the high electric field. Therefore, the DCM/MeOH solvent system was considered an unstable system for the future of the study. Additionally, employing a rotary drum collector for a better aligned fiber assembly was shown to be an effective technique. Product number 2 was prepared by injecting the solution from a 20GA needle gauge at 18 kV electrical field, and at 16.7 µL/min (1 mL/h) feed-rate 15 cm above a flat collector covered with Al foil, presented in Figure III.5. Same phenomenon of aggregation at the tip of the needle and projection onto the surface of the collector occurred to product no. 2 as it did to the previous sample.

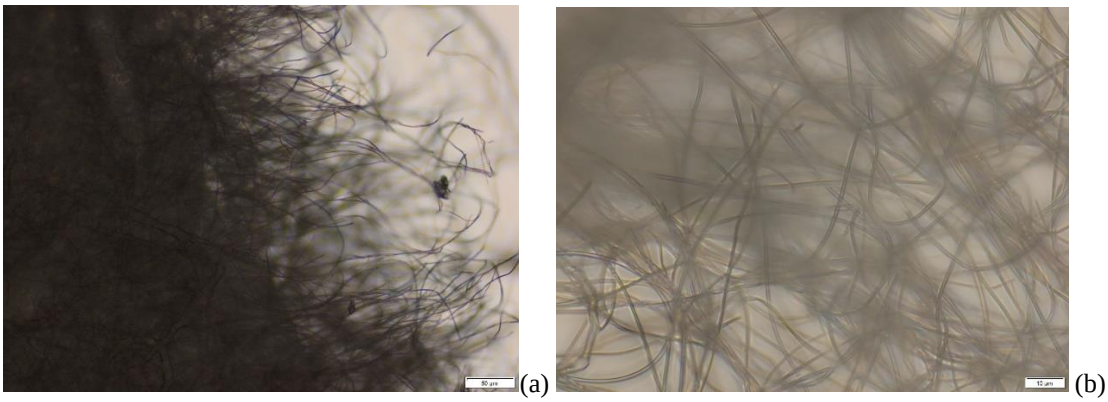

Figure III.5. Optical micrographs of CA electrospun product no.2. a) Scale bar = 50 µm, and b) Scale bar = 10 µm.

Product number 3 was prepared by injecting the solution from a 21GA needle gauge at 18 kV electrical field, and at 10 µL/min feed-rate 10 cm above a flat collector covered with Al foil, presented in Figure III.6 a. In retrospect, product number 4 was electrospun by injecting the solution from a 21GA needle gauge at 18 kV electrical field, and at 10 µL/min feed-rate 10 cm above a flat collector covered with Al foil, presented in Figure III.6 b. Both processes showed good electrospinnability, process stability and no aggregation at the tip of the needle.

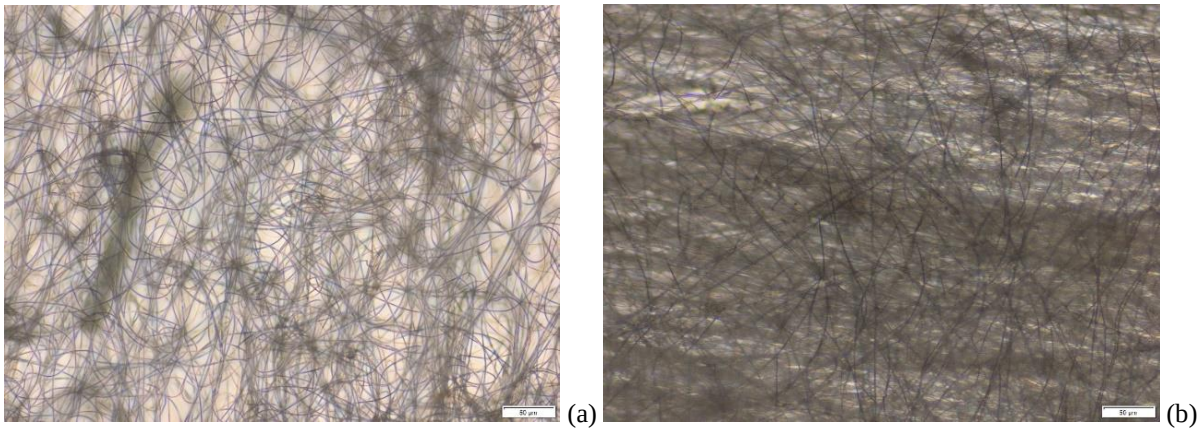
(a) (b)

Figure III.6. Optical micrographs of CA electrospun products: a) product no 3. b) product no 4. Scale bars = 50 µm.

Product number 5 was prepared by injecting the solution from a 20GA needle gauge at 25 kV electrical field, and at 50 µL/min (3 mL/h) feed-rate 15 cm above a flat collector covered with Al foil, presented in Figure III.7. The solution aggregated at the tip of the needle and whenever the aggregate was heavy enough, it was projected onto the surface of the product because of the high tension caused by the electric field.

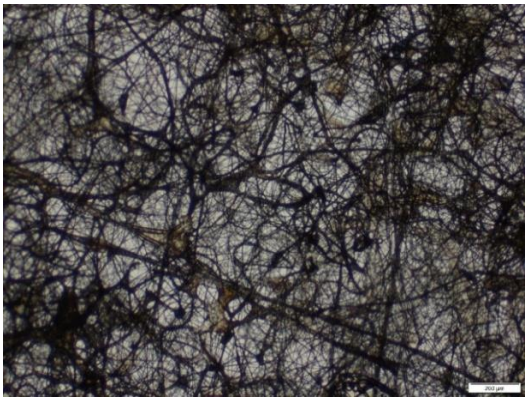
(a)
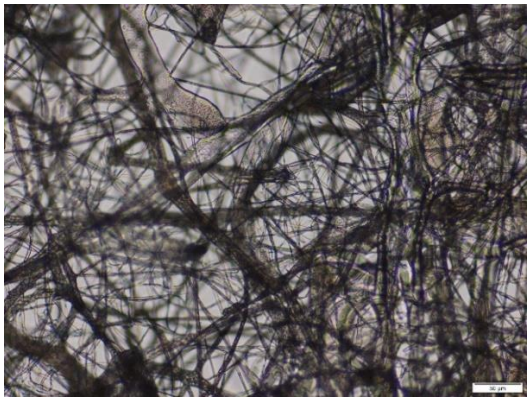
(b)

Figure III.7 Optical micrographs of CA electrospun product no.5. a) Scale bar = 50 µm, and b) Scale bar = 10 µm.

Products number 6 and 7 were electrospun by injecting their respective solutions from a 20GA needle gauge at 20 kV electrical field, and at 50 µL/min (3 mL/h) feed-rate 15 cm above a flat collector covered with Al foil. Figure III.8 a and b present optical micrographs of products number 6 and 7 respectively.

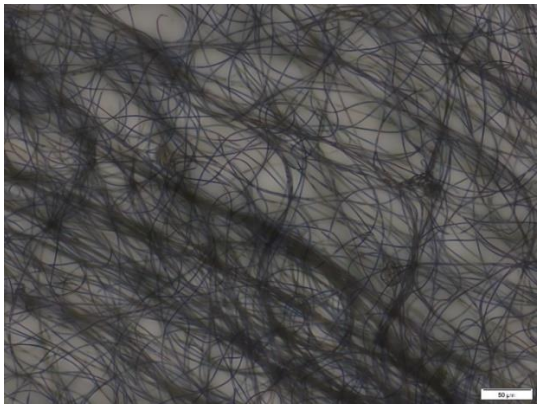
(a)
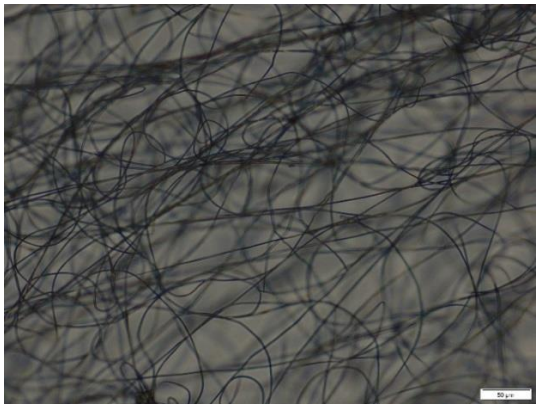
(b)

Figure III.8. Optical micrographs of CA electrospun products: a) product no. 6, and b) product no. 7. Scale bar = 50 µm.

As it occurred to the previous solvent systems, products 6 and 7 produced aggregates at the tip of the needle. It appears that the acetone/DMAc solvent system was the most reliable system that gave the best electrospinning stability and less aggregation, perhaps because of the vapor

pressure of each solvent and the use of "high volatile & poor solvent mixed with low volatile but good solvent". Therefore it was chosen as a candidate for the electrospinning of Azo-Cel. Yet other solvents could be tried to ensure that Azo-Cel reacts the same was as CA in a chosen solvent system.

The effect of tip-to-collector distance on the morphology of the products was studied as well. A solution of 17 wt% Azo-Cel in acetone/DMAc 1/1 v/v was prepared and electrospun by injection from an 18GA needle gauge at 25 kV electrical field, and at 50 µL/min (3 mL/h) feed-rate on a flat collector covered with Al foil. The first product (labelled ES-31-2) was prepared at 10 cm tip-to-collector distance, while the second product (ES-32-1) was electrospun at 15cm. Figure III.9 presents the optical micrographs of the two products.

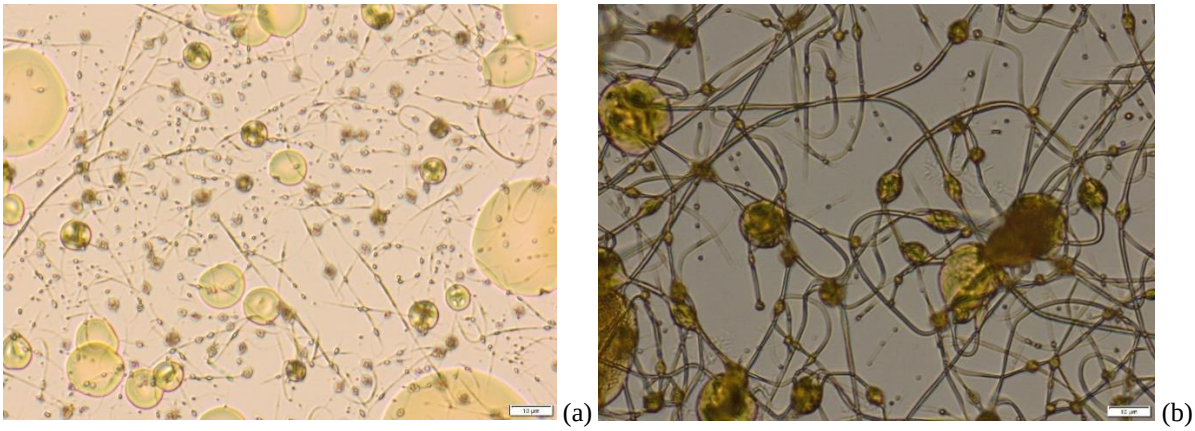
(a) (b)

Figure III.9. Optical micrographs of a) ES-31-2 (at 10 cm) and b) ES-32-1 (at 15 cm). The scale bar for both images is 10 µm.

Judging by the optical micrographs presented in Figure III.9, it appears that an increase of tip-to-collector distance led to fibers that are more continuous. This is because of the fact that the high tension caused by electrical field has a direct effect with the tip-to-collector distance; meaning that by increasing the tip-to-collector distance, the electrical charge must increase as well to keep

the quality of the nanofibers the same [125]. In another term, the polymer threads travel a longer distance and have more time to transform into continuous fibers at a constant electrical charge.

To study the effect of feed-rate on the stability of the electrospinning process as well as the morphology of the final product, a solution of 17 wt% Azo-Cel in acetone/DMAc 1/1 v/v was prepared and electrospun by injection from an 18GA needle gauge at 25 kV electrical field 15 cm above a flat collector covered with Al foil. The first product (labelled ES-34-3) was injected at 75 µL/min, while the second product (labelled ES-34-4) was injected at 30 µL/min. Figure III.10 presents the optical micrographs of these two products.

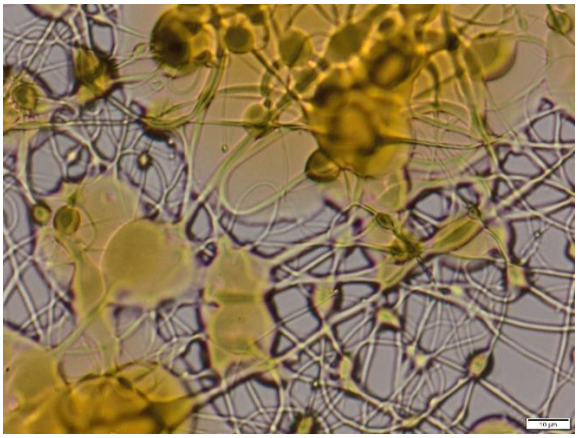
(a)
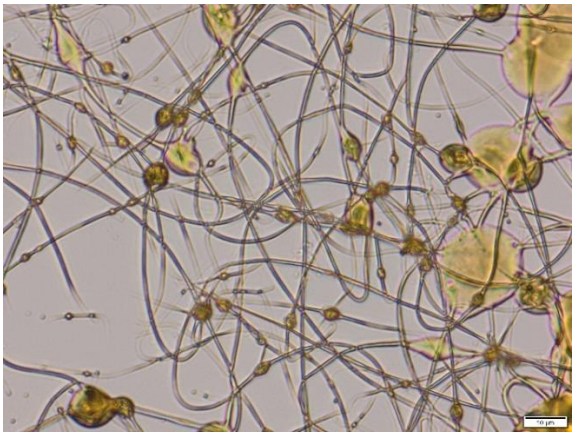
(b)

Figure III.10. Optical micrographs of a) ES-34-3 (at 75 µL/min) and b) ES-34-4 (at 30 µL/min). The scale bar for both images is 10 µm.

Interestingly, when the polymer was injected at high feed-rate of 75 µL/min, there was an enormous amount of polymer droplets and agglomerates that were injected alongside the fibers on the Al foil. However, once the feed-rate was decreased to 30 µL/min, the electrospinning process became more stable, meaning there were by far fewer droplets and aggregates/agglomerates projected on the surface of the product. This is because of the fact that at a constant electric field, higher feed-rate results in a higher quantity of polymer solution to come in contact with the high

tension of electric field, resulting in a higher portion of the polymer not being impacted by the electric field, hence droplets of polymer solution being drawn onto the surface of the product.

Additionally, the effect of electric field was studied on the electrospinnability of Azo-Cel. A solution of 17 wt% Azo-Cel in acetone/DMAc 1/1 v/v was prepared and electrospun by injection from an 18GA needle gauge at 30 µL/min feed-rate 15 cm above a flat collector covered with Al foil. The first product (labelled ES-33-2) was injected at 20 kV electric field, while the second product (labelled ES-34-1) was injected at 25 kV and the third product (labelled ES-34-2) was injected at 30 kV electric field. Figure III.11 presents the optical micrographs of these three products.

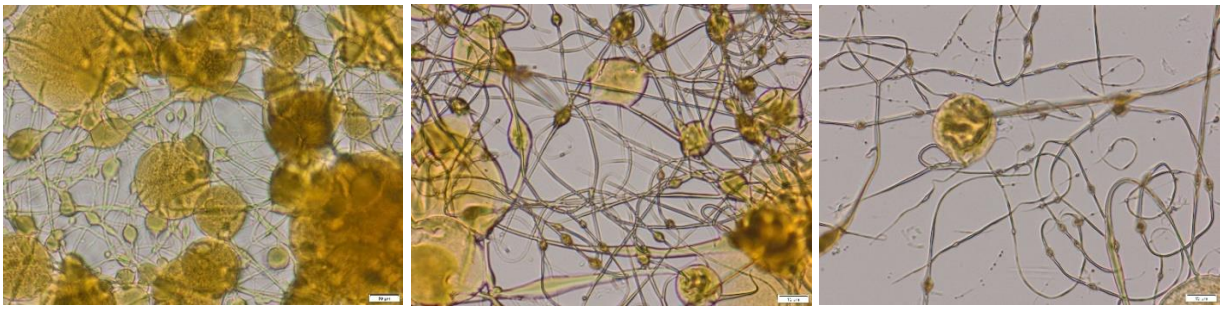

Figure III.11. Optical micrographs of 17 wt% Azo-Cel products in acetone/DMAc 1/1 v/v, applied at 20 kV (left), 25 kV (middle), and 30 kV (right). The scale bars for all three images are 10 µm.

As presented in Figure III.11, insufficient electric field results in more polymer droplets injected onto the surface of the product. In contrast, an increase of the electrical charge from 20 to 25 kV results in more polymer threads to form fibers and a decrease of beads and droplets (Figure III.11 middle). A further increase of electrical charge from 25 to 30 kV results in even fewer beads and more fibers to emerge (Figure III.11 right). Although an increase of electrical charge might be beneficial for a particular solvent system and product, an excess of electric field could result in an imbalanced surface of the product and thickness variation for the product.

SEM observations were required to characterize the morphology of the electrospun products in high resolution. Figure III.12 presents the SEM images of the electrospun products from Azo-Cel solutions in DCM/DMF solvent system with different polymer concentrations and solvent ratios. Previously, Otsuka and Barrett reported the effect of the solvent ratio of DCM/DMF at fixed polymer concentration (10 wt%) on the morphology of the fibers [19]. Hence, we have studied the effect of the polymer concentration at different solvent ratio of DCM/DMF, as well as the acetone/DMAc solvent system. As it is clearly observable in the images the electrospun products from the 8 wt% solutions (Figure III.12 a, b, c) show bead-like structure regardless of their solvent ratio probably due to their low viscoelasticity. Low viscosity leads to a quicker evaporation of the solvent while the polymer threads are being drawn by electrical charge, and a quicker evaporation of the solvent means polymer threads will not have enough time to form fiber and eventually they are drawn as beads on the surface of the collector.

By increasing the polymer concentration to 10 wt%, fine fibrous structure was observed with a small amount of beads for the solvent ratio of DCM/DMF = 1/1 (v/v) (Figure III.12 d) and without beads for that of DCM/DMF = 3/1 (Figure III.12 e) and 9/1 (v/v) (Figure III.12 f). Further increase of the concentration to 12 wt% gave, however, a negative effect for electrospinnability, *i.e.* the solutions tended to be agglomerated at the tip of the needle and consequently, the solutions stuck within the needle and form some beads (DCM/DMF = 1/1) (Figure III.12 g) or less amount of fibers (DCM/DMF = 3/1) (Figure III.12 h) were gathered on the substrates. At higher ratio of volatile DCM (DCM/DMF = 9/1), the solution was quickly stuck within the needle prior to applying high tension and nothing was gathered on the substrates.

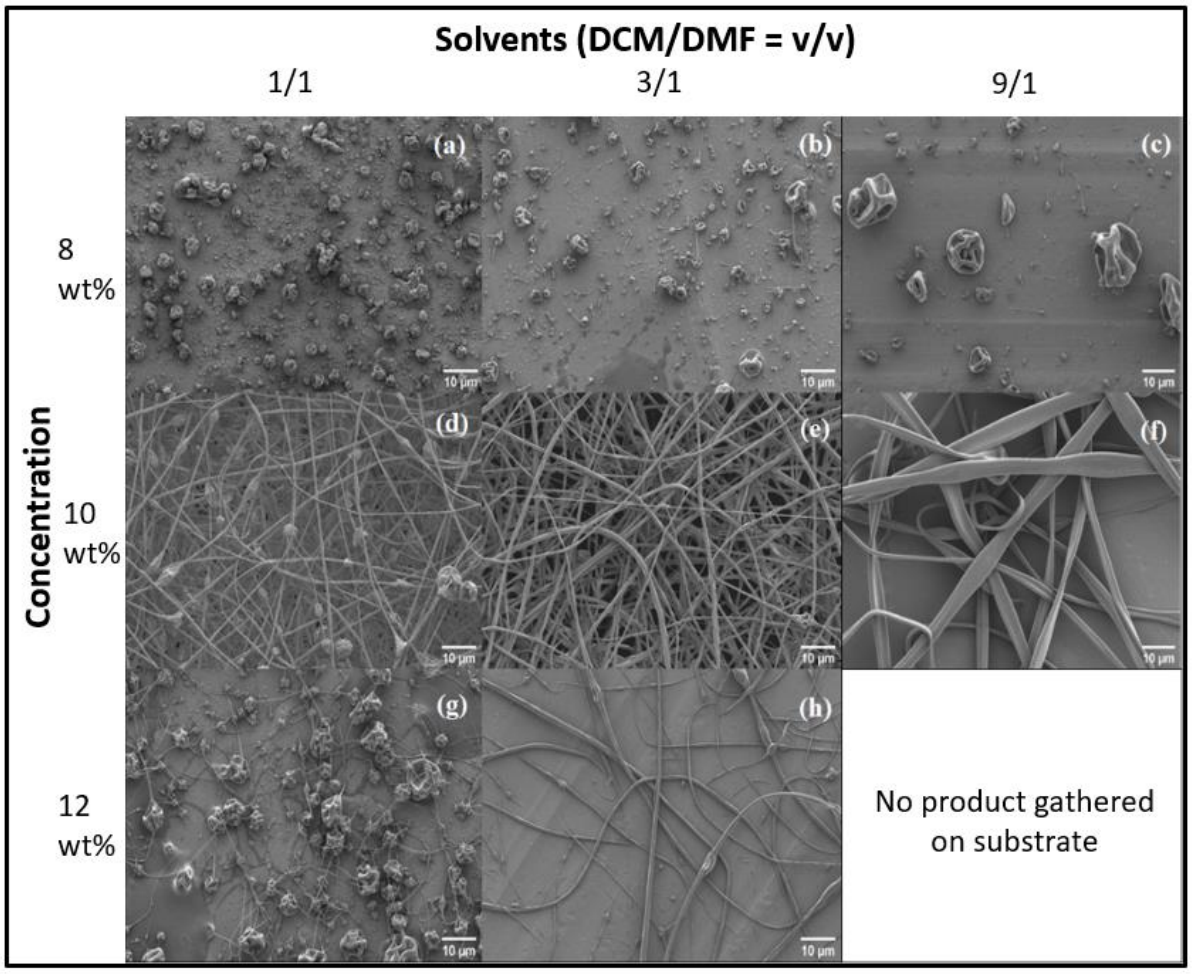

Figure III.12. SEM observations of the electrospun products from the Azo-Cel solutions in DCM/DMF solvent system with different polymer concentrations and solvent ratios.

Previously, Otsuka and Barrett reported the synthesis of Azo-Cel, its photo-responsive properties in solution, and a preliminary exploration of its successful electrospinning [19]. In the previous study, they found that a mixture of high-volatile and low-volatile good solvents at a certain ratio, *i.e.*, a mixture of dichloromethane (DCM: boiling point (bp) = 39.6 °C, vapor pressure (vp) = 47.1 kPa at 20 °C) and *N*,*N*-dimethylformamide (DMF: bp = 153 °C, vp = 0.516 kPa at 20 °C) with the volume ratio of DCM/DMF = 3/1, provided a stable electrospinning process of Azo-Cel to form continuous nanofibers when the polymer concentration was fixed to 10 wt%. However,

this solvent system was not optimal for longer duration electrospinning processes to from self-standing thick fabrics, because the polymer solution tended to agglomerate on the tip of the needle electrodes and impeded the polymer feed. Therefore, we explored other solvent systems to avoid this problem. Interestingly, mixing high-volatile poor solvents with low-volatile good solvents successfully prevented the agglomeration of Azo-Cel on the tip of the needle electrodes. Among various combination of the solvents, a mixture of high-volatile acetone (bp = 56.0 °C, vp = 30.0 kPa at 20 °C), a poor solvent of Azo-Cel, and a low-volatile *N*,*N*-dimethylacetamide (DMAc: bp = 165 °C, vp = 0.33 kPa at 20 °C), a good solvent of Azo-Cel, provided a consistently stable electrospinning process without agglomeration.

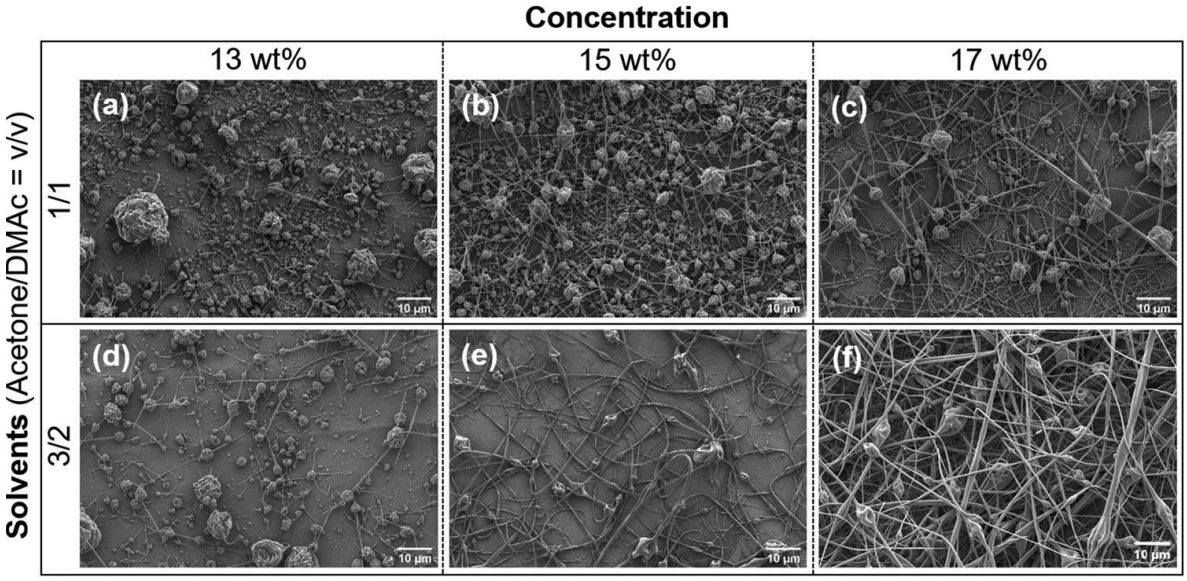

Figure III.13. SEM images of the electrospun products obtained from the Azo-Cel solutions in mixtures of acetone and DMAc with different volume ratios and concentrations: the products from (upper row) acetone/DMAc = 1/1 (v/v) solutions with a) 13 wt%, b), 15 wt%, and c) 17 wt%, and (lower row) acetone/DMAc = 3/2 (v/v) solutions with d) 13 wt%, e), 15 wt%, and f) 17 wt%.

Figure III.13 presents SEM images of the electrospun products from Azo-Cel solutions in the mixture of acetone and DMAc with volume ratios of acetone/DMAc = 1/1 and 3/2 and

concentrations 13, 15, and 17 wt%. As presented in Figure III.13 a,d, the electrospun products from the 13 wt% solutions displayed spherical beadlike structures regardless of their solvent volume ratios, probably because the viscosities and/or the surface tensions of the polymer solutions were insufficient against the applied electrostatic force so that the polymer solutions quickly sprayed away from the tip of the needle in the form of spherical droplets. By increasing the concentration to 15 wt %, a number of fibers coexisting with spherical beads were formed as shown in Figure III.13 b,e. One notes that increasing the volume ratio of acetone/DMAc from 1/1 to 3/2 tended to suppress the formation of spherical beads. A further increase of the concentration to 17 wt% (above this concentration, the polymer solution coagulates) fostered the formation of continuous fibers as presented in Figure III.13 c,f although some spherical and spindle beads still existed. Consequently, we chose acetone/DMAc = 3/2 (v/v) and 17 wt% as the optimal condition for the preparation of the self-standing Azo-Cel fabric.

One of the key steps to obtain self-standing fabrics *via* electrospinning is the process of detaching the textile from the substrate (aluminum (Al) foil in most cases). A preliminary test of electrospinning Azo-Cel directly on an Al foil showed that the resulting Azo-Cel textile strongly adheres to the Al foil, making it difficult to detach the textile without damaging it. To avoid this technical problem, a water soluble polymer, polyethylene oxide (PEO), was first electrospun on an Al foil followed by Azo-Cel to prepare a double-layered "Azo-Cel on PEO" textile on the Al foil. As Azo-Cel is not soluble in water, this double-layered textile on the Al foil was immersed in water to selectively solubilize the PEO layer that serves as a form of adhesion promotion layer between the Al foil and the Azo Cel textile. In this way, the Azo-Cel layer was successfully detached from the Al foil without damage as a floating textile on the water.

III.4. Conclusion

Electrospinnability of Azo-Cel has been studied in this chapter. Firstly, electrospinning of CA was studied and the effects of using a flat or rotary collector, as well as electrical charge, solution feed-rate, and tip-to-collector distance were thoroughly discussed. Then, the electrospinning of Azo-Cel was studied in two chosen systems of DCM/DMF and acetone/DMAc with various solvent ratios and polymer concentrations. The reason for which the electrospinning of CA was studied prior to that of Azo-Cel and the same solvent systems were applied is the fact that both polymers share the same cellulosic backbone with a slightly different side groups. Therefore they would be somewhat similar in terms of electrospinning. Further results have proven this statement to be correct and the solvent systems to be viable for the electrospinning of Azo-Cel.

The solvent system of acetone/DMAc was chosen to produce self-standing textile because it ensured the stability of the electrospinning process more than DCM/DMF. At last, the self-standing Azo-Cel textile was produced by electrospinning of a solution of 17 wt% Azo-Cel in acetone/DMAc 3/2 (v/v) on a rotary drum collector. It was electrospun on a layer of already prepared PEO on Al foil in order to avoid damaging the fabric and to facilitated the removal of the self-standing textiles by immersing it into water and dissolving PEO. Based on the result found during this project, varying the DP of the polymer can lead to a change in electrospinnability. The higher the DP of the polymer, the less stable the electrospinning and more difficult the acquisition of micro/nanofibers.

Chapter IV : Physical and Thermal Characterization of Azo-Cel Textile

Setup of Shimadzu “AGS-X” tensile machine.

IV.1. Introduction

Electrospun nanofibers, and specially those that are polysaccharide-based, demonstrate notable capabilities in a variety of scientific and technological domains including mechanics, thermodynamics, optics, etc, due to their increased surface area, as well as efficient porosity for energy storage applications [19,126–129]. In spite of polysaccharides' distinctive properties, electrospinning them has proven to be a difficult task because of their complex macromolecular structures and relatively low solubility in common organic solvents. Chemical and structural alterations can be used to tailor the porosity, mechanical durability, oxygen permeability, and hydrophilicity of fibrous membranes to meet practical requirements [130].

Modern high-tech sector utilizes fiber-reinforced polymer composites to develop various kinds of structures, including pressure tanks, vehicle body panels, and floor assembly, where the composite must endure a variety of static and dynamic tensions [131]. These tensions may be categorized as tensile, impact, ballistic, or fatigue loads [132]. This is why studying the tensile strength of Azo-Cel is a key component to a better understanding of the product. Xie and colleagues [185] report that implementing a rotative electrode and acquiring more aligned fibers increases the tensile properties of the fabric. As this difference of tensile properties between random and aligned fibers have already been studied, current results focus on the properties of the self-standing Azo-Cel textile that is consisted of aligned fibers.

In this chapter, the physical and thermal properties of Azo-Cel are discussed. These subjects include tensile strength, thermal annealing, X-ray diffraction, and confirmation of the chemical structure of Azo-Cel self-standing fabric by ATR-FTIR.

IV.2. Experimental

The mechanical properties in terms of the tensile strength and the strain at maximum of the self-standing fabrics were investigated using a Shimadzu "AGS-X" tensile testing machine (Figure IV.1 a) with a load cell of 20 N at a gauge length of 2 cm and a clamp moving speed of 0.2 mm/min according to the "ISO 13934-1" procedure[133]. The Azo-Cel fabric (DS ≈ 2.83, electrospun from acetone/DMAc 3/2 v/v at 25 kV, 18GA needle gauge, 15 cm distance and 10 µL/min feed-rate) was cut into a rectangular shape (3 × 0.5 cm^2) in such a way that the long axis is parallel to the orientation of the principal fiber axis. As the Azo-Cel fabric was too thin to hold tightly on the clamp, the fabric was sandwiched between two paper frames as a sample holder being clamped for testing. Both sides of the sample holder were then cut with scissors before starting measurements (Figure IV.1 b). Experiments were monitored and the data are acquired through TrapeziumX software.


(a)

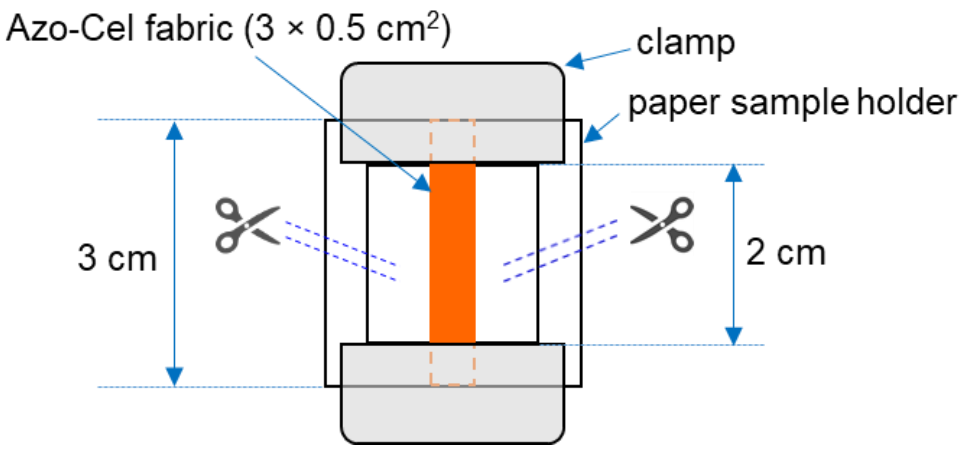

(b)

Figure IV.1. a) Shimadzu "AGS-X" tensile testing machine (with an Azo-Cel fabric between the clamps). b) Schematic illustration of the self-standing Azo-Cel fabric sandwiched with the paper frames as the sample holder being clamped for tensile testing.

The tensile strength of the Azo-Cel fabric was calculated according to the following equation:

$$\delta = \frac{F}{A}$$

where δ is the tensile stress (MPa), F is the stretching force (N) applied to the fabric in vertical sense, and A is the cross-section area (mm^2) of the specimen. Here, A was determined by multiplying the thickness to the width (0.5 cm) of the specimen assuming that the cross-section of the fabric is a rectangle. Thickness of each textile would be measured both by SEM to measure the uncompressed value, as well as the Vernier scale to measure the compressed values (Figure IV.2).

Figure IV.2. Thickness of the compressed textile was manually measured by Mitutoyo Digital Micrometer IP65 Vernier scale.

Azo-Cel fabrics were thermally annealed in MedlineScientific® Jeio Tech OV-11 28 Litre vacuum oven presented in Figure IV.3, from 12 to 24 hours from 180 to 200 °C.

Figure IV.3. MedlineScientific® Jeio Tech OV-11 28Litre vacuum oven.

XRD profiles of the products were acquired by irradiating X-ray to the specimens in a Warhus vacuum chamber Philips PW3830 X-ray generator (Figure IV.4 a) operating at 30 kV and 20 mA (Ni-filtered CuKα radiation, $\lambda = 0.1542$ nm). For each X-ray analysis, a specimen of 5 mm × 7 mm × 40 μm of Azo-Cel would be prepared and the two heads of the specimen would be

attached to the sides of the collimator using a double-side duct-tape, resulting in a firm attachment so that the high pressure caused by vacuum inside the chamber would not blow the fabric astray. A Fujifilm imaging plate was placed on position 2 (It's the positioning of the XRD film inside the chamber that determines whether the final profiles will be SAXS or WAXS) and the chamber was sealed with lead barrier and the sample was irradiated by X-ray for 6 h. Two-dimensional diffraction patterns recorded on the imaging plate were read offline *via* a Fujifilm BAS 1800-II bio imaging analyzer (Figure IV.4 b). The acquired circular patters were averaged radially by Gnuplot software to get diffraction profiles.

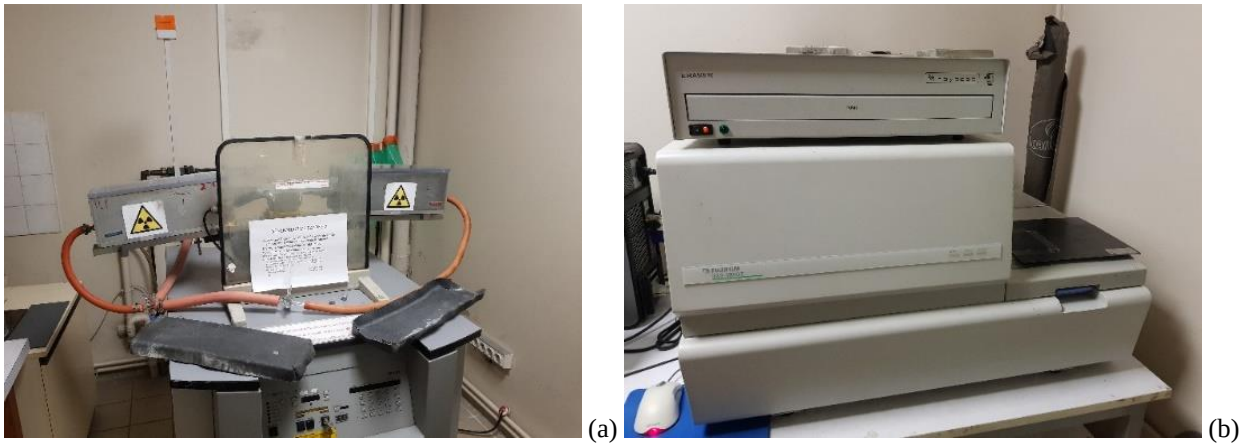

(a) (b)

Figure IV.4. a) Warhus vacuum chamber Philips PW3830 X-ray generator. b) Fujifilm BAS 1800-II bio imaging analyzer.

IV.3. Results and discussion

Previous studies revealed that alignment of electrospun fibers in a uniaxial direction improves the mechanical properties of the resulting fabrics, including the tensile strength along the principal fiber axis and the Young's modulus, compared to non-aligned fibrous fabrics.[6,7,9,134] Therefore, in this study, we employed a cylinder-shaped rotating drum electrode as a collector of the electrospun textile to fabricate an uniaxially aligned nanofibrous Azo-Cel fabric and the details

are fully discussed in the previous chapter. The obtained self-standing Azo-Cel fabric was vacuum dried and used for the following physical property analyses: ATR-FTIR, diameter determination, tensile properties, and XRD. Figure IV.5 presents ATR-FTIR spectra of the self-standing Azo-Cel fabric and the PEO textile for comparison.

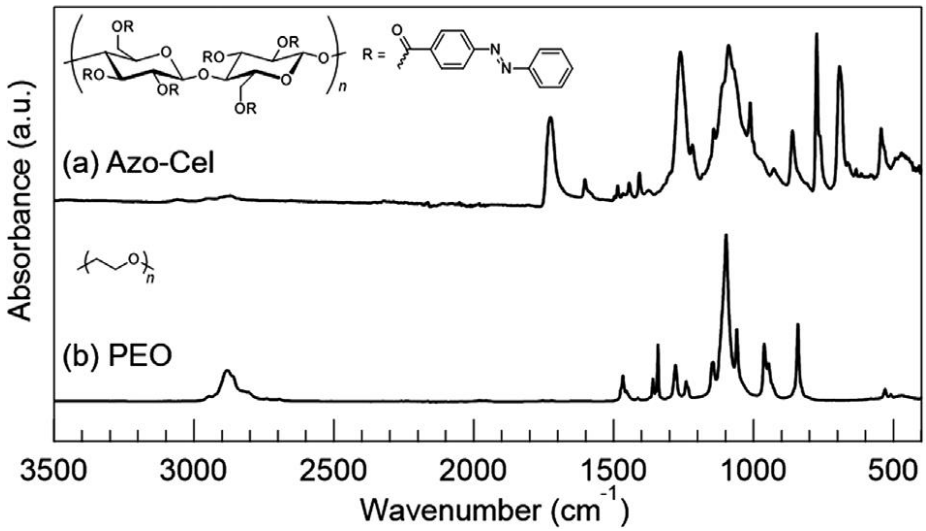

Figure IV.5. ATR-FTIR spectra of a) the self-standing Azo-Cel fabric and b) the PEO textile.

In the spectrum of the self-standing Azo-Cel fabric (Figure IV.5 a), a characteristic absorption band of the C-H stretching vibrations in the PEO backbone observed around 2880 cm^{-1} in Figure 2b disappeared, indicating a successful elimination of the PEO layer in the fabric. Secondly, Figure IV.6 shows a SEM image of the self-standing Azo-Cel fabric and a histogram of the constituent fiber diameter distribution.

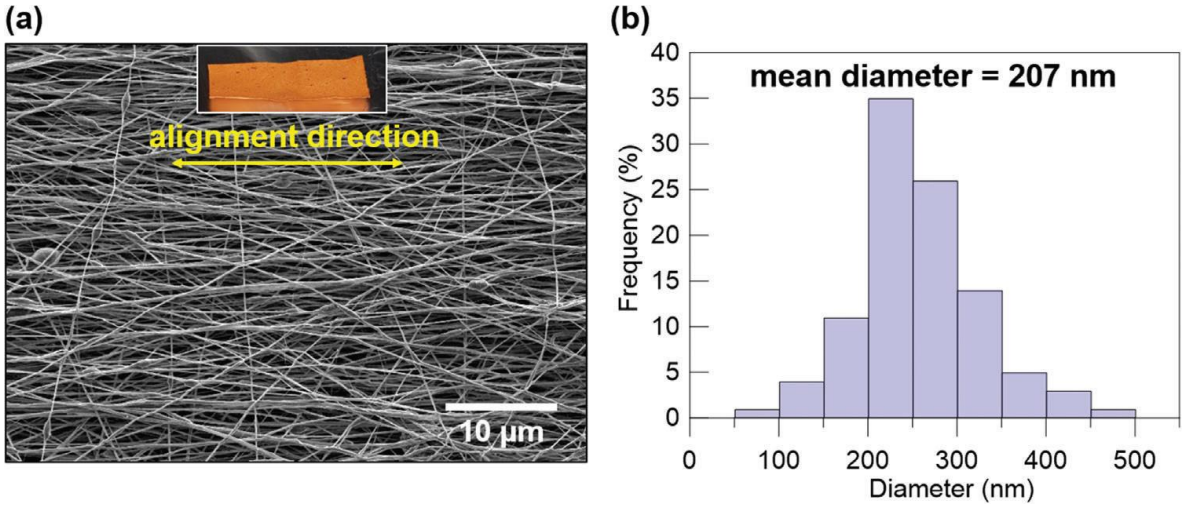

Figure IV.6. a) A SEM image of the self-standing Azo-Cel fabric (with an inserted photo) and b) a histogram of the diameter distribution of the fibers in the fabric determined from the SEM image by ImageJ open-source software.

By using a cylinder-shaped rotary electrode, formations of such spherical and spindle beads were reduced (as shown in Figure IV.6) thanks to the effect of high-speed rotation of the electrode, *i.e.*, the fibers are taken up on the rotating surface of the cylinder resulting in the alignment and stretching of the electrospun fibers [7]. As presented, the self-standing Azo-Cel fabric consisted of almost uniaxially aligned nanofibers with the mean diameter of 207 nm. Thirdly, Figure IV.7 presents stress-strain curves of the Azo Cel fabric. The stress (MPa) was calculated based on the "uncompressed" thickness (40 μm) determined by the SEM image (Figure IV.8) and the "compressed" thickness (11 μm) measured with a digital Vernier scale as detailed in the IV.2 Experimental section. If one considers that the Azo-Cel fabric maintains its thickness (uncompressed form: 40 μm) during the tensile testing, the maximum tensile strength of the fabric is calculated to be 1.2 MPa at breaking point with 0.64% tensile strain as shown in the red curve, while the maximum tensile strength can be calculated to be higher value (4.4 MPa) with the compressed thickness (11 μm) as shown in the black curve if one assumes that the fabric shrinks by reducing the voids between the nanofibers *via* stretching during the tensile testing.

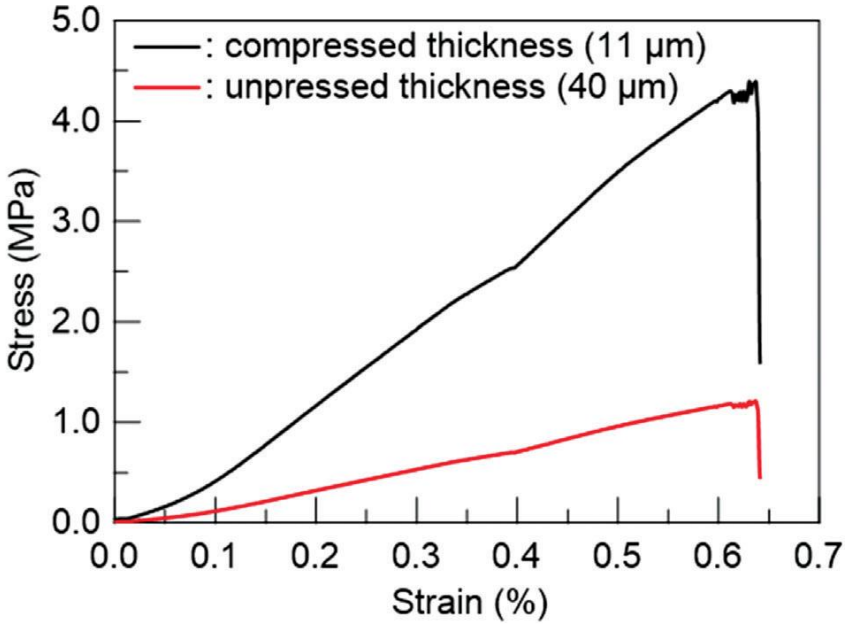

Figure IV.7. Stress-strain curves of the self-standing Azo-Cel fabric: the black and red curves respectively represent the stress (MPa) calculated based on the compressed thickness (11 µm) and the unpressed thickness (40 µm) of the fabric versus strain (%).

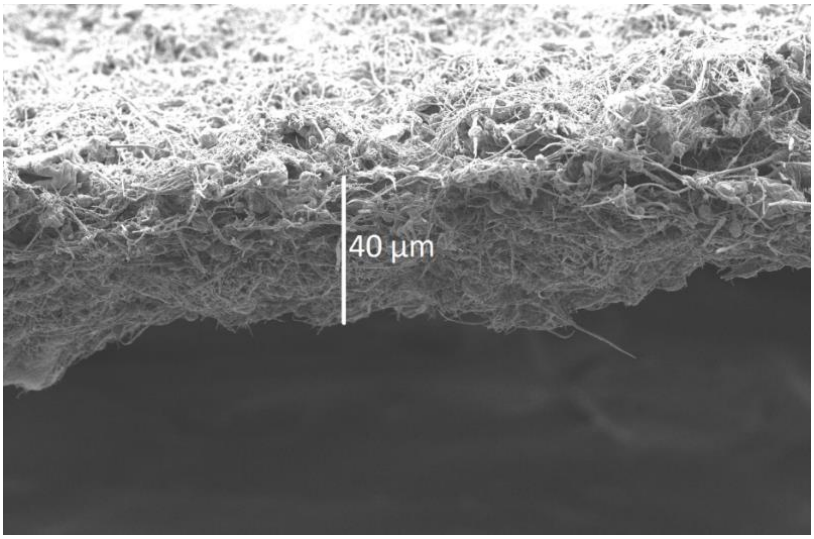

Figure IV.8. A SEM observation of the cross-section of the self-standing Azo-Cel fabric (scale bar = 40 µm).

The Azo-Cel textile exhibits a maximum Young's Modulus ($E=\delta/\varepsilon$, where E is the Young's Modulus, δ the tensile stress and ε the tensile strain values) at breakage point equal to 6.87 GPa for compressed thickness and 1.87 GPa for unpressed thickness. Although it should be noted that

the researchers in the textile field are mostly interested in the study of stress-strain behavior of the textile, especially for soft matters. On the other hand, most polysaccharides demonstrate a bi-linear behavior under tension (most possible hypothesis is the movement of macromolecular polymeric chains upon each other and a change in molecular angles), which makes the study of Young's modulus tricky. Therefore, studying the stress-strain profiles appear to be more reliable to discuss mechanical behavior of polysaccharide-based textiles [184].

It was studied that the Azo-Cel fabric improved its crystallinity by thermal annealing at 200 °C (higher temperature than the T_g of Azo-Cel: 175 °C) under vacuum for 24 hours followed by cooling down naturally at room temperature. Figure IV.9 presents the XRD patterns of as-spun and AC-200-24 products that are obtained by characterizing the two products at European Synchrotron Radiation Facility (ESRF).

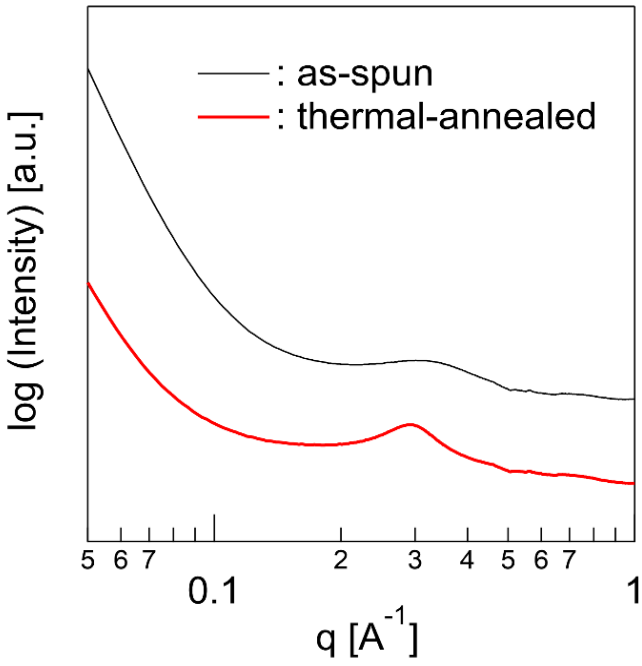

Figure IV.9. XRD patterns of as-spun and thermally annealed Azo-Cel (AC-200-24).

To further investigate the effect of thermal annealing on the crystallinity of the Azo-Cel fabrics, XRD of as-spun and thermally annealed Azo-Cel fabrics under various conditions (different temperatures and different time periods) was studied. Thermal annealing of the Azo-Cel fabric above 200 °C and for longer time than 24 hours resulted in visible degradation of the specimen, observed as a change of colour and shape. Therefore, Azo-Cel specimens were annealed at slightly over the T_g, *i.e.* 180 °C, and 200 °C, for 12 and 24 hours, making 4 annealed specimens overall. The samples were labelled as follows: as-spun, AC-180-12, AC-180-24, AC-200-12, AC-200-24. The first three digits indicate the temperature of annealing, and the last two digits stand for the time period under which the specimen was annealed.

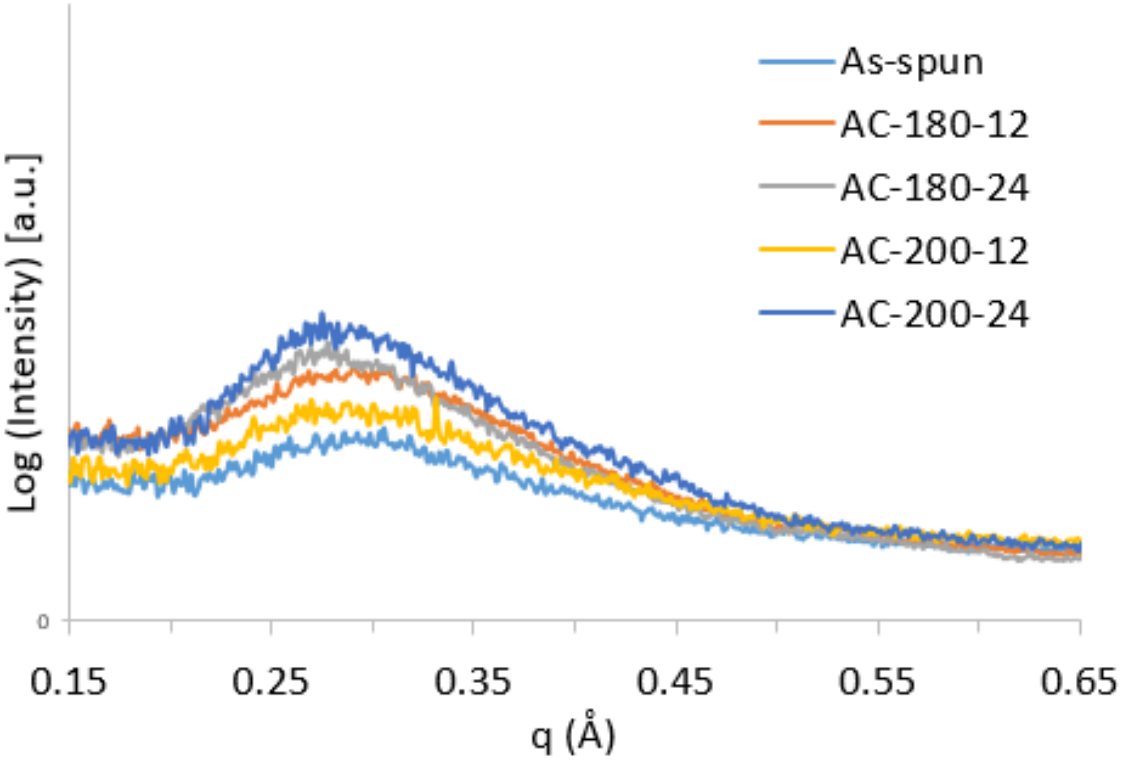

Figure IV.10. XRD profiles of as-spun and thermally annealed Azo-Cel specimens.

Figure IV.9 presents the XRD profiles of the 5 specimens. At both 180 and 200 °C, the specimens annealed for longer time (24 hours) show clearer diffraction peaks around $2\theta = 18°$ comparing to those annealed for shorter time (12 hours), indicating that the Azo-Cel improves its crystallinity in proportion to the annealing time at these temperatures. However, extending the annealing time more than 24 hours did not change the XRD patterns. Thus far, thermally annealing the Azo-Cel fabric at 180 and 200 °C for 24 h proved to be the best options to improve the crystallinity. The XRD profiles illustrated in Figure IV.10 are results of short time of irradiation (1 hour). Increasing the irradiation time would solve the problem and homogenize the profiles.

It is primordial to note that the sample AC-200-24 was more brittle than AC-180-24 probably due to slight thermal degradation of the polymer that could not be visually observed. Therefore, AC-180-24 was used as the thermally annealed Azo-Cel sample for the UV-induced photo-actuation analysis described in the next two sections.

IV.4. Conclusion

The obtained self-standing Azo-Cel textile was characterized by ATR-FTIR after removal of PEO layer and vacuum drying. It's been shown through the IR spectra that the PEO was completely removed and no residues were found on the product. The Azo-Cel textile has a mean dimeter of 207 nm, estimated by statistical analysis using ImageJ software. The tensile properties of Azo-Cel showed a maximum stress of 4.4 MPa for an uncompressed Azo-Cel textile (Thickness = 40 μm) and 1.2 MPa for a compressed Azo-Cel textile (Thickness = 11 μm). This is because the Azo-Cel textile is considered to be a porous nanofibrous material, therefore the real thickness is in an uncompressed state. However, if we remove these pores and consequently decrease the

thickness, according to the tensile strength formula (described in the experimental section), a higher tensile resistance may be achieved.

At last, the XRD profiles of as-spun and four different thermally annealed products were studied and it was found that increasing the temperature and time of annealing may increase the crystallinity. However, this can affect the flexibility of the Azo-Cel membrane and render it more rigid. Therefore it was found that annealing the Azo-Cel textile at 180 °C for 24 hours may be the suitable candidate for further investigations.

Chapter V : Photo-responsivity Properties of Azo-Cel Textile

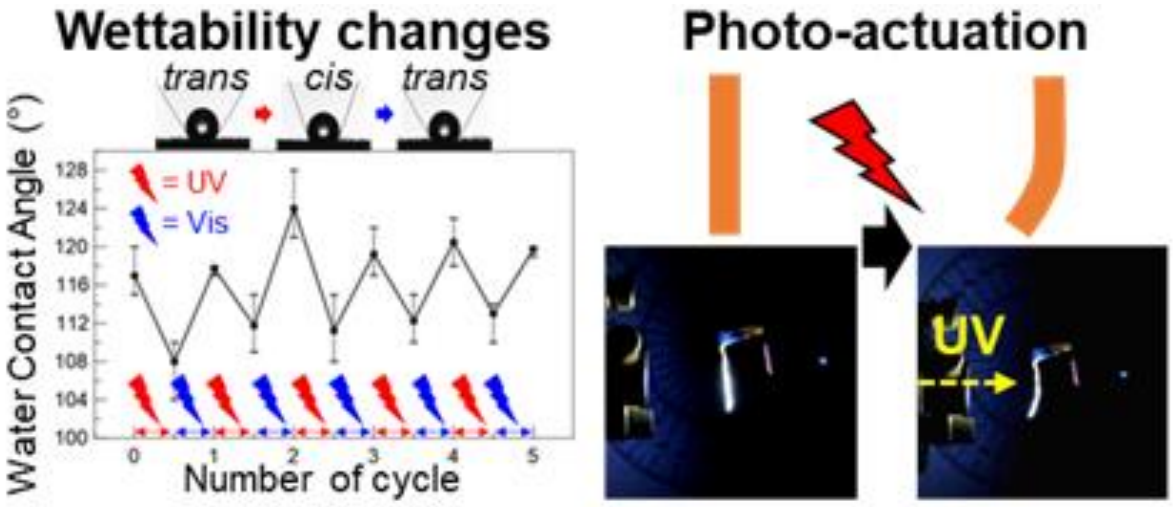

V.1. Introduction

AB polymers belong to a category of photo-deformable smart functional polymers. They are able to produce photo-actuators; the sort of material that convert light energy into mechanical movement [135–140]. AB units can undergo *trans*-to-*cis* photo-isomerization once irradiated by UV light, and *cis*-to-*trans* photo-isomerization when irradiated by visible light. Specifically, the photo-isomerization of an azo compound from the linear *trans* form to the bent *cis*-form can prompt its large size (or length) adjustment from 0.9 to 0.55 nm, which can cause significant changes in the arrangement order of azo mesogens and the conformation of their encompassing polymer chains, consequently leading to the creation of microscopic force within azo polymers and their photomechanical impacts. AB-contained materials exhibit a variety of macroscopic photo-responsive behavior once irradiated by proper light. These behaviors include twisting, bending, oscillation, rotation, and contraction. They also demonstrate significant promise in a variety of actuation applications, including soft robotics and artificial muscles [90,141,142]. Recently, photo-actuation of non-liquid-crystalline polymers containing AB under specific conditions has been also reported [143–145]. Although these AB-containing polymers possess great photo-deformable effects in the form of their cross-linked or networked gels or films, there are some fundamental drawbacks for practical applications such as artificial muscles in soft robotics because of their weak mechanical strength and thermal resistance. Therefore, designing polymeric photo actuators in other forms than gels or films is of great importance. Our approach to tackle this challenging task is the electrospinning of a photo-responsive cellulose 4-phenyl azobenzoate (Azo-Cel) to form robust and flexible photo-responsive fabrics.

V.2. Experimental

The WCA of Azo-Cel fabrics was measured using an I.T. Concept "Tracker" Tensiometer at room temperature, illustrated in Figure V.1 a. Following procedure describes the general pathway of each measurement: a 5 μL of deionized water was dropped on a piece of the fabric that is already fixed on a glass slide using a double-sided tape. The contact angle was measured when the angle became stable after 90 s. The water droplet was wiped out from the specimen with a piece of tissue paper (Kimberly Clark "Kimwipes") after each measurement. Then, the specimen was irradiated with UV light (λ = 355–375 nm) *via* a SPOT UV Hamamatsu LC8 L9588 Hg-Xe lamp equipped with an A9616-07 filter at a light intensity of 60 mW/cm^2 for 15 min in a darkened room, illustrated in Figure V.1 b. The WCA was measured after the UV irradiation in the same manner as described above in a darkened room. The water droplet was then wiped out, and a white fluorescent room light was turned on and the specimen was left for 30 min under visible light before measuring the WCA again. The above-mentioned process was repeated over 5 cycles for 4 different pieces of Azo-Cel fabrics.

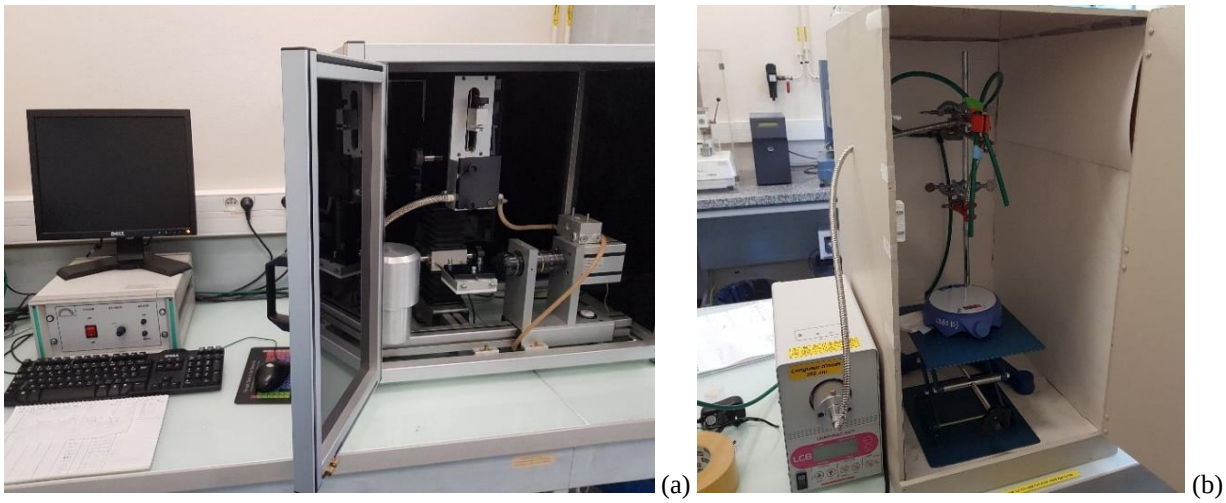
(a) (b)

Figure V.1. a) I.T. Concept "Tracker" Tensiometer. b) SPOT UV Hamamatsu LC8 L9588 Hg-Xe lamp.

For each WCA experiment, either on Azo-Cel derivative fabrics or on CA fabrics, a 4 × 20 mm^2 fabric would be prepared in a way that the long side of the rectangle would be parallel to the principal axis of the aligned fibers. The fabric would be anchored with tweezers and placed at three different distances away from the UV light (λ = 280–400 nm) source (Ushio UXM-200H, Hg/Xe 200W lamp equipped with a LOT-ORIEL 66216 dichroic mirror and a 59060 IR blocking filter), *i.e.*, at 1, 2, and 4 cm, leading to different surface light intensities of 60, 45, and 25 mW/cm^2, respectively. Figure V.2 illustrates the UV irradiation setup.

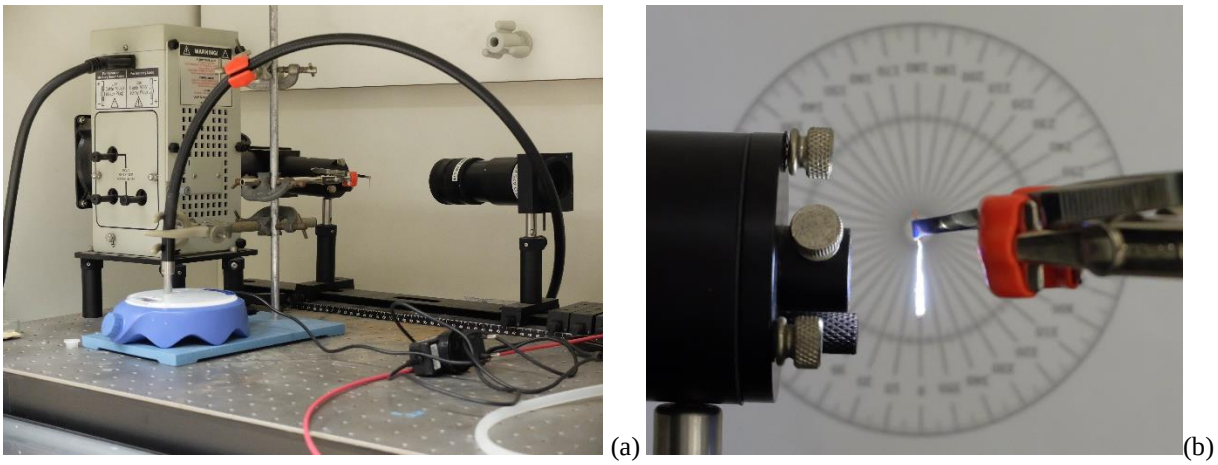
(a) (b)

Figure V.2. a) Ushio UXM-200H, Hg/Xe 200W lamp. b) An example of a self-standing Azo-Cel fabric just at the start of the irradiation process, placed 1 cm away from the UV light.

Azo-Cel, and CA fabrics were irradiated by UV light in a dark room for 30 min and the whole process was monitored using a Fujifilm X30 digital camera. The UV-induced photo-actuation behavior (angular movement) of the fabrics was characterized by measuring the difference between the angle of the UV-irradiated fabrics at the end of 30 min, and the initial angle of the non-irradiated fabrics using a printed protractor sheet placed behind the specimens, illustrated in Figure V.2 b.

V.3. Results and discussion

Under light irradiation, photo-responsive materials can change their molecular geometric structures, which is frequently accompanied by variations of molecular polarity and surface free energy, leading to an induced transition of surface wettability [146]. In the case of AB-functionalized materials, photo-isomerization of the AB moiety between its *trans* and *cis* isomers causes a change in dipole moment, resulting in a change of surface wettability. The *trans* isomer with a smaller dipole moment has a lower surface free energy, and the *cis* isomer with a larger dipole moment has a higher surface free energy [147,148]. Therefore, the materials having the *trans* isomer generally show greater Water Contact Angle (WCA) than those having the *cis* isomer [149,150]. A similar phenomenon was observed for the Azo-Cel fabric. One notes that the photo-isomerization of the AB moiety in Azo-Cel from the *trans* to the *cis* isomers under UV irradiation and vice versa under visible light irradiation in the solution state was reported by Otsuka and Barrett [19]. A WCA of an Azo-Cel fabric was first measured as it was obtained (a picture of a water droplet on the as-spun Azo-Cel fabric is shown in Figure V.3 a), then the same Azo-Cel fabric was irradiated with UV for 15 min followed by its WCA measurement (Figure V.3 b). The specimen was left for 30 min under visible light before measuring its WCA again (Figure V.3 c). The above-mentioned procedure was repeated for 5 cycles and variation of the WCA was plotted in Figure V.3 d, where the WCA values are the mean values of 4 sets of the measurements using different pieces of Azo-Cel fabric, and the error bars represent their maximum and minimum values. It should be noted that the small hysteresis and range of the WCA values are probably due to rough surfaces of the Azo-Cel fabric because the surface nano/microstructure is one of the important factors of the surface wettability.

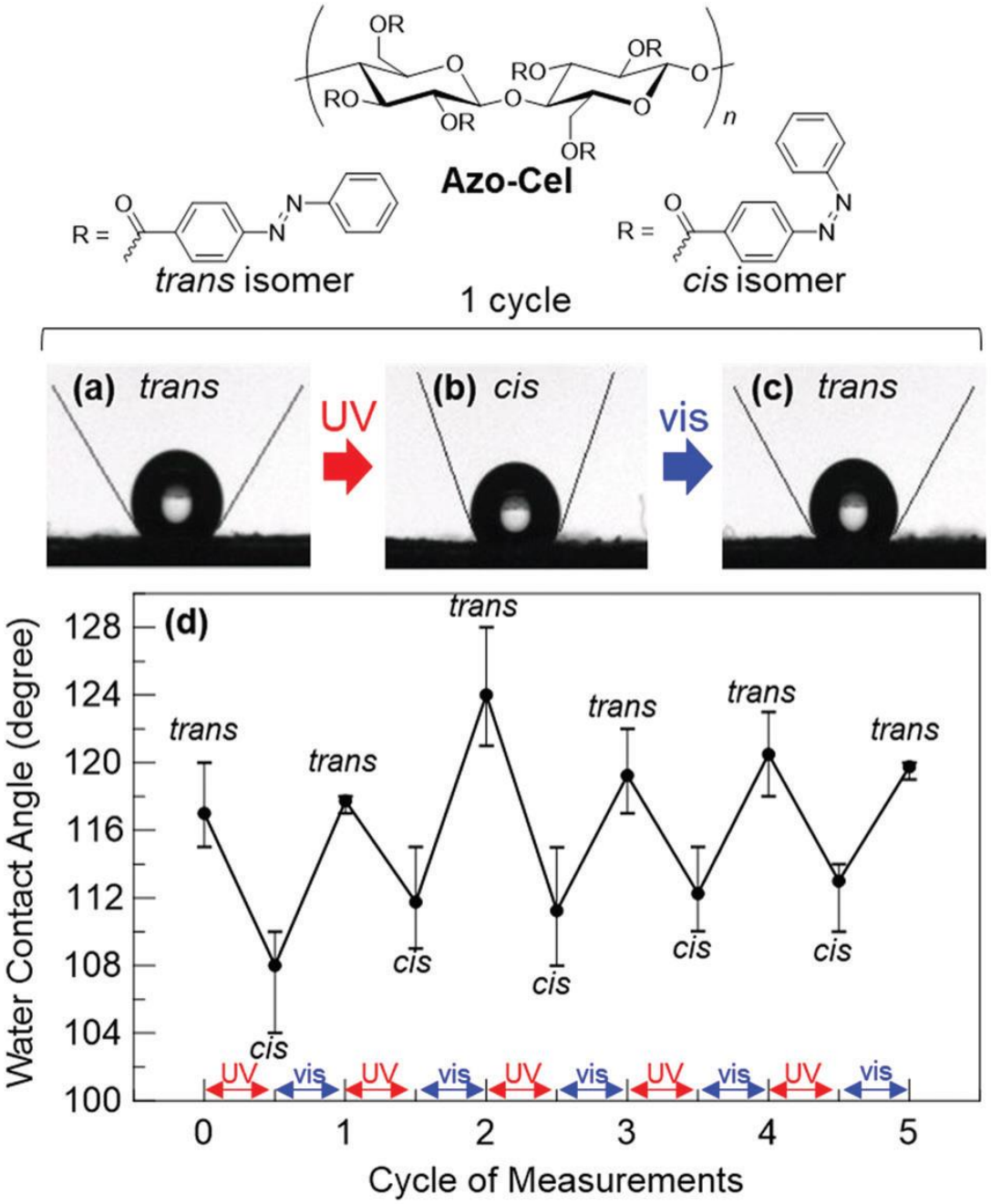

Figure V.3. Photos of water droplets on a) an as-spun Azo-Cel fabric (*trans* isomer): WCA = 120°, b) the same fabric after UV radiation (*cis* isomer): WCA = 108°, and c) the same fabric after visible light irradiation (*trans* isomer): WCA = 118°. d) The WCA changes of the Azo-Cel fabric over 5 cycles of UV/visible light irradiations. The plotted WCA values are the mean values of 4 sets of the measurements using 4 different pieces of the Azo-Cel fabric, and the error bars represent their maximum and minimum values.

As presented in the Figure V.3 d, the WCA was reversibly changed by the UV and visible light irradiations (averaged angle change was 8.7°), indicating that the photo-isomerization of the AB moiety in the Azo-Cel fabric induced the changes of its surface wettability. Many of the AB-functionalized materials that have been reported have the potential to convert photo-stimuli into mechanical deformations, in other words, a photo-actuation property [26]. Among them, a pioneering work of UV-driven azomaterial bending toward the light source was reported by Ikeda et al. on AB-functionalized LCP films [27]. The key of this asymmetric bending deformation of the film was that the photo-isomerization from the rod-like *trans* isomer to the bent-shape *cis* isomer of the AB moiety occurred only in the surface region of the film facing the UV light source, but not in the bulk of the film because most of the incident photons are absorbed near the surface, within a thickness of less than 1 μm due to the large molar extinction coefficient of the AB moiety (2.6×10^4 L mol^{-1} cm^{-1}). The resulting gradient distributions of the bent-shape *cis* isomers in the thickness direction of the film led to a stress gradient, which induced the bending of the film toward the light source.

Figure V.4 shows the stability of the water droplet after its exposure to the surface of the self-standing Azo-Cel textile. It is clear that after 90 seconds, the WCA is stable and the product shows a good fatigue towards the water droplet.

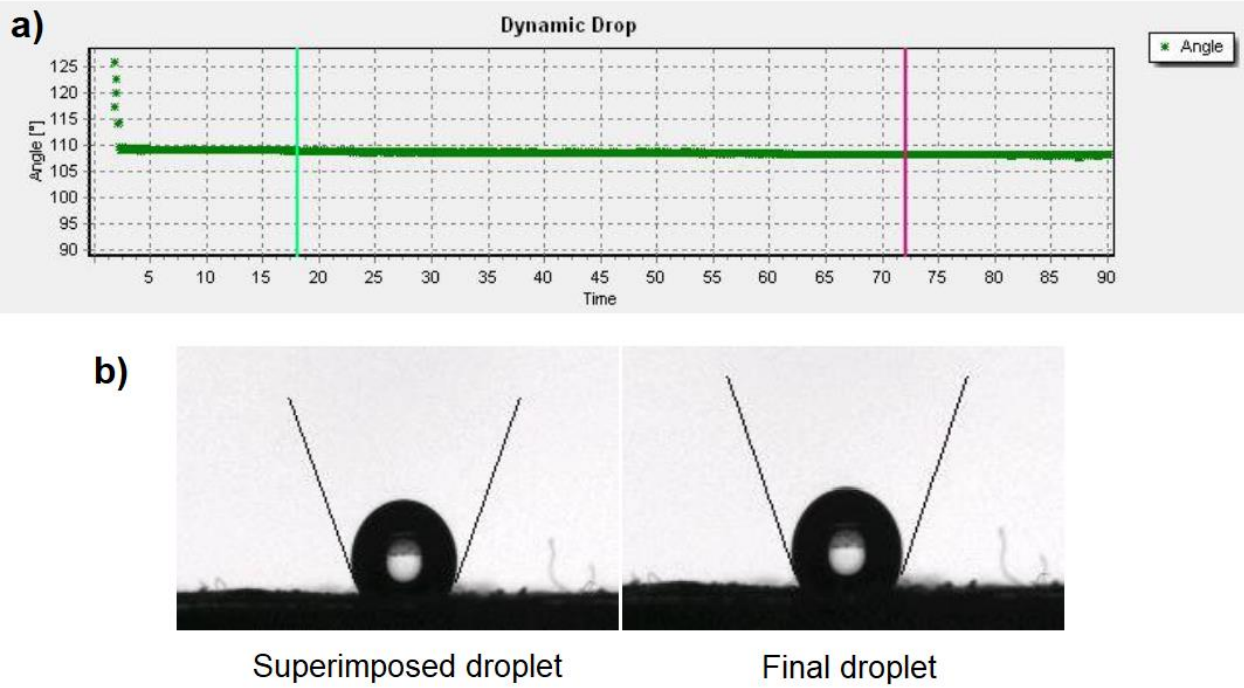

Figure V.4. An overall scheme of the WCA of water droplet over 90 s after being in contact with the surface of self-standing Azo-Cel textile. a) The plot of WCA vs time of the water droplet, b) Superimposed droplet vs final droplet. Estimated WCA is at 108°.

We here observed a similar UV-driven asymmetric bending deformation of the Azo-Cel fabric toward the light source (Figure V.5). Figure V.5 b shows a series of photographs of a piece of the Azo-Cel fabric placed 2 cm away from the UV light source (at the left-side in the photos) over the time of irradiation with light intensity = 45 mW/cm^2. As presented in the Figure, the Azo-Cel fabric clearly bent toward the UV light source over time, and the bending angle from the initial state became about 15° after a 30 min irradiation. As a control experiment, an electrospun fabric made of CA, which consists of the same cellulosic backbone as Azo-Cel yet a non-photo-responsive acetyl group as the pendant group, was irradiated by UV under the same conditions (Figure V.5 d). In stark contrast to the Azo-Cel fabric, the CA fabric did not bend at all under the UV irradiation, suggesting that the bending deformation of the Azo-Cel fabric was induced by the

photo-isomerization of the AB moiety in the Azo-Cel. One notes that co-electrospinning of CA with free AB did not produce homogeneous fibrous fabrics because the CA and the AB molecules were phase separated during the spinning process and formed huge aggregates of AB in the CA fabric as shown in Figure V.6. Therefore, chemical modification of cellulose with AB groups is confirmed essential to electrospin such a photo-responsive cellulosic fabric.

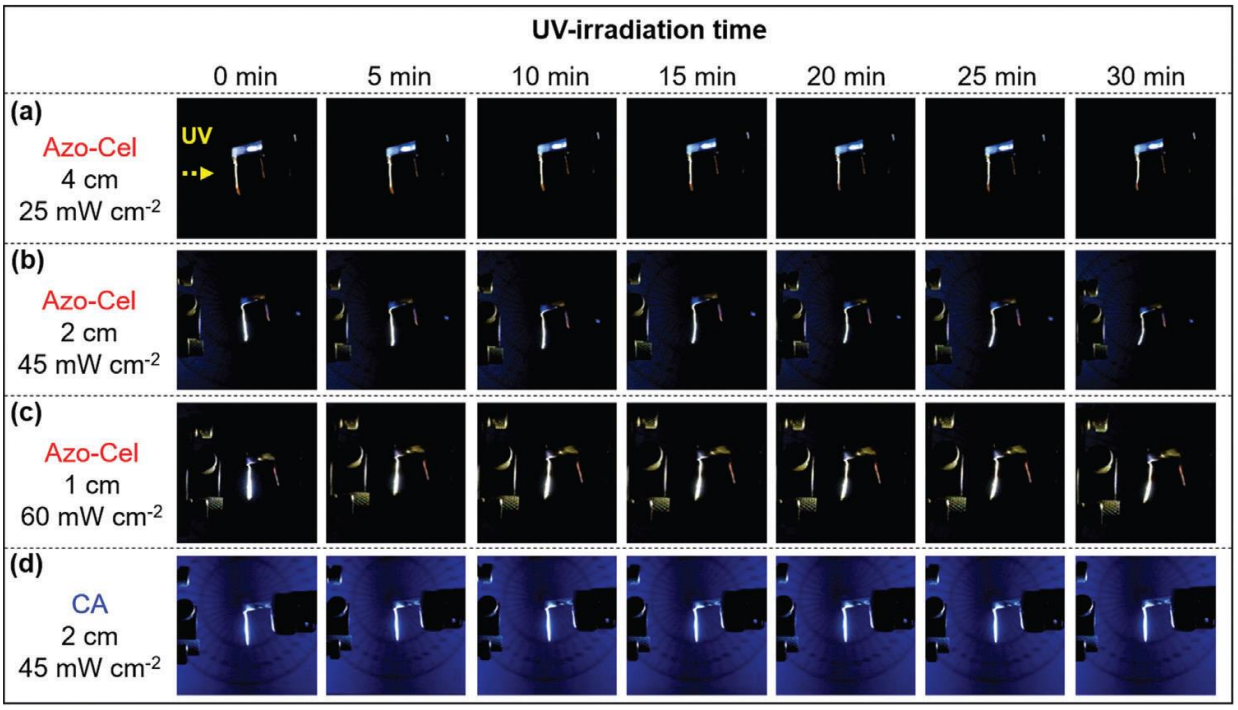

Figure V.5. Series of pictures of Azo-Cel and CA fabrics irradiated by UV over time of the irradiation: a) Azo-Cel placed at 4 cm away (the light intensity = 25 mW/cm^2), b) Azo-Cel placed at 2 cm away (45 mW/cm^2), c) Azo-Cel placed at 1 cm away (60 mW/cm^2), and d) CA placed at 2 cm away (45 mW/cm^2) from the UV light source (at the left-side in the pictures).

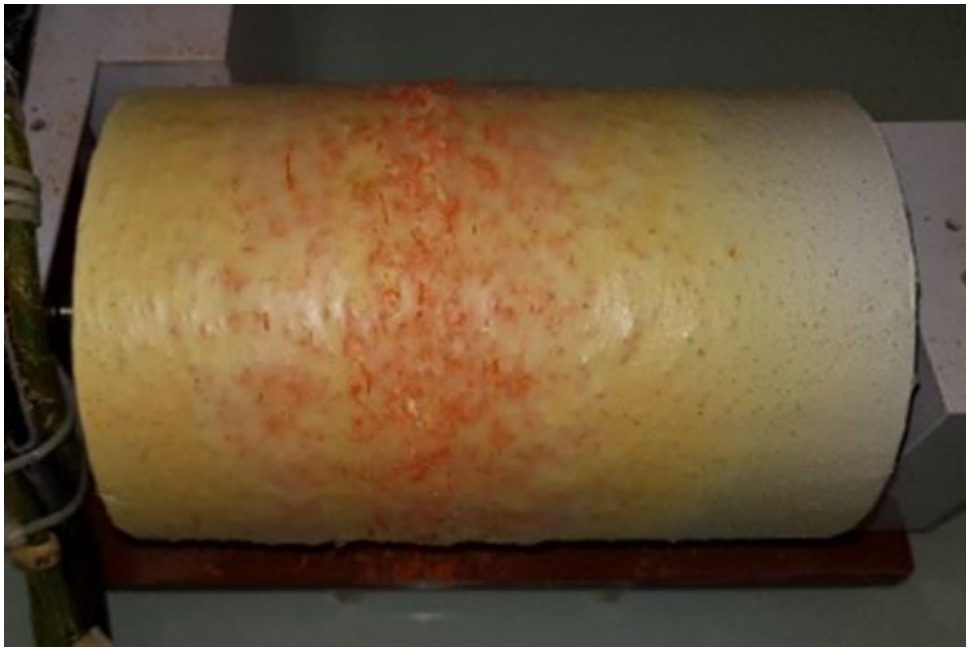

Figure V.6. A picture of the co-electrospun product from the mixture of CA and AB (molar ratio: glucose unit of CA/AB = 1/3) in acetone/DMAc = 2/1 (v/v) (concentration of CA: 17 wt%) collected on the cylinder-shaped drum electrode.

UV irradiation of the Azo-Cel fabric from longer and shorter distances also supports the UV-driven bending mechanism. Figure V.5 a and d respectively present bending behaviors over time of 2 pieces of the Azo Cel fabric placed at 4 cm (25 mW/cm^2) and 1 cm (60 mW/cm^2) away from the light source. As can be seen in Figure 5a, the UV irradiation from a longer distance (4 cm) barely bent the Azo-Cel fabric, and the bending angle after 30 min irradiation was not clearly detected, while that observed at a medium distance (2 cm) shown in Figure V.5 b was evident. This can be explained by the lower light intensity (25 mW/cm^2) from the longer distance not being sufficient to photo-isomerize the AB moiety in the surface region of the Azo-Cel fabric from the *trans* to the *cis* isomers, which must be the driving force of the asymmetric bending. On the other hand, the UV irradiation from a shorter distance (1 cm) clearly induced an asymmetric bending of the Azo-Cel fabric toward the light source, while the bending angle (≈ 10°) was smaller than that

observed in the Azo-Cel fabric irradiated from the medium distance (≈ 15°) shown in Figure V.5 b. Such a decrease of the bending angle (-5°) was possibly due to deeper penetration of photons from the shorter distance (1 cm) with higher light intensity (60 mW/cm^2) compared to those from the medium distance (2 cm) with medium light intensity (45 mW/cm^2), which decreases the gradient distributions of the *cis* isomers in the thickness direction of the fabric, and thereby leads to the less asymmetric deformation (*i.e.*, smaller bending angle). Such intermediate irradiation optimization conditions have been observed previously for azo-photomechanical materials [25], balancing higher driving input power, with confinement to the near-surface region only.

V.4. Conclusion

The self-standing Azo-Cel fabric clearly demonstrated strong photo-actuation behavior at optimal irradiation conditions. Azo-Cel demonstrates photo-responsive WCA changes upon UV and visible light irradiations thanks to the presence of Azo side groups. It also exhibits photo-responsive movements toward UV light. To put this novel polysaccharidic photo-actuator to practical use, for instance as an artificial muscle, photo-deformable performance parameters such as stimuli-response speed, and deformation extent, still must be improved. Previous studies on AB-functionalized materials have shown that regularly aligned AB units can cooperatively amplify nanoscopic geometric variations of an individual AB molecule into macroscopic deformations. Therefore, further studies on structural ordering of AB moieties in Azo-Cel by regioselective functionalization of cellulose and thermal annealing of the fabric are under investigation with a view to optimize crystallinity of the Azo-Cel fabric to obtain better photo-deformable performance and mechanical properties.

Chapter VI : Regioselective Functionalization of di-Azo-Cel

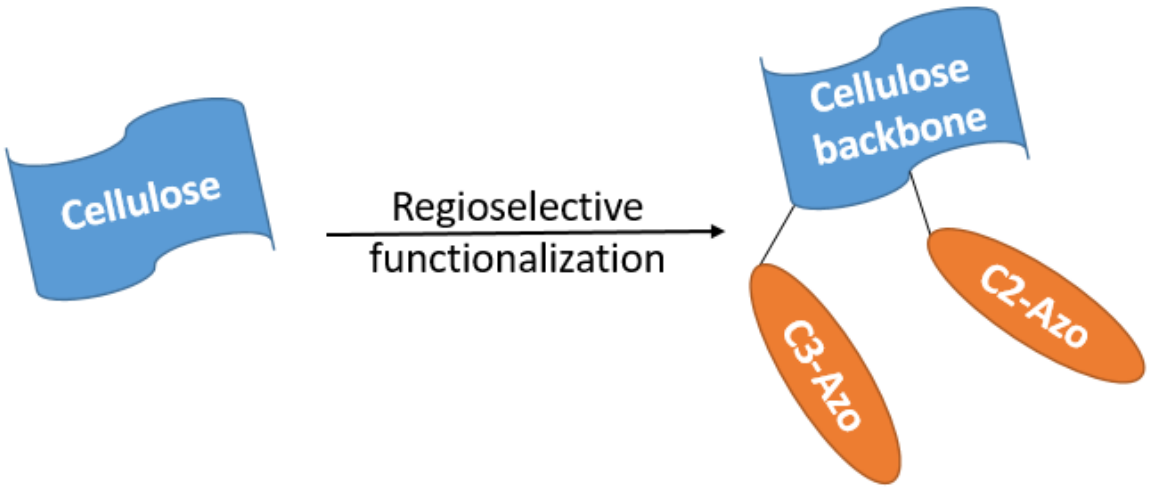

VI.1. Introduction

Physical properties of cellulose and its derivatives, such as crystallinity and the solubility, are greatly influenced by their intra-/intermolecular interactions, *e.g.* hydrogen bonding, ionic bonding, and π–π stacking, between their pendant groups [109]. Regioselective substitution of the hydroxyl groups of cellulose with Azo group is thus investigated in order to study the effect of these intra-/intermolecular interactions on the physical properties of Azo-Cel that must be one of the key aspects affecting the photoresponsivity of the fabrics. As a first attempt, the primary hydroxyl group of the carbon-6 (C6) of the AGU is selectively protected with triphenylmethyl group (or so-called trityl group) [151] that will be deprotected after regioselective substitutions of the secondary hydroxyl groups of C2 and C3 with Azo group.

The dissolution of cellulose in DMAc/LiCl [152], and most importantly its tritylation in DMAc/LiCl/pyridine has been the focus of researchers [153,154] before the discovery of ionic liquids (ILs). However, it has been proven that the synthesis of cellulose derivatives in ILs as reaction media would be more effective than DMAc/LiCl [155]. ILs are basically molten organic salts having low melting points. Early ILs were based on alkylpyridinium cations [156], but they demonstrated facile reduction. Consequently, more durable salts have been introduced based on 1-alkyl-3-methylimidazolium [157]. In 2002, Swatloski and colleagues reported the dissolution of cellulose with ILs and its applications [158]. They state that ILs can be utilized as non-derivatizing solvents for cellulose. In contrast, ILs containing 'non-coordinating' anions, such as $[BF_4]^-$ and $[PF_6]^-$, were considered non-solvents, whereas ILs including anions that are strong hydrogen bond acceptors were most successful, especially when microwave heating was incorporated. The most efficient solvents are ILs that contain chlorides, where cellulose is likely to be dissolved by hydrogen

bonding between hydroxyl groups and the anions. Scheme VI.1 presents some examples of ILs based on imidazolium, pyridinium, and ammonium salts.

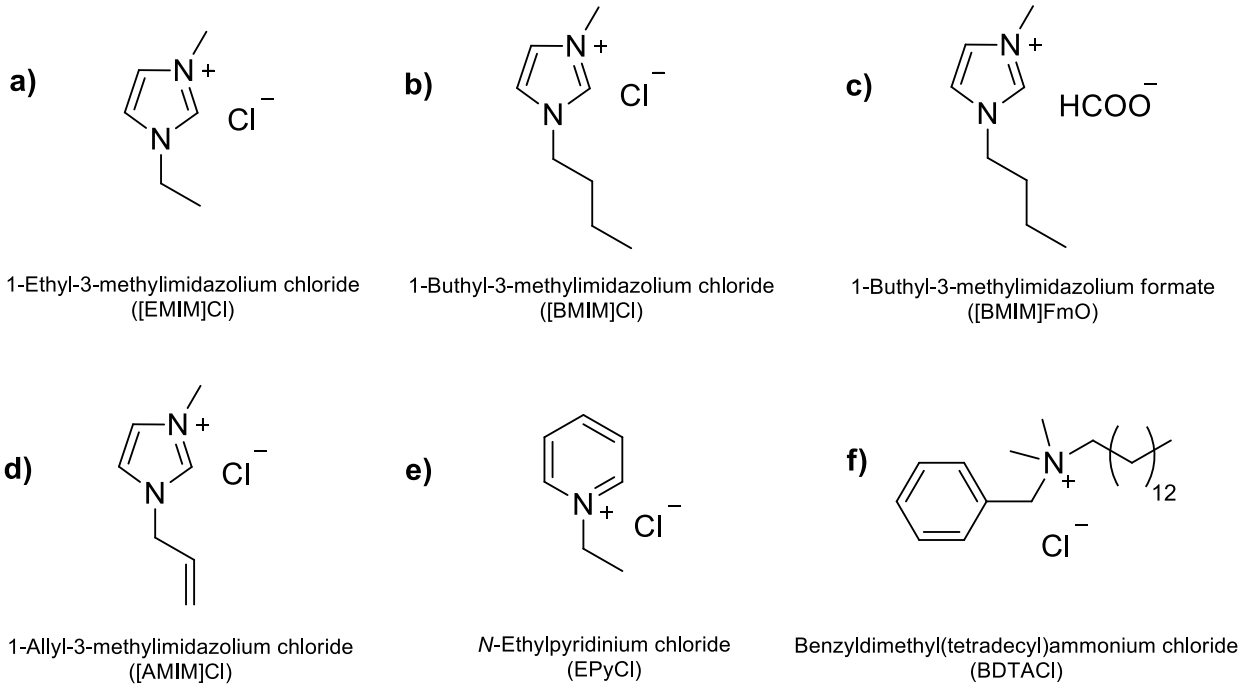

Scheme VI.1. ILs based on imidazolium, pyridinium, and ammonium salts. a-d) Imidazolium salts, e) pyridinium salt, f) Ammonium salt [159].

It is interesting to note that the length of the alkyl chain directly correlates with the solubility of cellulose in 1-alkyl-3-methylimidazolium type ILs, meaning that ILs with even-numbered alkyl chains are able to dissolve the polymer more efficiently than those with odd-numbered alkyl chains [151]. The intrinsic viscosity of cellulose in ILs decreases as the temperature rises, which could be a sign of degrading solvent's thermodynamic properties [160,161]. In an experimental condition, [BMIM]Cl gave the best results out of all ILs with even-numbered alkyl chains, with up to 25 wt% dissolved cellulose by microwave heating; but it is easier to make solutions ranging 5 to 10 wt% of cellulose [158]. Hence, [BMIM]Cl was selected as the IL of choice for this study.

VI.2. Experimental

Synthesis of di-Azo-Cel

Synthesis of regioselective di-Azo-Cel is conducted in three main steps. First, primary alcohol groups (C6) of AGUs in cellulose are functionalized with trimethylphenyl radicals (trityl group) to produce regioselectively functionalized 6-*O*-trityl cellulose (6OTC). Remaining free alcohol groups of AGUs in 6OTC at C2 and C3 are then functionalized with 4-phenylazobenzoate to procure 2,3-*O*-di-Azo-6-*O*-trityl cellulose (di-Azo-monoTC). At last, C6 groups are deprotected from trityl groups to produce 2,3-*O*-di-Azo-Cel (di-Azo-Cel). Further details are discussed in below-mentioned sub-sections. To review materials' details, refer to chapter II.2 *Materials* section.

To synthesize 6OTC (Scheme VI.2), 1.0 g of dried MCC (Avicel PH-101 Serva Co. w.p) was dissolved into 10.0 g of [BMIM]Cl (9.3 mol equiv. to 1 mol AGU) at 80 °C. This process took a full day of magnetic stirring and ultrasonication. Then, 6.84 g of trityl chloride (4 mol equiv. to 1 mol AGU) was dissolved into 5 mL of anhydrous pyridine (10 mol equiv. to 1 mol AGU) at 80 °C.

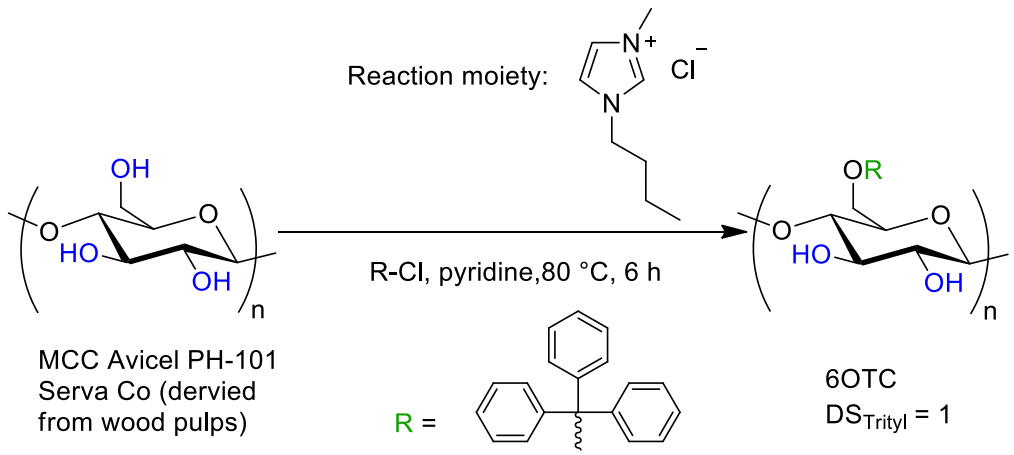

Scheme VI.2. Synthesis pathway of 6OTC.

The mixture of trityl chloride in pyridine was then poured in one portion into the melt of cellulose in [BMIM]Cl and the reaction was carried out for 6 h at 80 °C. After 6 h the reaction was stopped and the mixture was precipitated into a system of MeOH/deionized water, filtered, and washed several times with MeOH to extract pure 6OTC (Yield = 94.91 %).

To synthesis di-Azo-monoTC, 1.0 g of 6OTC was firstly dissolved into 100 mL of anhydrous pyridine. 1.4 g of Azo dye (2.2 mol equiv. per 1 mol AGU) was dissolved in 100 mL of anhydrous pyridine and then was poured in one portion to the mixture of 6OTC in pyridine. The reaction (Scheme VI.3) was carried out for 48 h at 100 °C, after which the mixture was precipitated in an excess amount of ethanol and filtered. The product was placed inside a Soxhlet extractor to be purified by continuous reflux with acetone at 70 °C for 24 h in order to remove the residual unreacted Azo dye. Afterwards, the product was vacuum dried overnight at 70 °C to yield di-Azo-monoTC as an orange-colored solid powder. Yield = 77.22 %

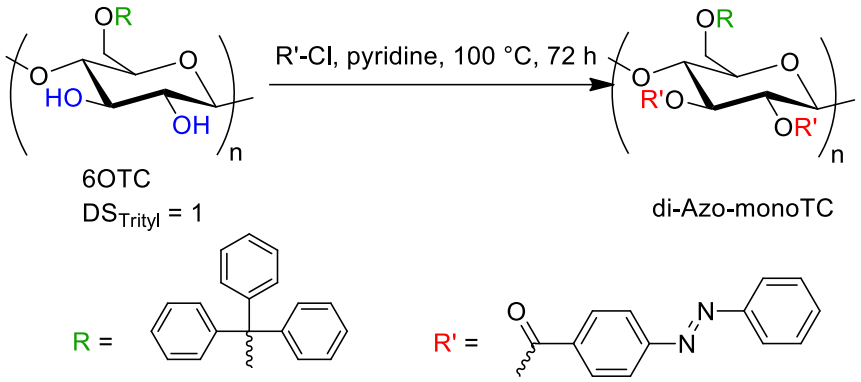

Scheme VI.3. Synthesis pathway of di-Azo-monoTC.

To obtain di-Azo-Cel, 2.0 g of dry di-Azo-monoTC was dissolved into 50 mL of THF at 60 °C. Once the product was fully dissolved, then 6 mL of concentrated HCl (37 %) was added to the mixture and the detritylation reaction was carried out for 72 h at 60 °C, after which the mixture was precipitated in acetone and filtered. The product was purified by soxhlet extractor with acetone

at 70 °C for 24 h and then vacuum dried at 70 °C for 24 h to yield 84 % of an orange-colored solid powder (considering a theoretical mass of 1.41 g for 100 % yield di-Azo-Cel). Scheme VI.4 illustrates the synthesis path to obtain di-Azo-Cel from di-Azo-monoTC.

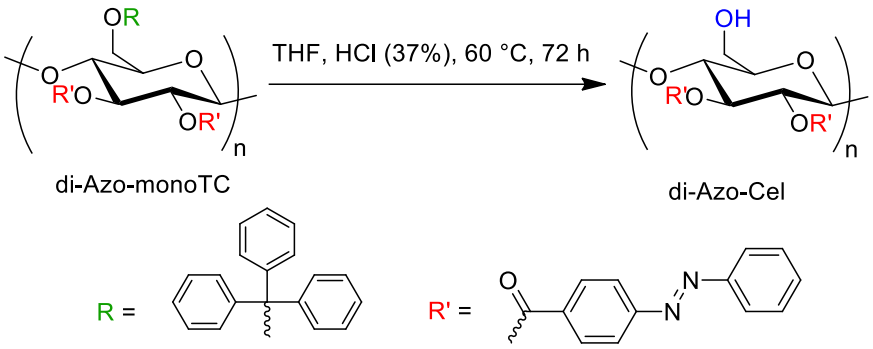

Scheme VI.4. Synthesis pathway of di-Azo-Cel.

Elemental Analysis

Elemental Analysis (EA) of di-Azo-monoTC and di-Azo-Cel products was performed at Spectropole center of chemical analysis at Aix-Marseille University. The applied method is called CHNS, during which the amounts of carbon (C), hydrogen (H), nitrogen (N), and sulfur (S) are determined in a sample. The products were analyzed by a Flash EA 1112 series Thermo Finnigan instrument and the results are obtained *via* Eager Xperience software. During each experiment, the temperature is set to 970 °C and helium gas is injected to the system at 140 mL/min. Afterward, the chromatographic column of the instrument converts the compound and elutes it in the form of CO_2, H_2O, NO_2, and SO2, which are then detected with the aid of Thermal Conductivity Detector (Katharometer).

Electrospinning of di-Azo-Cel

10 mL of a PEO solution (4.5 wt% in deionized water) was first electrospun using a 20 GA needle (inner diameter = 0.61 mm) under a 20 kV electric field at a 16.7 µL/min solution feed rate

on a rotating drum electrode covered with Al foil. Then, 10 mL of a di-Azo-Cel solution (10 wt% in DCM/DMF = 3/1 (v/v)) was electrospun on the same Al foil coated with the PEO textile using a 20 GA needle under 25 kV at 10 μL/min solution feed rate. Electrospinning was carried out at room temperature (ca. 25 °C) and ca. 30% humidity. The electrospun products were collected on two different types of metallic electrodes placed 15 cm below, namely a flat plate (20 cm × 20 cm) and a cylinder-shaped rotating drum (diameter: 10 cm; length: 15 cm) covered with Al foil.

VI.3. Results and Discussion

Characterization of di-Azo-Cel

6OTC has been characterized by ATR-FTIR spectroscopy method and its spectrum is compared to that of MCC, as presented in Figure VI.1.

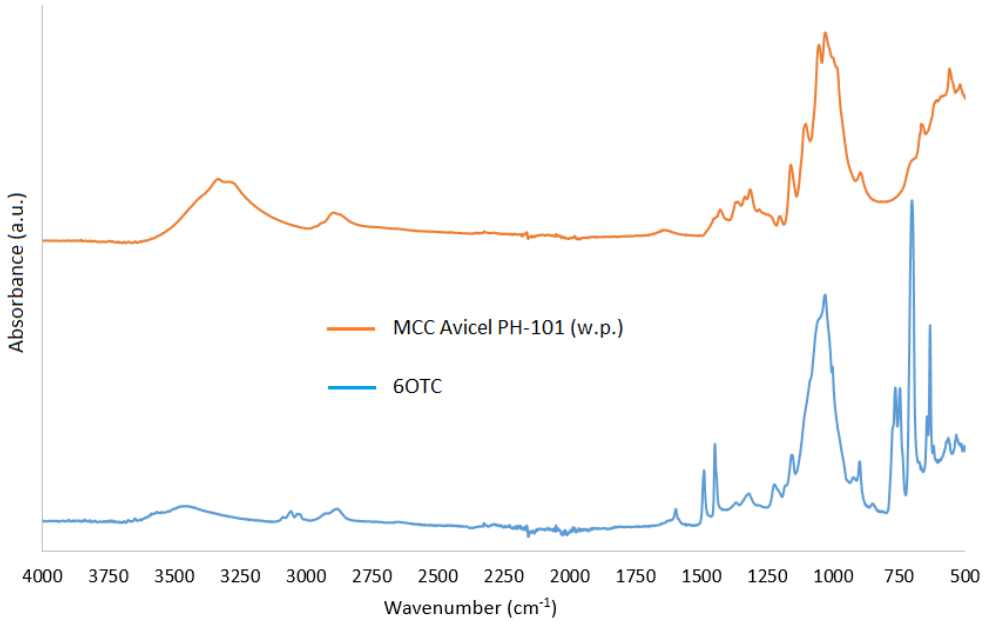

Figure VI.1. ATR-FTIR spectra of 6OTC (blue) and MCC Avicel PH-101 w.p. (orange).

The trityl side groups are manifested between 600 and 770 cm^{-1} and at 3100 cm^{-1} as well as the –OH stretching band at around 3450 cm^{-1}. The reason behind the massive difference in the

intensity of –OH stretching bands between cellulose and 6OTC is that in cellulose, the C6 is freer and more available due to reduced stereo-hindrance in that region, compared to C2 and C6. Once this region is functionalized, this intensity fades away [109].

6OTC is soluble in DMSO and THF. Respective solution of 6OTC in DMSO-d_6 were prepared according to the same procedure described in chapter II.3 and characterized through NMR platform at CERMAV-CNRS at 80 °C. Figure VI.2 presents both ^{1}H and ^{13}C NMR spectra of 6OTC.

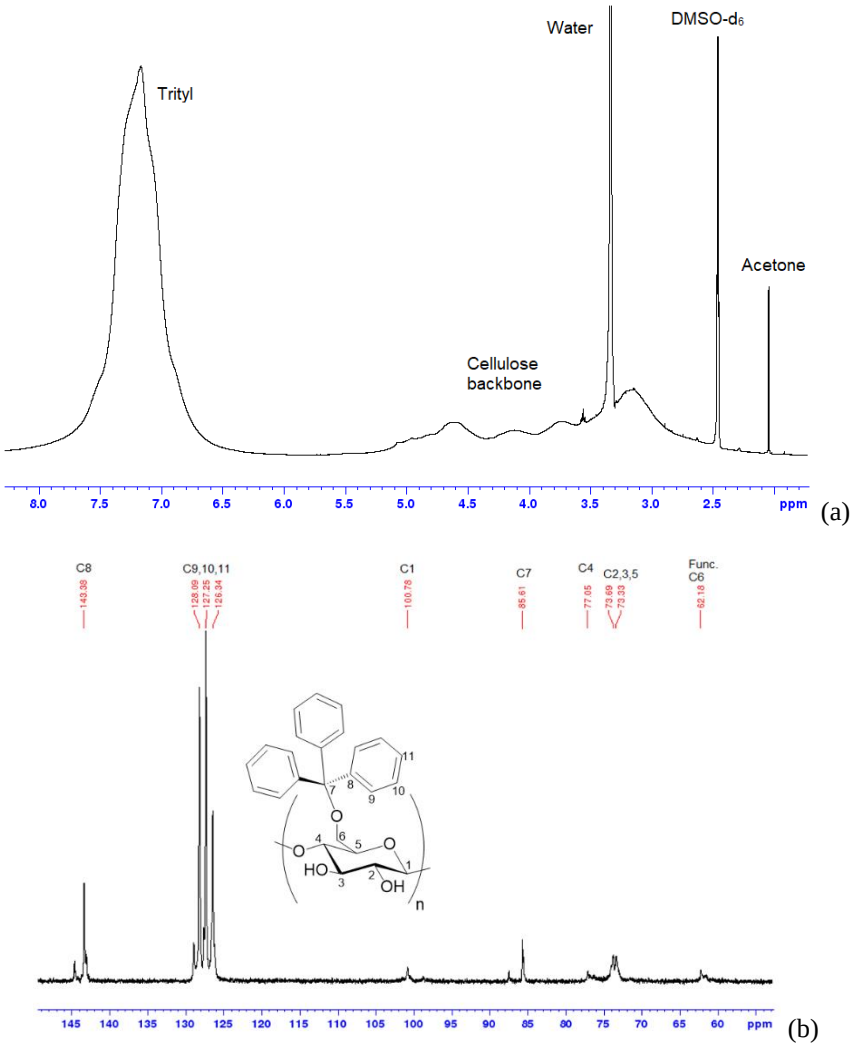

Figure VI.2. a) ^{1}H NMR and b) ^{13}C NMR spectra of 6OTC in DMSO-d6 at 80 °C.

As shown in Figure VI.2 a, the broad signal between 7.5 – 6.8 ppm corresponds to the aromatic protons of the trityl side groups of 6OTC that are attached to the C6 of AGU, accompanied by a broad signal around 5.8 – 2.7 ppm corresponding to the cellulose backbone protons. Moreover, sharp peaks at 2.1 and 3.3 ppm correspond to acetone and water, respectively. This is due to the fact that the product was first precipitated in a mixture of MeOH/water and then extracted by acetone in a Soxhlet extractor. According to the ^{13}C NMR spectrum of 6OTC illustrated in Figure VI.2 b, the product exhibits a clear signal at around 62 ppm, which corresponds to the functionalized C6 of the AGU, and no peak at 60 ppm that stands for the unfunctionalized C6. The signals for cellulose backbone can be found between 70 and 100 ppm. The signal around 85 ppm, and between 126 and 143 ppm correspond to the functionalized trityl side groups at C6 position. The results are in agreement with what has been previously reported by Erdmenger and colleagues [151]. The absence of interfering peaks, as well as the signal that presents the unfunctionalized C6 at 60 ppm, suggest that the DS of the 6OTC product should be around 1.

Electrospinning of 6OTC in solvent systems of DMSO and DMSO/acetone was conducted as a preliminary test to study the electrospinnability of 6-*O* functionalized cellulose derivatives and to compare the results with a possible future 6-*O*-Azo-Cel product. Solutions of 10 wt% 6OTC were prepared in 1 mL of the following solvent systems: DMSO; DMSO/acetone 7.5/2.5 v/v; DMSO/acetone 5/5 v/v; DMSO/acetone 2.5/7.5 v/v. Each solution was injected from a gas-tight syringe by 20 kV electrical charge at 10 µL min^{-1} through an 18GA needle gauge (inner diameter = 0.84 mm), 15 cm above a flat collector covered with Al foil to gather fiber-mats. Figure 9 presents the results at two different magnifications.

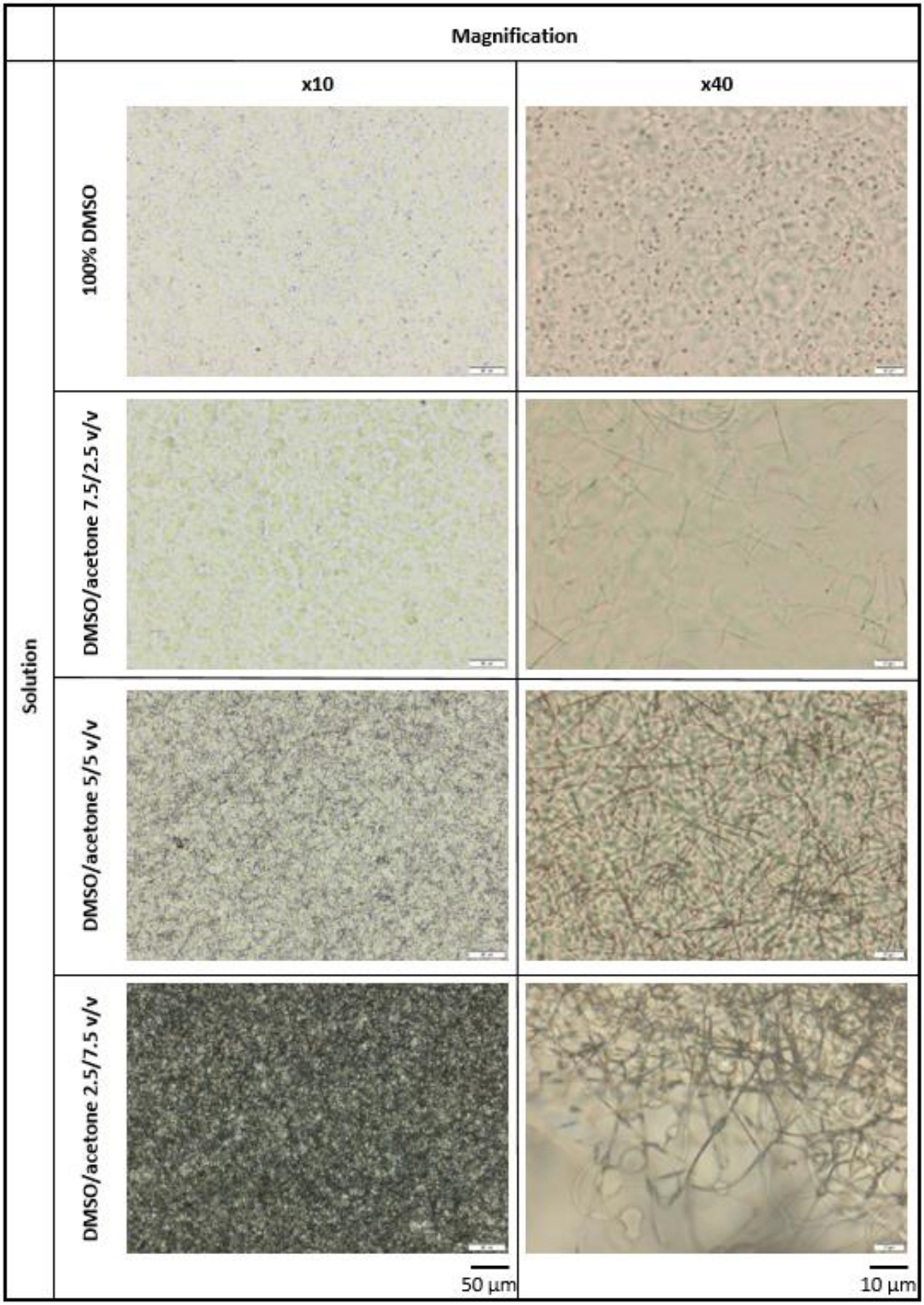

Figure VI.3. Optical micrographs of 6OTC electrospun products in different solvent systems.

As illustrated in Figure VI.3, the quality of fibers along with the possibility of bead transforming into fibers increases with the decrease of DMSO. 6OTC is soluble in DMSO and insoluble in acetone. Therefore, it was perfectly expected that a lower portion of good solvent, which means higher concentration of the polymer, would favor the fiber formation. These trials also showed that a regioselectively 6-*O* functionalized cellulose derivative that can form hydrogen bonds at C2 and C3 of AGU is still electrospinnable, which is a positive finding for the future of this study.

Electrospinning of 6OTC seems to be a success. These tests demonstrated that a regioselectively-functionalized cellulose derivative that can form hydrogen bonds at C2 and C3 of AGU (in this case 6OTC) is still electrospinnable, which is a positive finding for the future of this study and the future product of 6-*O*-Azo-Cel. After characterizing 6OTC by IR and NMR spectroscopy methods, it was esterified with Azo dye and 2,3-*O*-di-Azo-6-*O*-Trityl cellulose (di-Azo-monoTC) was produced. Di-Azo-monoTC was then characterized by IR and NMR spectroscopy methods to study the integrity of the chemical structure of the product. Figure VI.4 presents the ATR-FTIR spectrum of di-Azo-monoTC.

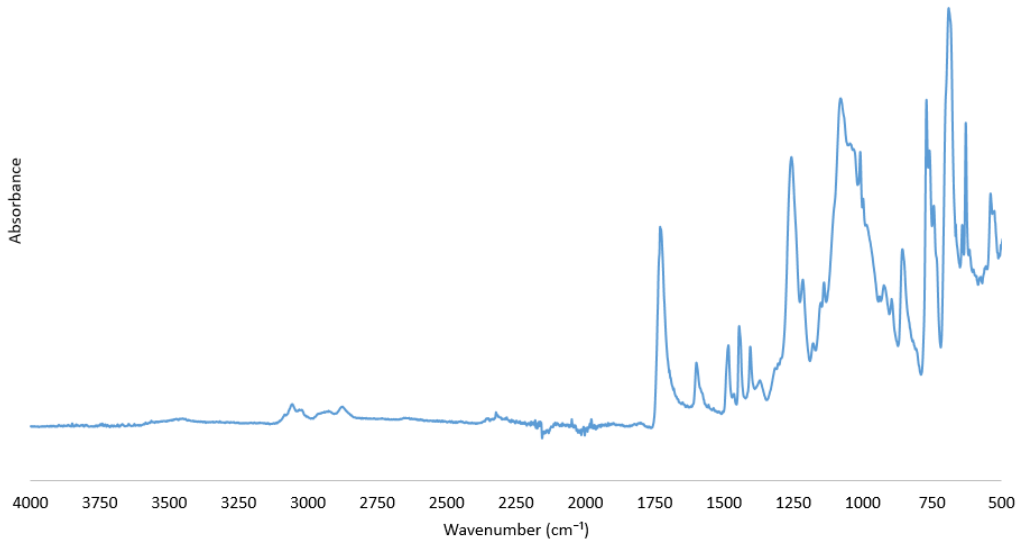

Figure VI.4. ATR-FTIR spectrum of di-Azo-monoTC.

The di-Azo-monoTC product exhibits signals of both side groups on its IR spectrum, *i.e.* Azo at 1723 cm^{-1} for C=O, 1603 cm^{-1} for C=C, 1258 cm^{-1} for C–O, as well as trityl between 600 and 770 cm^{-1} and at 3100 cm^{-1}. The absence of the band at around 3450 cm^{-1} that represents stretching band of –OH is an indication that the free hydroxyl groups of AGU in 6OTC are now functionalized with azo side groups.

Figure VI.5a presents the ^{1}H NMR spectrum of di-Azo-monoTC product. The broad signal between 7.3 – 6.7 ppm corresponds to the aromatic protons of the trityl side groups of the product that are attached to the C6, while the peaks between 8.1-7.4 ppm belong the Azo protons that are attached to C2 and C3 of AGU. The broad signal around 5.5 – 2.7 ppm corresponds to the cellulose backbone protons. Moreover, sharp peaks at 2.12 and 1.52 ppm represent acetone and water, respectively. On the ^{13}C NMR spectrum of di-Azo-monoTC product illustrated in Figure VI.4 b, the product exhibits clear signals that belong to both trityl and Azo side groups (see Figures II.8b for Azo and VI.2b for trityl signals).

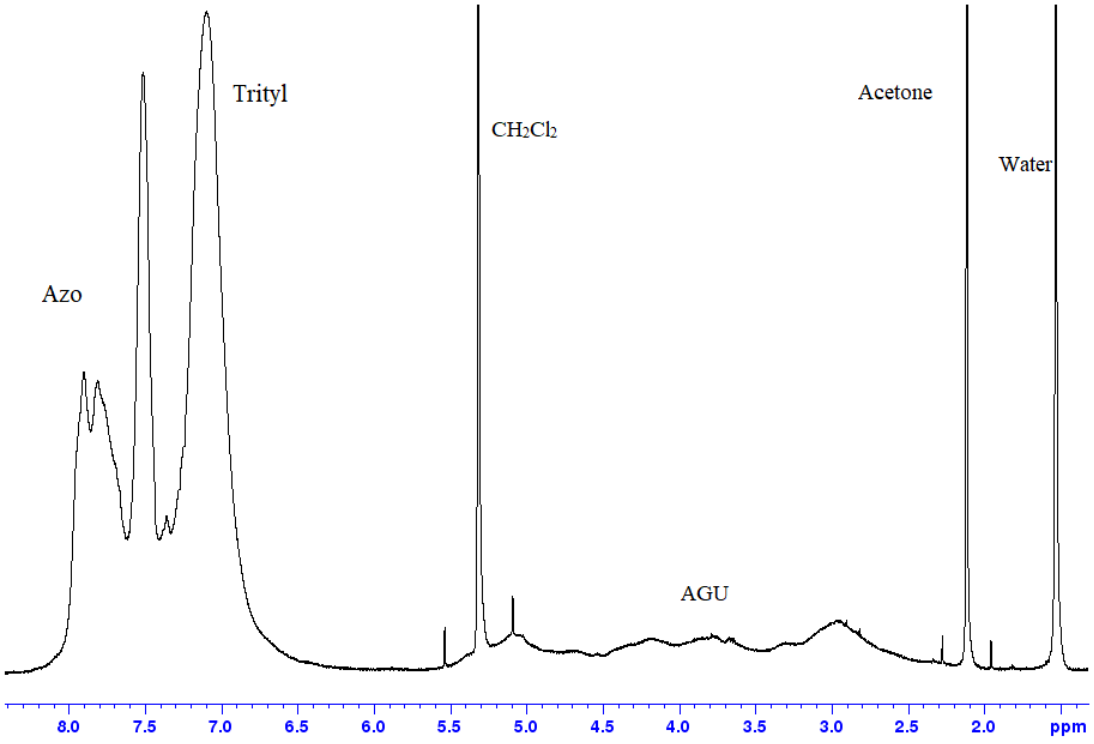

(a)

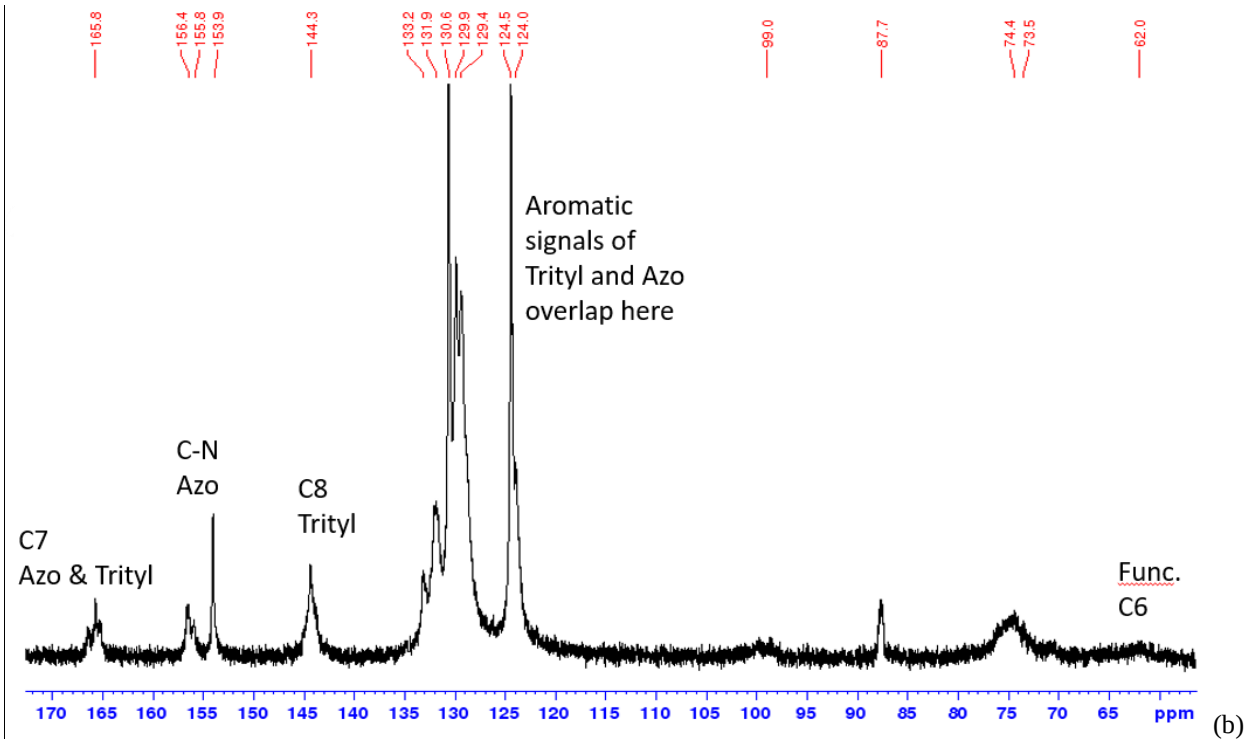

Figure VI.5. a) ^{1}H NMR spectrum of di-Azo-monoTC in CD_2Cl_2 at r.t. b) ^{13}C NMR spectrum of di-Azo-monoTC in CD_2Cl_2 at r.t (For more details refer to Figures II.8 b and VI.11 b).

Theoretical values of di-Azo-monoTC are as follows: 74.62% C, 4.91% H, and 6.83% N (theoretical value for DS_{azo} = 2, or 4 atoms of N per AGU). EA of the di-Azo-monoTC product gave the following percentages for each component of the product: 75.16% C, 5.10% H, and 6.10% N. According to these results, each AGU block of the di-Azo-monoTC polymer must contain about 3.55 atoms of N in average; therefore, it is estimated that the DS of the azo group in the product is 1.77.

Judging by the absence of free C6 signal (unfunctionalized primary hydroxyl group of AGU) on the ^{13}C NMR spectrum, as well as the absence of –OH stretching band on the IR spectrum and the solubility of the product in common organic solvent, as well as the EA results, we conclude that the product is 2,3-*O*-di-Azo-6-*O*-trityl cellulose.

According to literature, treating with concentrated HCl at room temperature can selectively deprotect [162–166] the ether linkage between the trityl group and C6 carbon. Therefore, we followed the reported method and tried the detritylation of di-Azo-monoTC in THF with 300 µL of concentrated HCl (37%) at room temperature over 72 h. Figure VI.6 presents the evolution of detritylation reaction over 72 h.

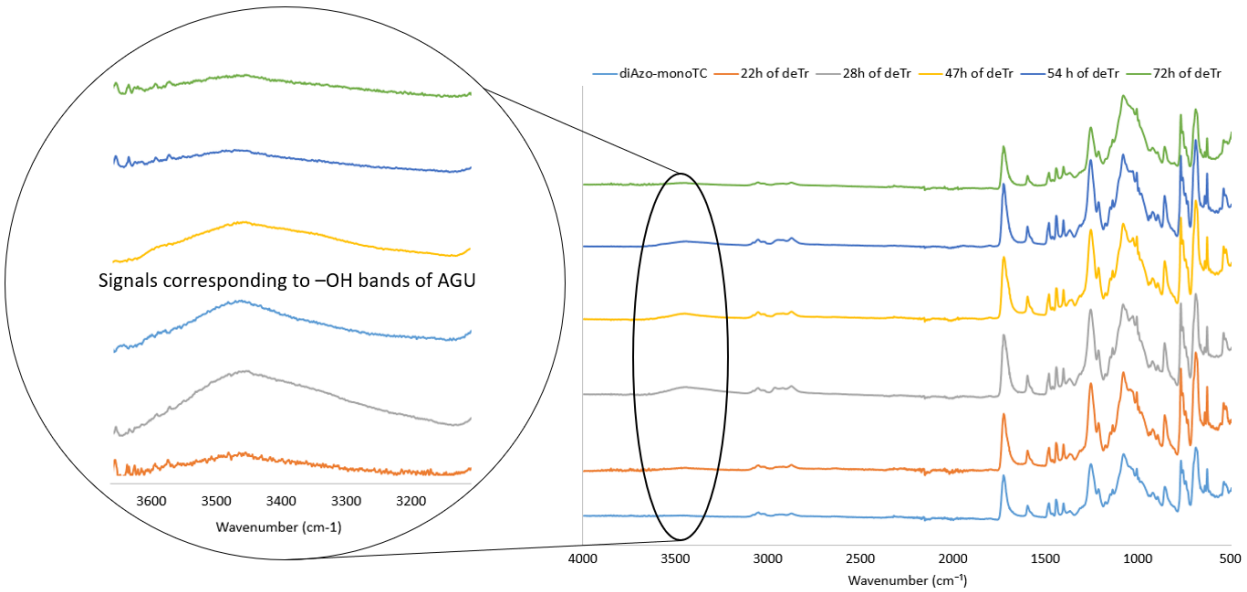

Figure VI.6. IR spectra of di-Azo-monoTC product being detritylated over 72 h. Comparative spectra (right) vs zoomed spectra of –OH bands (left).

It seems that by allowing the detritylation continue over time, the stretching band of –OH groups at 3450 cm^{-1} becomes stronger and the assigned trityl peaks (3059 cm^{-1}, 1065 cm^{-1}, and 703 cm^{-1})[151] weaker. The final product of this step (we call it HA-2-14) was vacuum dried overnight at 70 °C and characterized through ^{1}H NMR spectroscopy (Figure VI.7).

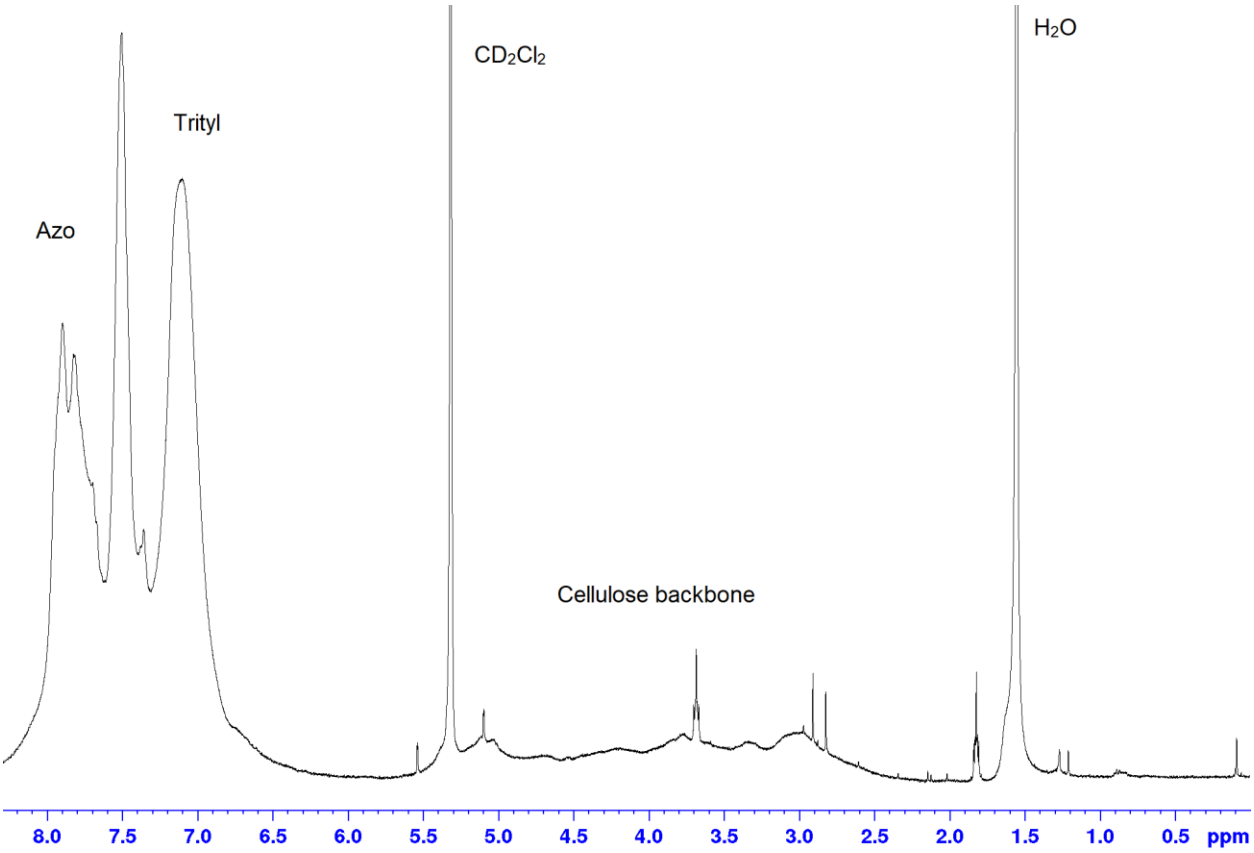

Figure VI.7. ^{1}H NMR spectrum of detritylated product (HA-2-14) in CD_2Cl_2 at r.t. Trityl peaks still appear between 6.9 and 7.3 ppm.

Trityl-corresponding signals still appear on the ^{1}H NMR spectrum, meaning that probably the amount of added acid was not sufficient to completely deprotect the trityl side groups. For the next step, 300 µL of concentrated HCl was added to the reaction at the beginning, and every 3 hours 100 µL was added and after sampling several drops of the reaction moiety, the IR spectrum was acquired. Figure VI.8 illustrates the evolution of detritylation process (product HA-2-16) after consistent addition of acid.

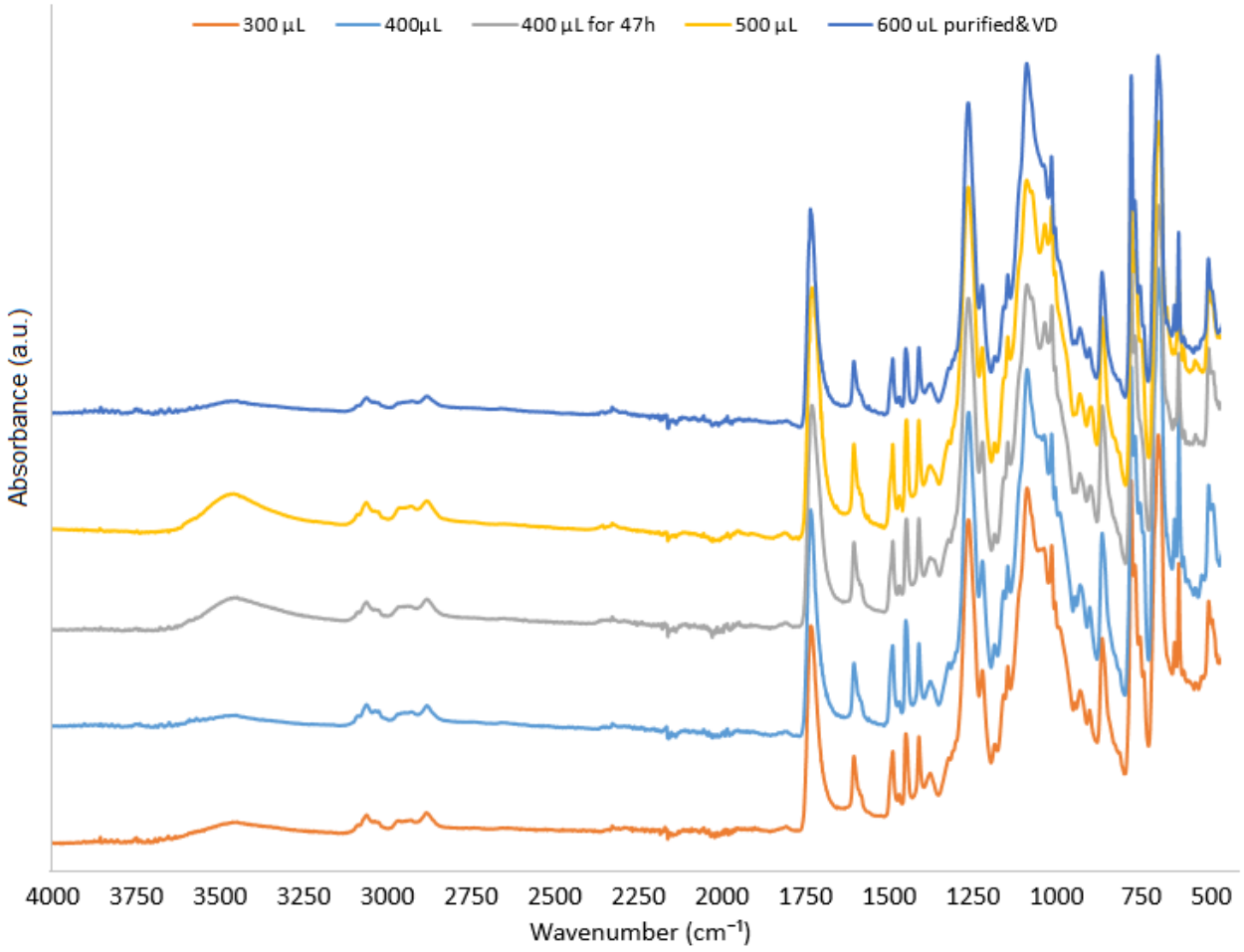

Figure VI.8. IR spectra of di-Azo-monoTC product (HA-2-16) being detritylated over 72 h and consistent addition of acid.

Again, it seems that by allowing the detritylation continue over time, the stretching band of –OH groups at 3450 cm^{-1} becomes stronger and the assigned signals weaker. Yet strong signals attributed to trityl side groups still appear on the ^{1}H NMR spectrum of the product HA-2-16 between 6.9 and 7.3 ppm (Figure VI.9).

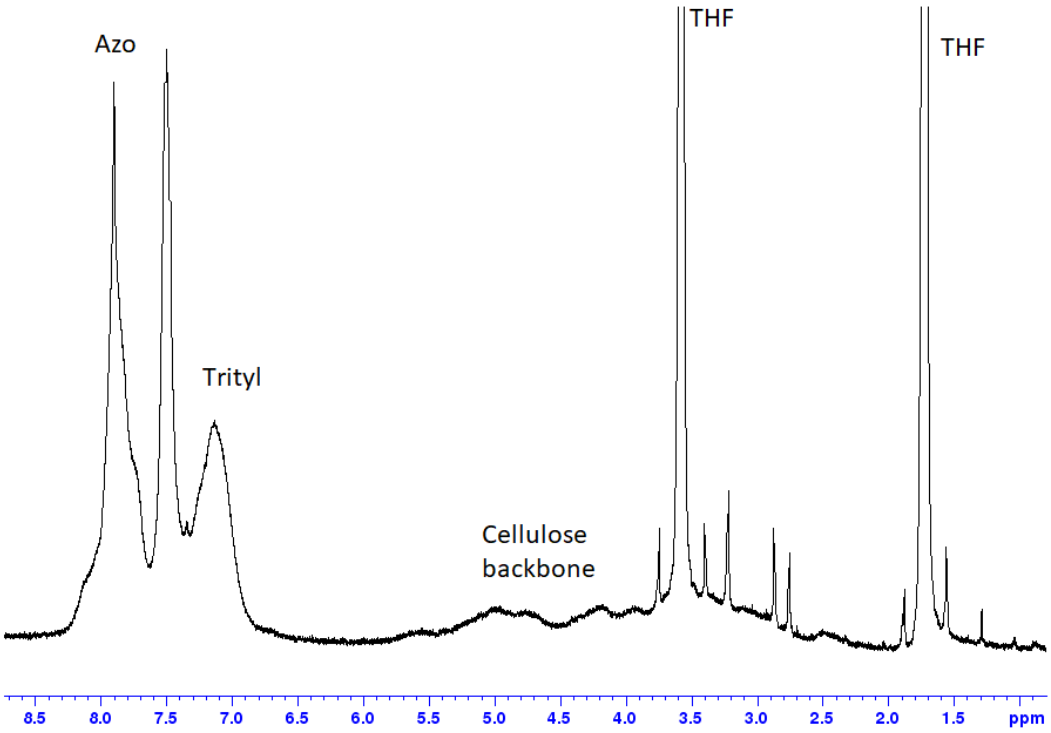

Figure VI.9. ^{1}H NMR spectrum of detritylated product (HA-2-16) in THF-d_8 at r.t.

Judging by the reduced intensity of the assigned trityl signals on the ^{1}H NMR spectrum, one can assume that the addition of acid helps with the detritylation process, but it is not the ultimate and effective approach as there are still side groups on the AGUs of the product that are not deprotected. It has been studied that raising the temperature of a reaction moiety may accelerate the reaction or increase the efficiency [167–170]. Hence, another detritylation reaction was launched, but this time with 600 µL of concentrated HCl in THF at 60 °C. The reaction continued for 72 h at the mentioned conditions, after which the product (labelled HA-2-49) was extracted, dried, and characterized by ATR-FTIR spectroscopy (Figure VI.10). The broad signal at around 3450 cm^{-1} belongs to the reappeared –OH stretching bands of AGU in the di-Azo-Cel product, and almost all the manifested trityl signals between 600 and 770 cm^{-1} and at 3045 cm^{-1}, disappeared.

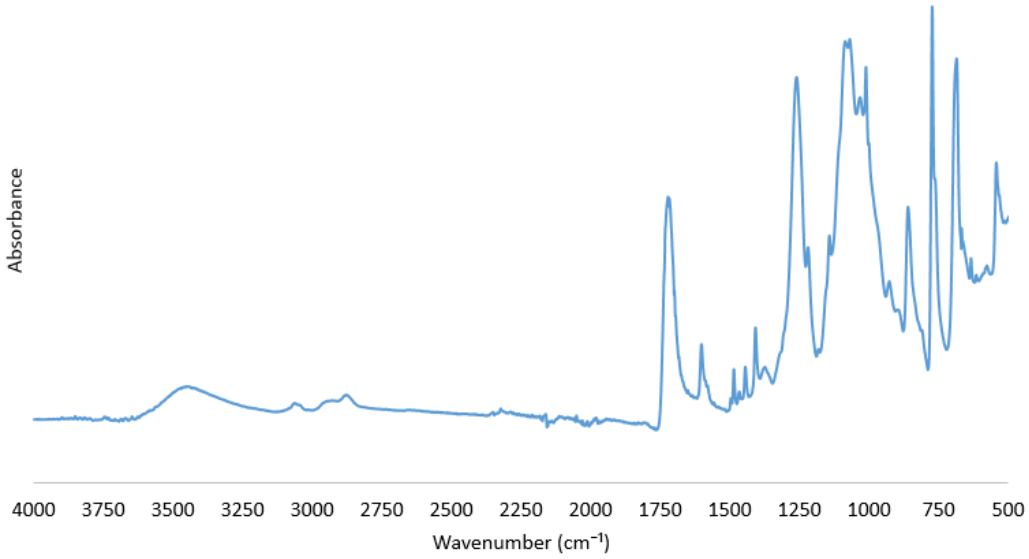

Figure VI.10. IR spectrum of the product HA-2-29.

On the ^{1}H NMR spectrum of di-Azo-Cel (HA-2-49) illustrated in Figure VI.11a, it is observable that the broad signal which used to appear between 7.3-6.8 ppm disappeared, while the azo signals between 8.2-7.5 ppm still appear on the spectrum. Same observation was witnessed on the ^{13}C NMR spectrum of di-Azo-Cel (Figure VI.11b).

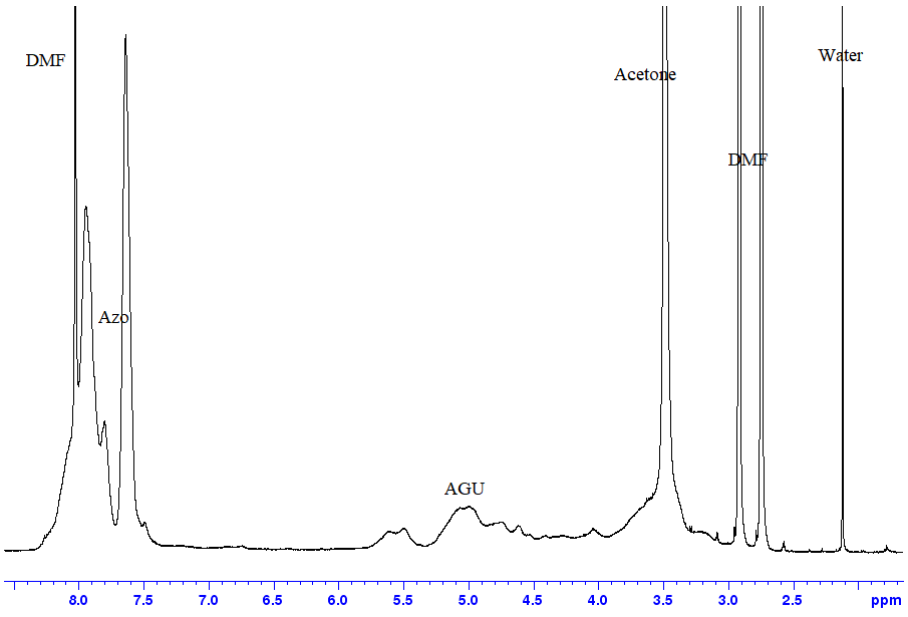

(a)

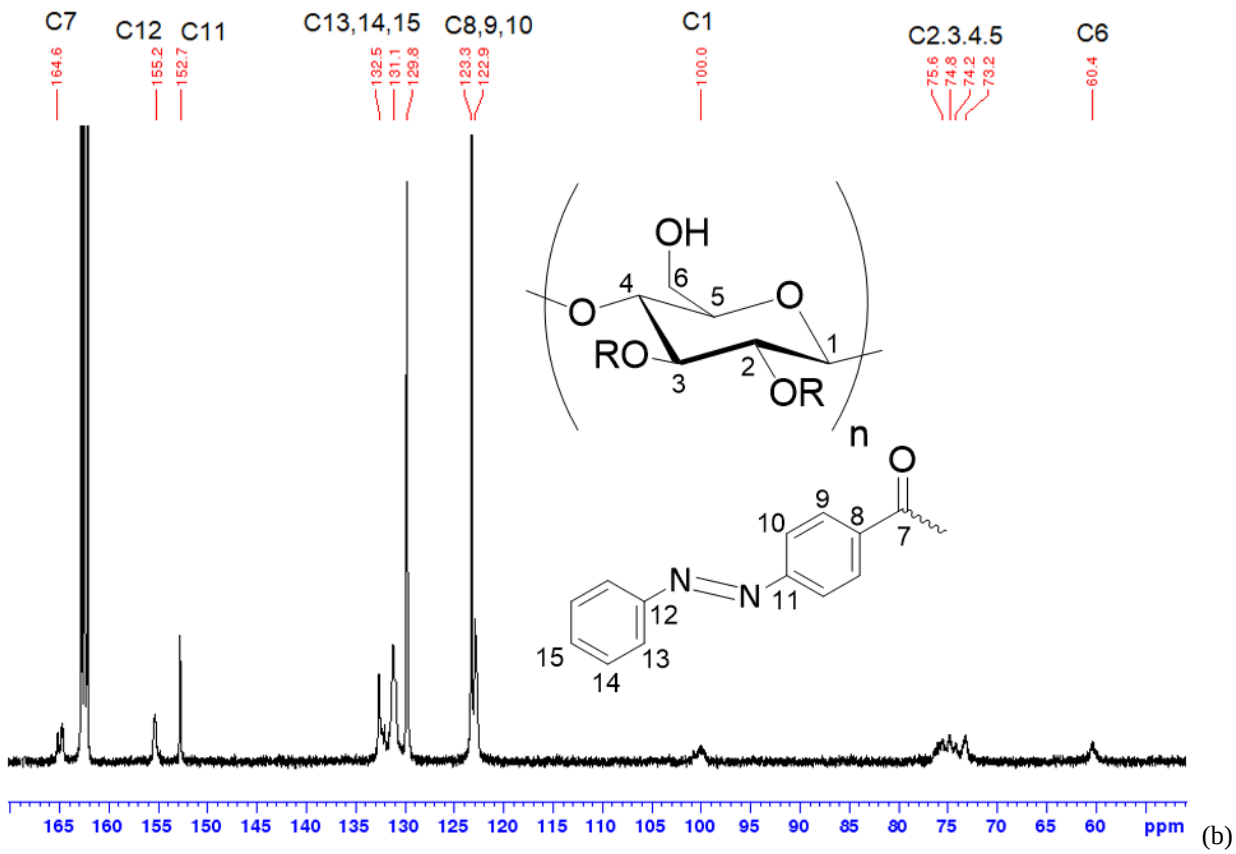

Figure VI.11. a) ^{1}H NMR and b) ^{13}C NMR spectra of the product HA-2-29 in DMF-d_7 at r.t.

The signal that appears at 60 ppm corresponds to the free –OH group at C6, while no signal emerges at 62 ppm that would present the functionalized C6 of the AGU. In addition, signals at around 85, 126, and 143 ppm that corresponded to the functionalized trityl side groups at C6 position disappeared from the spectrum of this product, yet the signals that represent azo bonds (see Figure II.8b) remain on the spectrum.

Theoretical EA values of di-Azo-Cel product are as follows: 66.43% C, 4.53% H, and 9.68% N (theoretical value for DS_{azo} = 2 or 4 atoms of N per AGU). EA of the HA-2-29 product gave the following percentages for each component of the product: 60.24% C, 4.91% H, and 7.24%

N. According to these results, each AGU block of the product HA-2-29 must contain about 3.34 atoms of N in average; therefore, it is estimated that the DS of the azo group in the product is 1.67. This slight decrease of the Azo group after the detritylation could be due to a combination of reaction circumstances, *i.e.* the product being in contact with highly concentrated HCl at high temperature over an extended amount of time breaks some of the ester linkage with the Azo group.

T_d of di-Azo-Cel product (HA-2-29) was measured by TGA by applying the same protocol as Azo-Cel (See chapter II). As presented in Figure VI.12 the slope of the TGA curve starts to dramatically drop at around 281 °C, which is determined to be the T_d of di-Azo-Cel. The T_d of di-Azo-Cel is lower than that of Azo-Cel (286 °C), one hypothesis − that can be extrapolated from literature[108] − is that that having free –OH groups that are able to form hydrogen bonds is the reason for this drop of T_d value.

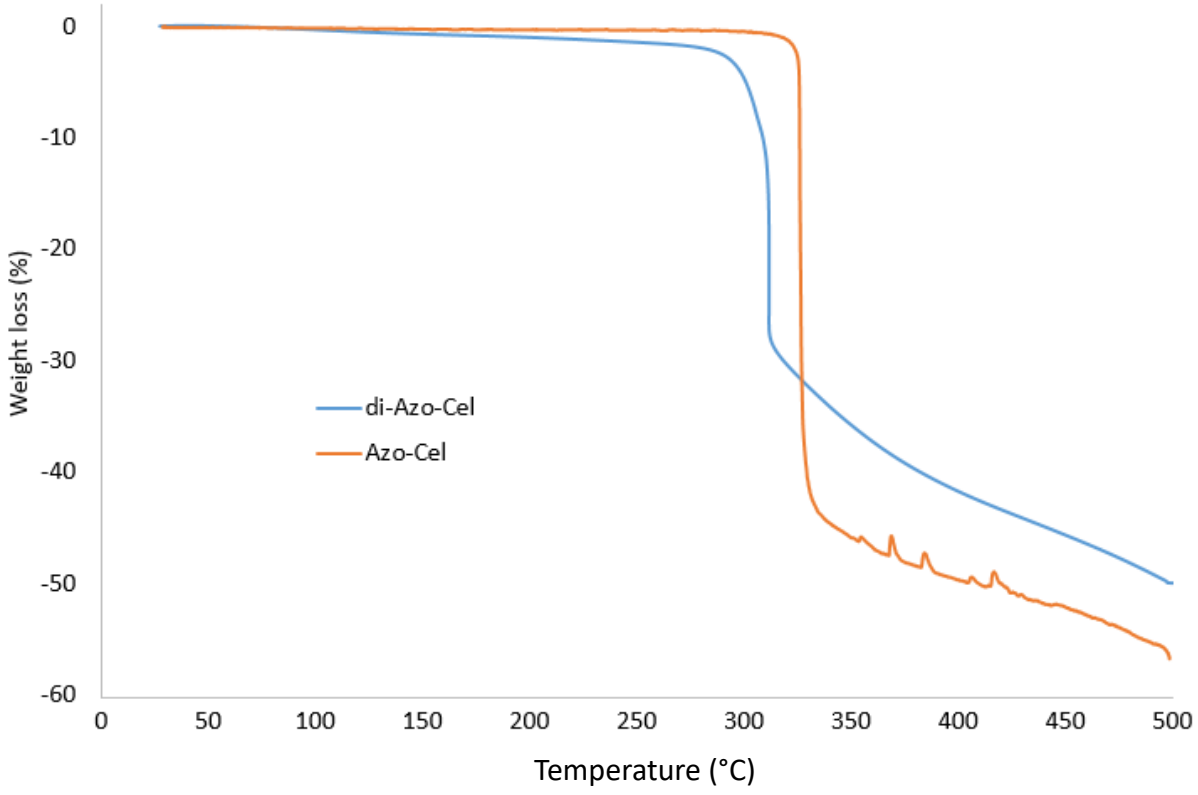

Figure VI.12. TGA curves of di-Azo-Cel (blue) and Azo-Cel (orange).

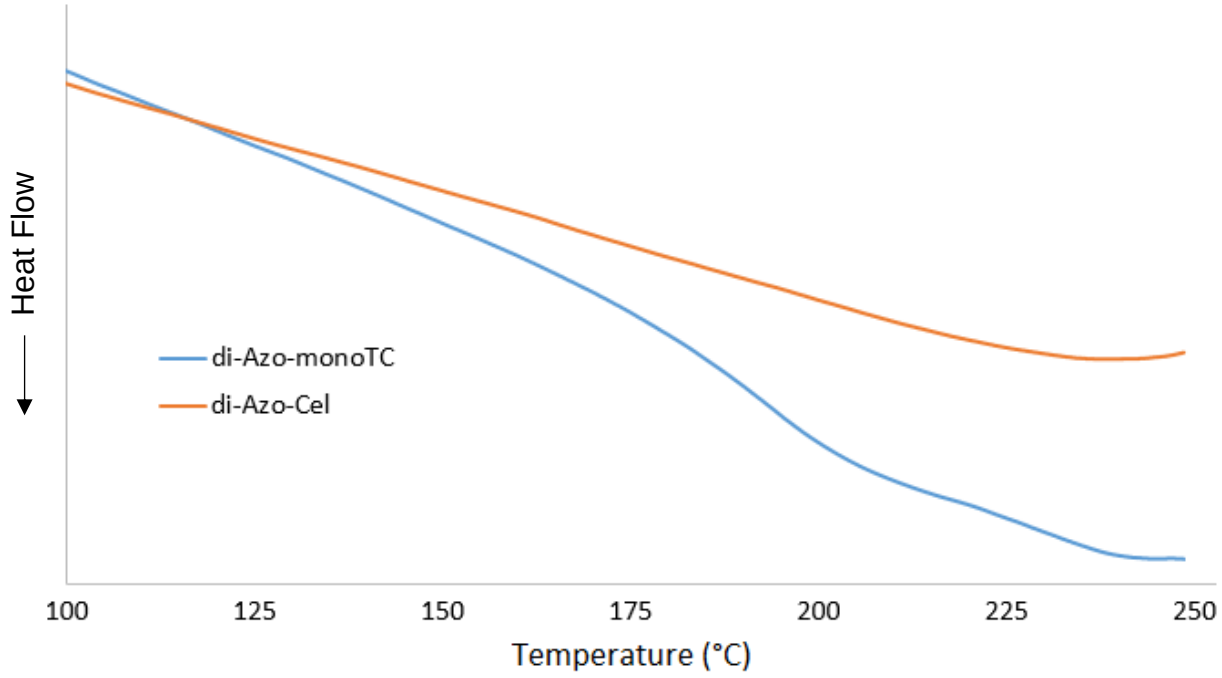

Figure VI.13. DSC traces of di-Azo-monoTC (blue) and di-Azo-Cel (orange).

Figure VI.13 illustrates the DSC traces of the second heating cycle of both di-Azo-monoTC and di-Azo-Cel products by comparing heat flow vs temperature. As it is visible, di-Azo-Cel shows no clear thermal flow change, probably because of the presence of hydrogen bonds between polymer chains. The di-Azo-Cel product shows a T_g of around 185 °C. This is a higher value compared to Azo-Cel (T_g = 176 °C) and in line with what has been stated in literature. In 2003 Gomez-Carracedo and colleagues reported that by increasing the DS − for non-Ionic cellulose ether products − the T_g decreases [108]. In this case, Azo-Cel, which has a higher DS, shows a lower T_g compared to di-Azo-Cel with lower DS.

UV-vis of di-Azo-monoTC and di-Azo-Cel was carried out in solutions of THF with equal concentration for both solutions. Figure VI.14 presents the results.

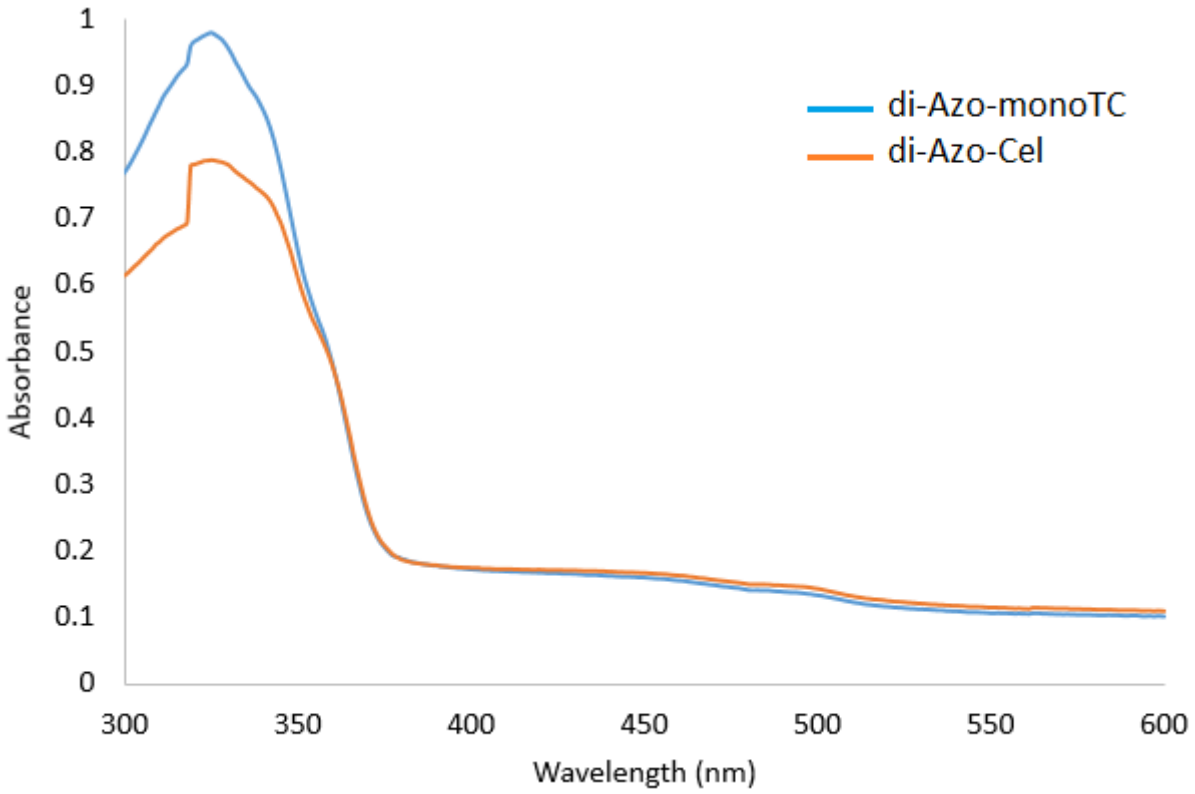

Figure VI.14. UV-vis measurement of di-Azo-monoTC and di-Azo-Cel in THF.

As illustrated in Figure VI.14, there is an almost clear peak at around 330 nm that is attributed to the π-π* electron transition of AB functional groups, whereas the weak absorption band at around 450 nm belongs to the n-π* electron transition of the AB moiety in the compound. It seems that the n-π* absorption band in both di-Azo-monoTC and di-Azo-Cel is weakened compared to that of Azo-Cel (see Figure II.9), probably due to the lower molar ratio of Azo side groups. Additionally, di-Azo-Cel shows a weaker π-π* absorption band compared to di-Azo-monoTC. One hypothesis is the slightly lower DS_{azo} of di-Azo-Cel after detritylation.

The di-Azo-Cel product has been solubilized in the following organic solvents to study its solubility for electrospinning: DMSO, DCM, DMAc, THF, DMF, Toluene, acetone, and Chloroform. Figure VI.15 presents the state of solubility of the solutions.

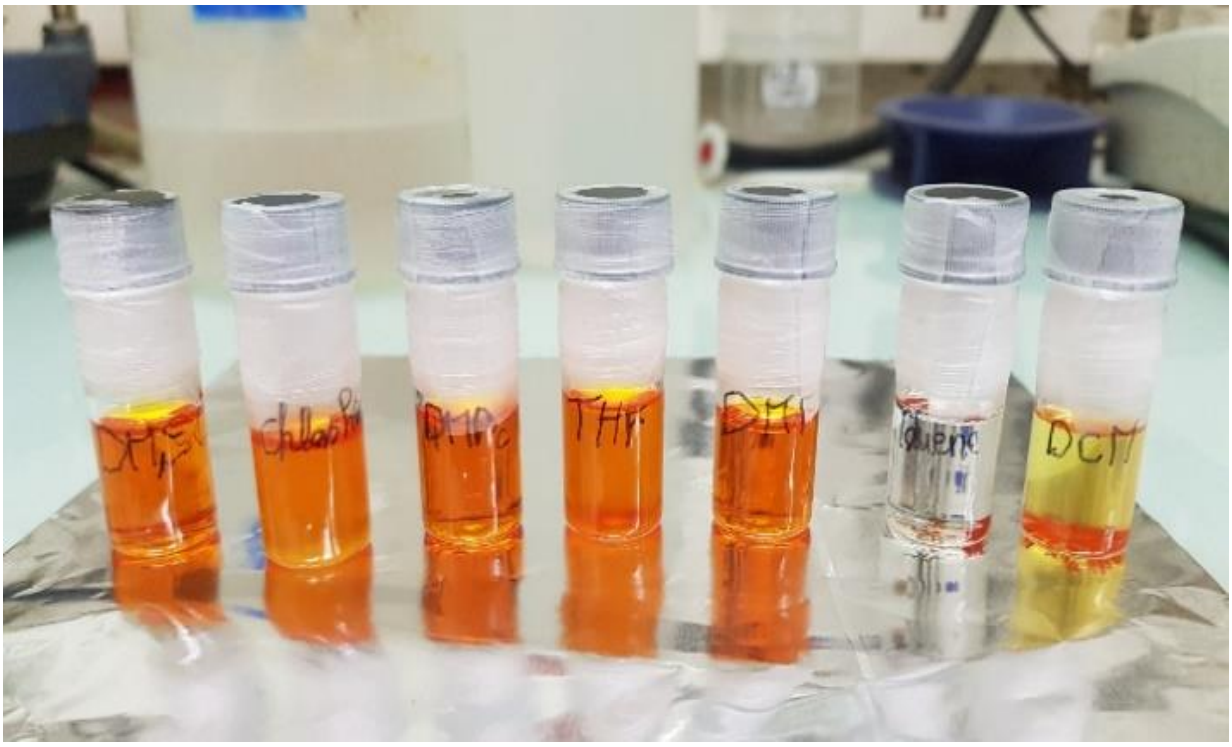

Figure VI.15. Solubility of di-Azo-Cel in several organic solvents after 8 h of stirring.

Table VI.1. Summary of solubility check tests for di-Azo-Cel.

Solvent	Solubility *	Remarks
DMSO	+	Perfectly soluble and clear solution.
Chloroform	×	Partially soluble. Shady solution. Better than DCM.
DMAc	+	Perfectly soluble and clear solution.
THF	+	Partially soluble. Shady solution. But better than chloroform.
DMF	+	Perfectly soluble and clear solution.
Toluene	-	Insoluble.
DCM	×	Partially soluble. Shady solution. Swollen polymer powder.
Acetone	-	Insoluble.

* Soluble (+). Partially soluble (×). Insoluble (-).

Table 1 summarizes the solubility of di-Azo-Cel in common organic solvents. To prepare solutions, 5 mg of di-Azo-Cel was first introduced to the respective test solvent, magnetic stirred for 8 h, and then rested overnight at dark. The day after they were examined and each solution demonstrated different solubility. Judging by the state of solutions, *i.e.* clarity and presence of precipitates, the solubility of di-Azo-Cel in organic solvents is classed as follows: DMF > DMAc > DMSO > THF > Chloroform > DCM > Toluene > Acetone.

The di-Azo-Cel polymer in DMF and DMAc gives perfectly clear solutions with no precipitates or swollen polymer at all, while it is mostly soluble in DMSO and THF, leaving mild to moderate precipitates in the solvent. The polymer is partially soluble in chloroform with moderate precipitation, less soluble in DCM with heavy precipitate and swollen polymer, and insoluble in toluene and acetone.

Electrospinning of di-Azo-Cel

During the electrospinning of Azo-Cel (DS = 2.83), it was found that a solvent system of acetone/DMAc provided a stable electrospinning process of Azo-Cel to form continuous nanofibers when the polymer concentration was fixed to 17 wt% (see chapter III.3). Therefore, di-Azo-Cel was solubilized at the same concentration in the same solvent system and then electrospun at optimized electrospinning conditions. Figure VI.16 presents the optical micrographs of the results.

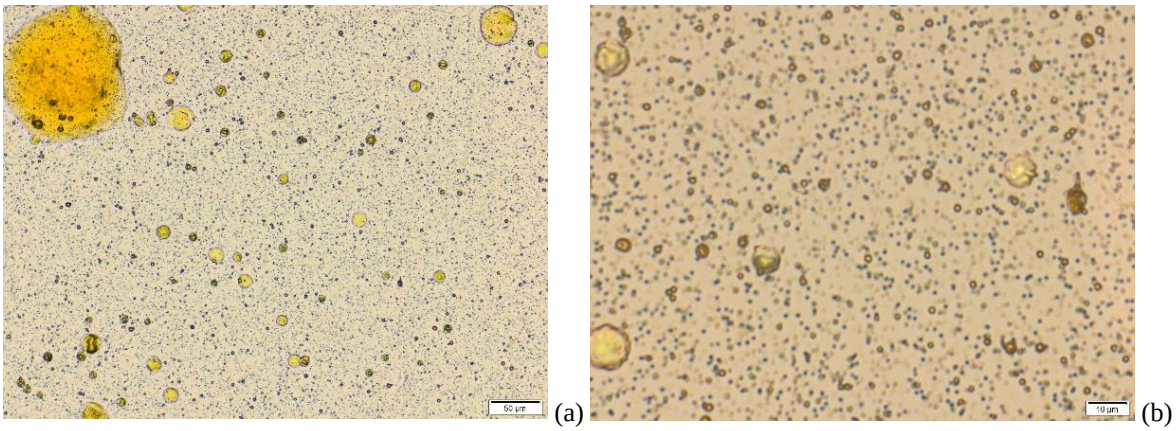

Figure VI.16. Optical micrographs of di-Azo-Cel electrospun product 17 wt% in acetone/DMAc 3/2 (v/v). a) x10 (50 µm) and b) x40 (10 µm) magnifications.

As it appears in Figure VI.16, the product did not manage to produce fibers in acetone/DMAc solvent system. Thus, various solvent systems were utilized to find an optimum moiety for fiber production of di-Azo-Cel, such as acetone/DMF, THF/DMAc, THF/DMF, acetone/DMSO, and 100% DMAc, with different concentrations and solvent ratios. Electrospinning at 25 kV, by 10 µL/min through 20GA needle 15 cm away from the collector showed to be the most stable condition for all systems. However, no solvent system produced fibers. Figure IV.15 presents the optical micrographs of electrospun products in the above-mentioned solvent systems. As Figure VI.17 illustrates, none of the mentioned solvent systems managed to produce neither stable electrospinning and polymer jet, nor continuous fiber production because every time the solution was agglomerated at the tip of the needle and impeded the electrospinning process.

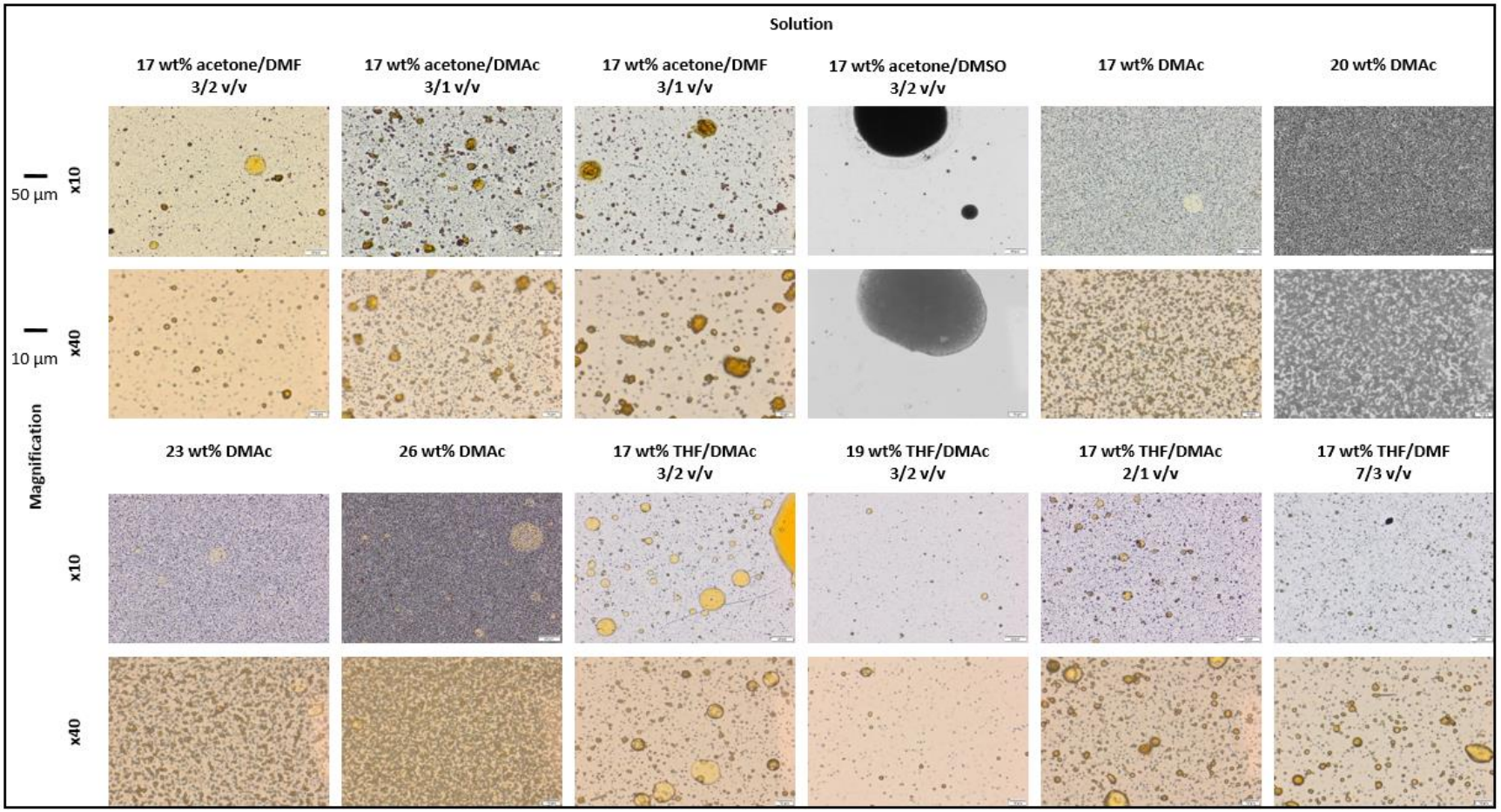
Solution
17 wt% acetone/DMF 3/2 v/v
17 wt% acetone/DMAc 3/1 v/v
17 wt% acetone/DMF 3/1 v/v
17 wt% acetone/DMSO 3/2 v/v
17 wt% DMAc
20 wt% DMAc
50 µm
x10
10 µm
x40
Magnification
23 wt% DMAc
26 wt% DMAc
17 wt% THF/DMAc 3/2 v/v
19 wt% THF/DMAc 3/2 v/v
17 wt% THF/DMAc 2/1 v/v
17 wt% THF/DMF 7/3 v/v
x10
x40

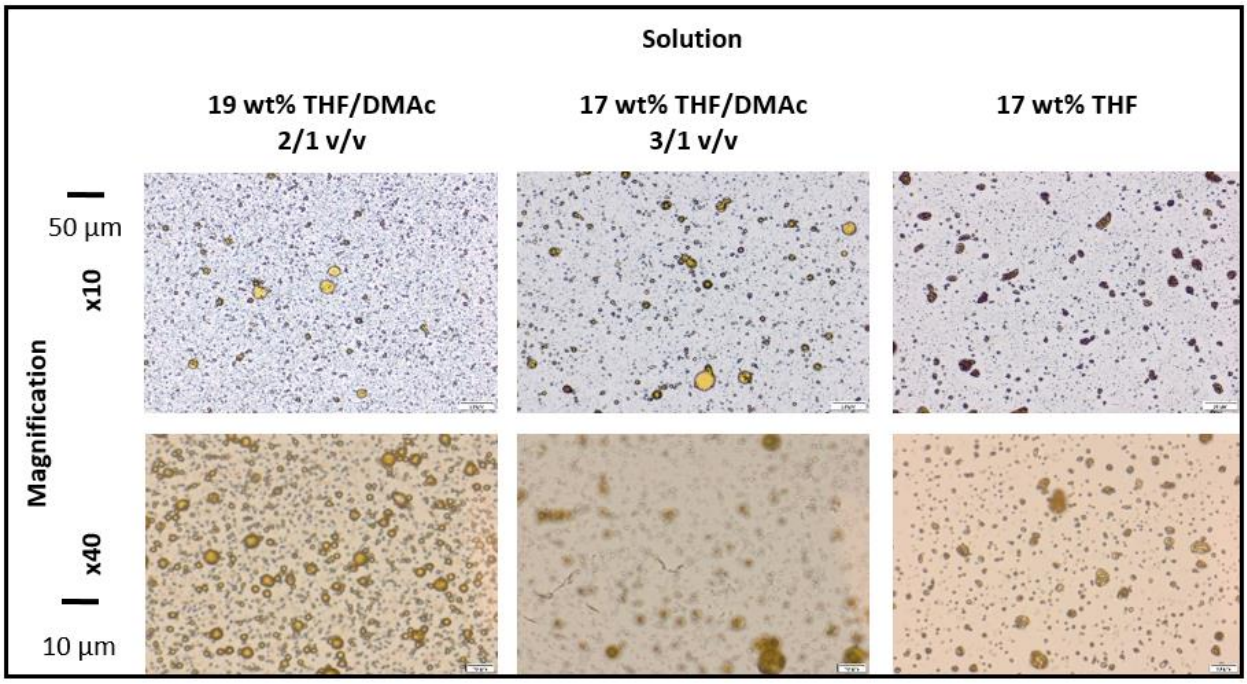

Figure VI.17. Optical micrographs of 2,3-*O*-Azo-Cel electrospun products in different solvent systems. Note: the solvent 20 wt% in acetone/DMAc 3/2 v/v was so viscous that it could not be drawn into the syringe to be electrospun.

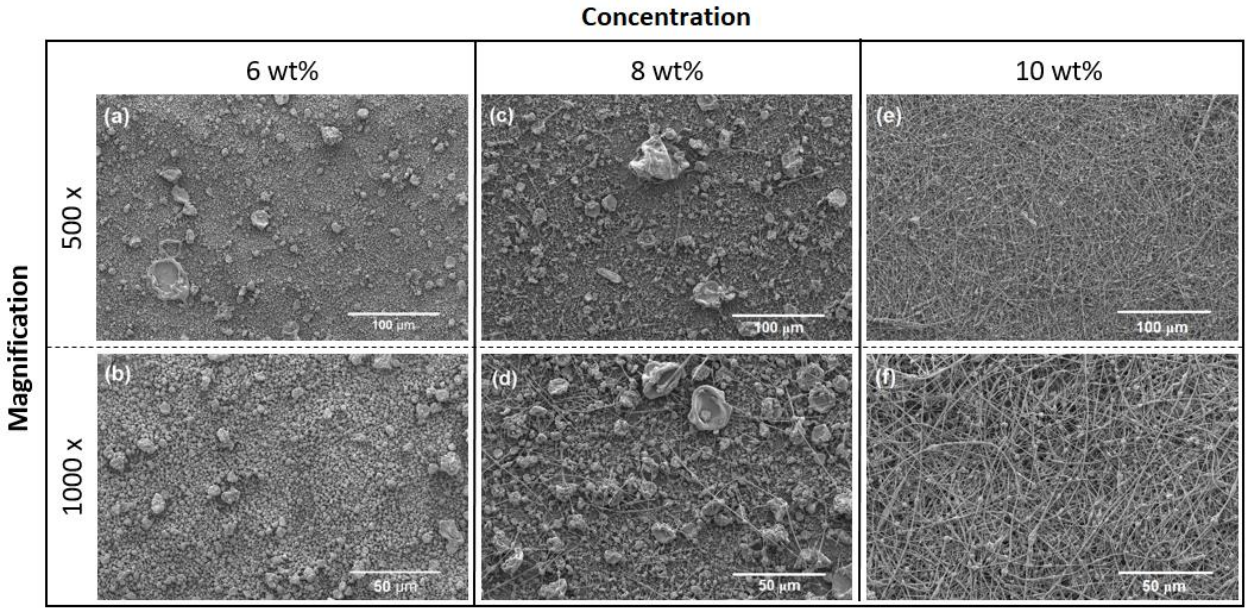

Figure VI.18. SEM observations of di-Azo-Cel products in a solvent system of DCM/DMF 3/1 (v/v) with 6, 8, and 10 wt% polymer concentrations and different magnifications.

After confronting unproductive results, a solution of di-Azo-Cel in DCM/DMF 3/1 (v/v) was prepared, as it had previously managed to procure continuous fibers, albeit unstable electrospinning conditions. Samples of three different polymer concentrations of 6, 8, and 10 wt% were and electrospun using a 20 GA needle gauge under 25 kV electrical charge at 10 μL/min on a flat collector that had been covered with Al foil and placed 15 cm below the gas-tight syringe, filled with the polymer solution. Figure VI.18 presents the SEM observations of these trials.

As presented in Figure VI.18 a,b the electrospun products from the 6 wt% solutions displayed spherical beadlike structures probably because the viscosities and/or the surface tensions of the polymer solutions were insufficient against the applied electrostatic force so that the polymer solutions quickly sprayed away from the tip of the needle in the form of spherical droplets. By increasing the concentration to 8 wt %, a number of fibers coexisting with spherical beads were formed as shown in Figure VI.18 c,d. Further increase of the concentration to 10 wt% fostered the formation of continuous fibers as presented in Figure VI.18 e,f although some spherical and spindle beads still existed. Increasing the concentration above 10 wt% led to the coagulation of the polymer solution at the tip of the needle during electrospinning.

For the preparation of the self-standing di-Azo-Cel fabric, first a layer of PEO was electrospun on a rotary drum collector, covered with Al foil, then di-Azo-Cel was electrospun on PEO on Al foil. Afterward, the Al foil coated with the double-layered “di-Azo-Cel on PEO” textile was removed from the drum electrode and cut into small pieces. The specimen was then immersed in deionized water, which is a good solvent of PEO but a non-solvent of di-Azo-Cel, to solubilize the PEO layer and detach the di-Azo-Cel layer from the Al foil without any physical pressure on the textile. After half a day, the PEO layer was completely dissolved and the di-Azo-Cel layer was

detached from the Al foil as a floating textile that was dried under vacuum at 70 °C overnight to obtain a self-standing Azo-Cel fabric.

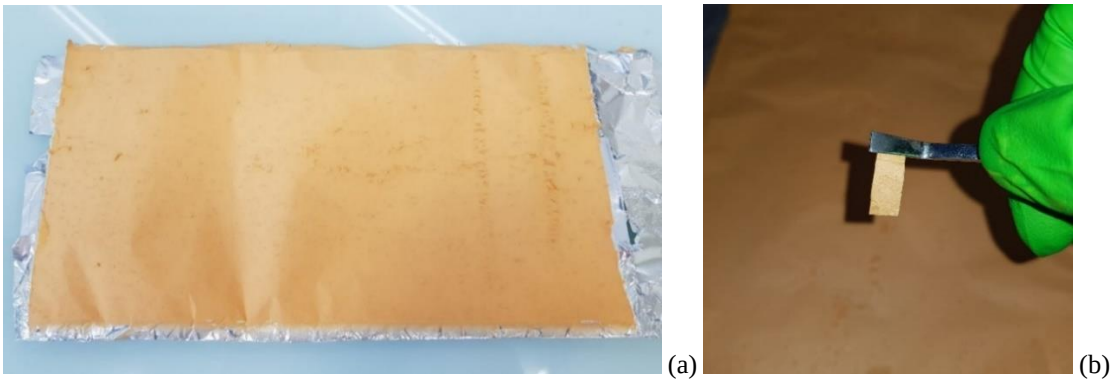
(a) (b)

Figure VI.19. a) Self-standing di-Azo-Cel textile on PEO on Al foil. Visibly, di-Azo-Cel has a lighter shade of orange than Azo-Cel. This is because of the reduced quantity of azo side groups in the product. b) di-Azo-Cel membrane separated and prepared for analysis. The membrane appears to have a brighter shade of orange compared to Azo-Cel due to a decreased amount of azo side groups present in the product.

Employing a rotary drum electrode for the fabrication of the self-standing di-Azo-Cel textile has led to two major ameliorations; a decrease in number of beads and an alignment of fibers in the direction of rotational force, thanks to the effect of high-speed rotation of the electrode, *i.e.* the fibers are taken up on the rotating surface of the cylinder resulting in the alignment and stretching of the electrospun fibers [7]. Figure VI.20 presents the results.

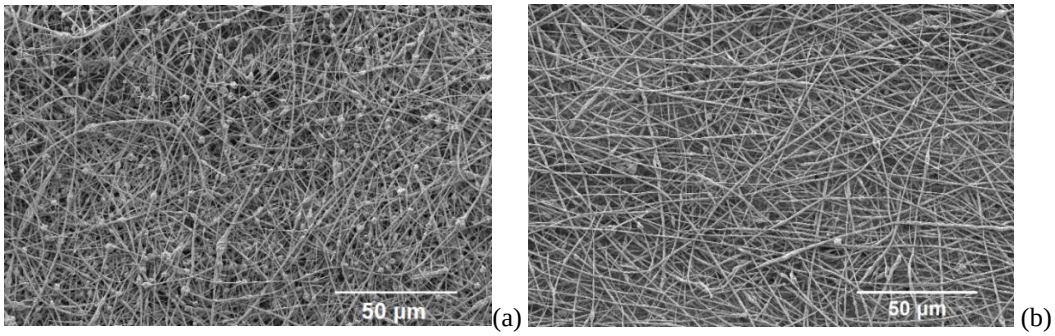

(a) (b)

Figure VI.20. SEM observations of a) randomly assembled and b) uniaxially aligned di-Azo-Cel fabrics. It appears that the overall number of beads diminished after introducing rotary force to the electrospinning process.

The di-Azo-Cel self-standing textile is consisted of somewhat uniaxially aligned fibers. The fibers in this product seem to be less aligned than those in Azo-Cel. One can assume that the presence of more free –OH groups that are able to form intramolecular hydrogen bonds is the reason behind this phenomenon; meaning that the backbone polymer chains in di-Azo-Cel have less capacity of moving freely, therefore showing more resistance to high tension caused by the electric field of the electrospinning machine and less alignment.

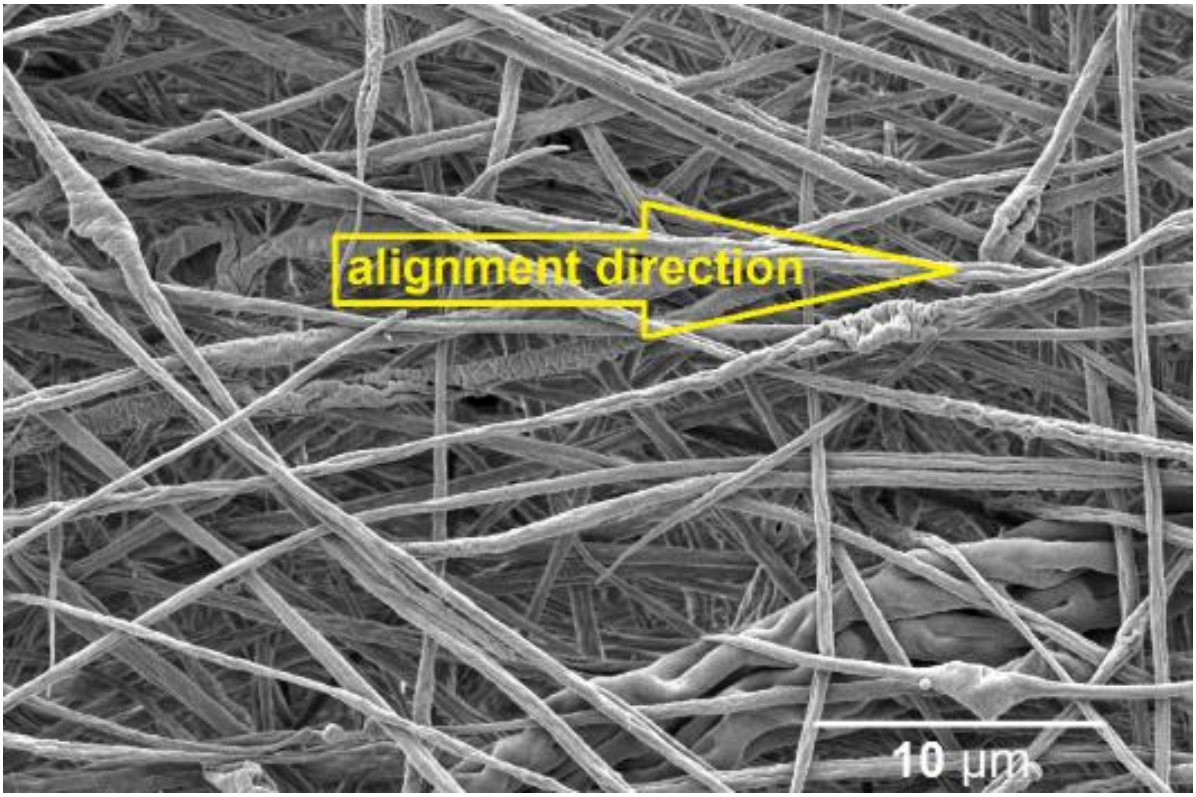

Figure VI.21. a) Alignment direction of fibers in self-standing di-Azo-Cel fabric.

The tensile strength of the self-standing di-Azo-Cel fabric was characterized with a similar method as described in chapter IV.2. The fabric shows a maximum of 1.48 MPa stress at breakage point with a total strain of 1.8 %. The presence of–OH groups that form intramolecular hydrogen bonds could be the reason behind the elevated tensile strain (almost three times compared to that of Azo-Cel) of di-Azo-Cel. Because of the hydrogen bonds, the polymer chains do not break easily

and move upon each other more freely (because of the fewer Azo side groups), causing a lower amount of force required to break the chains, and higher deformation. Figure VI.22 illustrates the stress-strain curve of the di-Azo-Cel fabric.

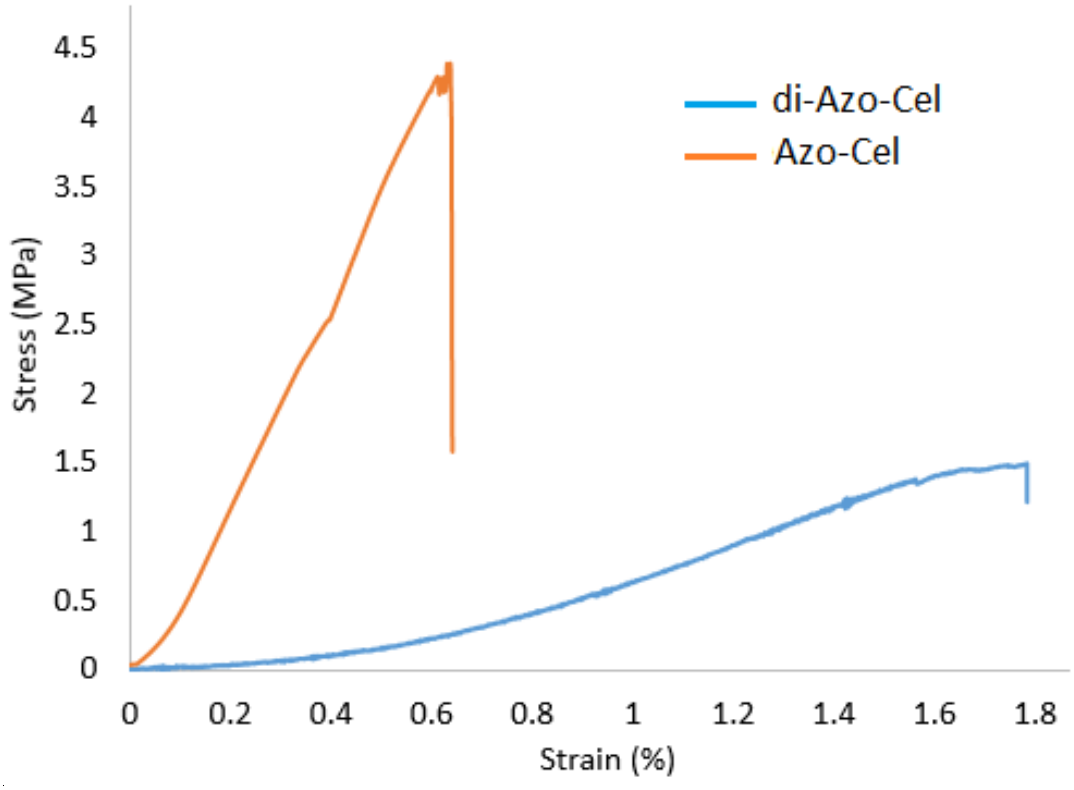

Figure VI.22. Stress-strain curve of di-Azo-Cel fabric (Compressed thickness of the fabric is at 39 µm, measured by IP65 Vernier scale).

VI.3.3. Photo-responsivity of di-Azo-Cel Textile

Photo-responsivity of di-Azo-Cel textile was studied through the same two methods of wettability characterization by WCA and UV-induced photo-actuation analysis, as described in chapter V.3. Same parameters are applied herein and the di-Azo-Cel is characterized according to the same procedures. WCA of a di-Azo-Cel fabric was first measured under the visible light of the room as it was obtained, then the same di-Azo-Cel fabric was irradiated with UV light (λ = 355–375 nm) for 15 min followed by its WCA measurement. Afterward, the specimen was exposed to

visible light for 30 min followed by measuring its WCA again. This procedure was repeated for 5 cycles and variation of the WCA was plotted in Figure VI.23, where the diagram represents the values of 4 sets of the measurements using different pieces of di-Azo-Cel fabric, and the error bars represent their maximum and minimum values for each point.

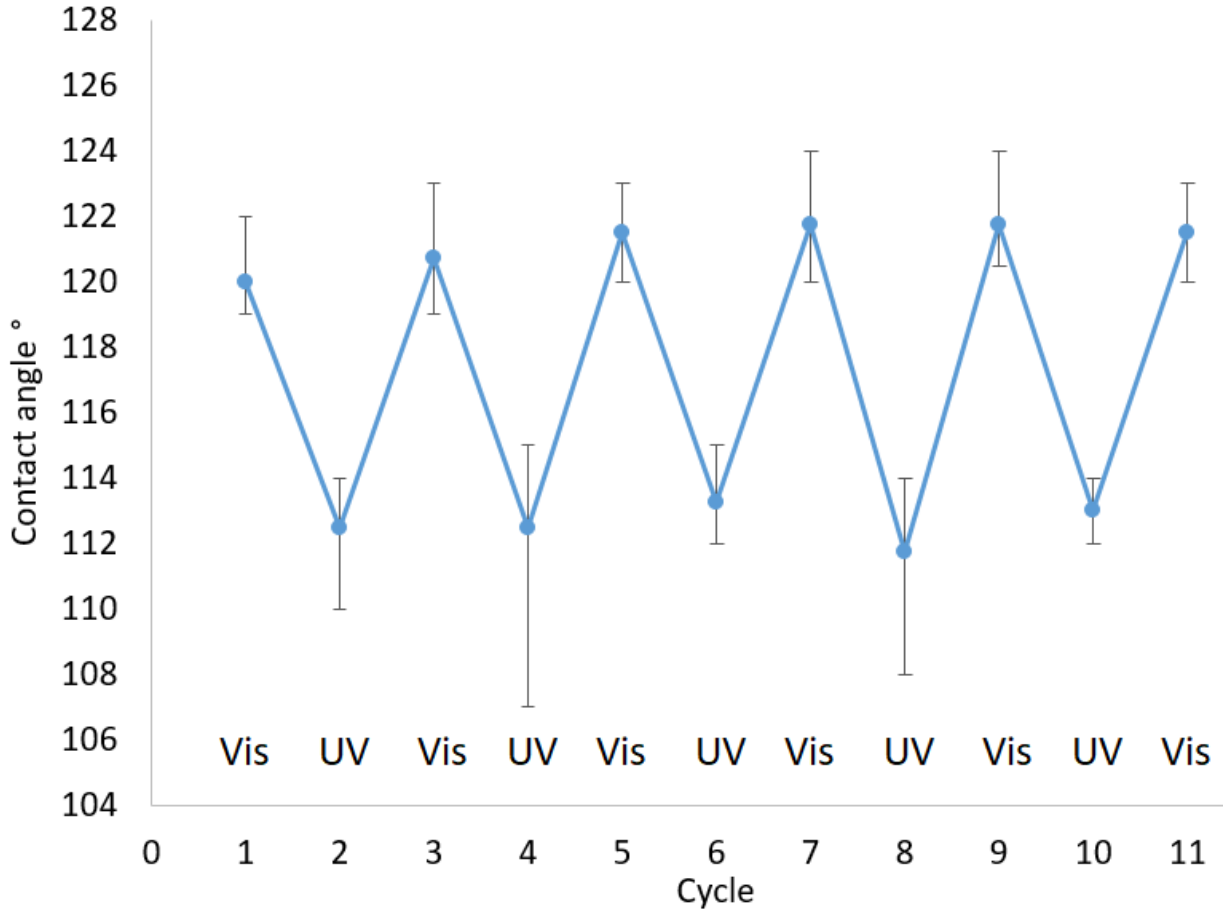

Figure VI.23. WCA changes of the di-Azo-Cel fabric over 5 cycles of UV/visible light irradiations. The plotted WCA values are the mean values of 4 sets of the measurements using 4 different pieces of the di-Azo-Cel fabric, and the error bars represent their maximum and minimum values.

The WCA plot of di-Azo-Cel textile shows a more uniform change in wettability upon UV and visible light irradiations, probably because of the fact that the surface of the di-Azo-Cel fabric was smoother than the surface of Azo-Cel textile. The WCA of di-Azo-Cel was reversibly changed

by UV and visible light irradiations, with an averaged angle change of 8.6°, indicating that even a reduction in the molar ratio of Azo side groups in di-Azo-Cel compared to Azo-Cel, did not dampen the wettability properties and the AB moiety in the di-Azo-Cel fabric still managed to induce the changes of its surface wettability.

UV-induced photo-actuation analysis of the di-Azo-Cel fabrics was conducted in accordance with the same protocol as Azo-Cel fabrics (see chapter V.3). Similarly to Azo-Cel, a UV-driven asymmetric bending deformation was observed toward the light source for di-Azo-Cel (Figure VI.24).

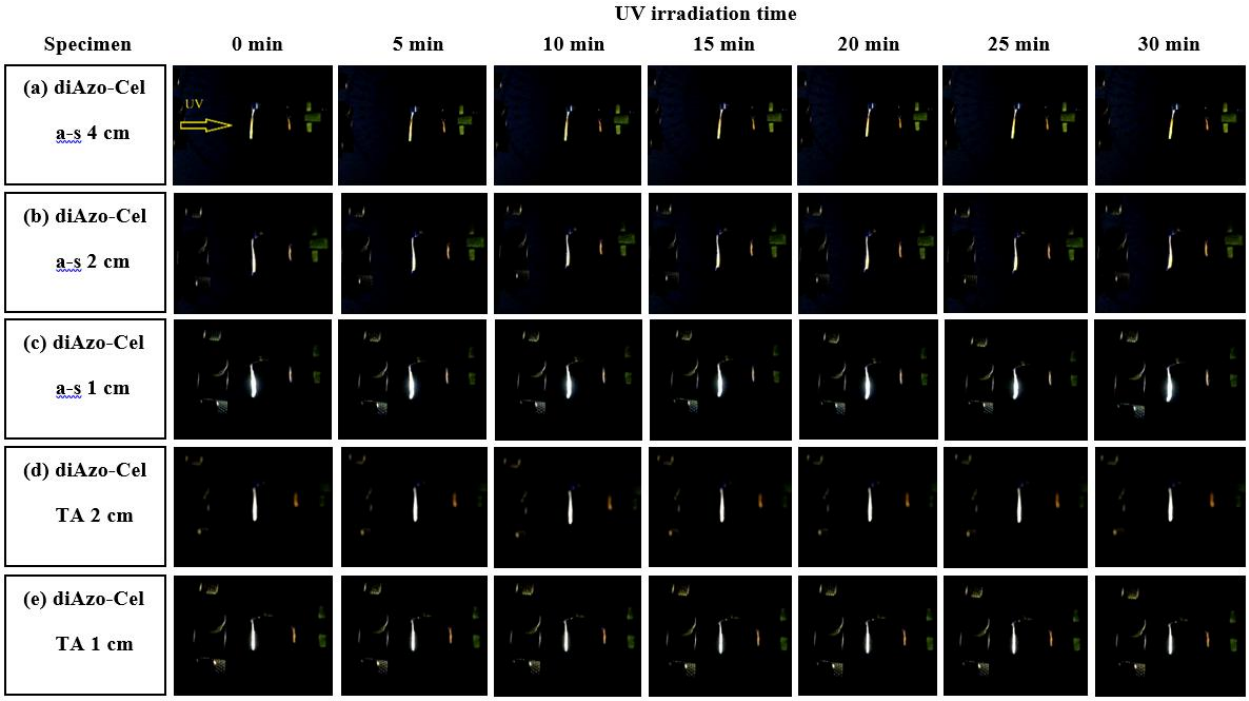

Figure VI.24. Series of pictures of as-spun and thermally annealed di-Azo-Cel fabrics irradiated by UV over time of the irradiation: a) di-Azo-Cel placed at 4 cm away (I = 25 mW/cm^2), b) di-Azo-Cel placed at 2 cm away (45 mW/cm^2), c) di-Azo-Cel placed at 1 cm away (60 mW/cm^2), d) Thermally annealed di-Azo-Cel placed at 2 cm away (45 mW/cm^2), and e) Thermally annealed di-Azo-Cel placed at 1 cm away (60 mW/cm^2) from the UV light source (at the left-side in the pictures).

It was already discussed that the CA fabric did not show bending toward the source of UV light, proving that the movements of Azo-Cel were induced by the photo-isomerization of the AB moiety in the Azo-Cel. Figure VI.24 a-e present bending behaviors over time of 5 pieces of the as-spun (a-s) and thermally annealed (TA) di-Azo-Cel fabrics placed at 4 cm (25 mW/cm^2), 2 cm (45 mW/cm^2), and 1 cm (60 mW/cm^2) away from the UV light source. The di-Azo-Cel fabric barely bent toward the UV irradiation from a longer distance of 4 cm, as presented in Figure VI.24 a, whereas the bending was visible at a medium distance of 2 cm, illustrated in Figure VI.24 b. The same explanation as the case of Azo-Cel stands true: The lower light intensity (25 mW/cm^2) from the longer distance is not sufficient to photo-isomerize the AB moiety in the surface region of the di-Azo-Cel fabric from the *trans* to the *cis* isomers, which must be the driving force of the asymmetric bending. Furthermore, the UV irradiation from a shorter distance (1 cm) clearly induced an asymmetric bending of the di-Azo-Cel fabric toward the light source. In addition, it appears that the bending behavior of di-Azo-Cel has dampened compared to Azo-Cel, probably due to the reduced amount of AB pendants that undergo *trans* to *cis* photo-isomerization once irradiated by UV light and induce anisotropic bending. Interestingly, thermal annealing of the di-Azo-Cel did not favor the photo-actuation (Figure VI.24 d,e) It seems that thermal annealing may have crystallized the polymer backbone of the fibers, thus rendering them more rigid and therefore more difficult to react to light stimuli. As stated by Zhuang and colleagues in 2015 [171], thermal annealing incites a rearrangement of the molecular structure of the polymer matrix, thus the crystal region of the annealed polymer matrix increases.

Regarding the tensile properties of the annealed Azo-Cel and di-Azo-Cel fabrics, it was impossible to measure their tensile strength due to the fact that both products became so rigid that

would break inside the tensile holders before starting measurements, but were flexible enough to be tested for photo-responsivity properties.

VI.4. Conclusion

Regioselectively Azo-functionalized cellulose was synthesized through protection of C6 of AGU by tritylation, then esterifying the C2 and C3 regions, then eventually deprotecting the C6 regions to obtain di-Azo-Cel. A self-standing di-Azo-Cel fabric was produced via electrospinning of its 10 wt% solution in a system of DCM/DMF 3/1 v/v. di-Azo-Cel shows no change in WCA of the new product compared to Azo-Cel, yet the photo-responsive bending is heavily impacted and dampened due to a decrease in molar ratio of functionalized Azo side groups.

It appears that regioselectively Azo-functionalized cellulose demonstrates different thermal/mechanical/photo-responsive behavior compared to the conventional Azo-Cel (DS ≈ 2.83). The change in the molarity of Azo side groups between the two products had a direct effect in those behaviors. It should be noted that although the photo-responsive bending of di-Azo-Cel was slower and less intense that Azo-Cel, the wettability measurements demonstrated no change in terms of WCA changes that are derived from a collective *cis/trans* photo-isomerization of the Azo moieties. Therefore further measurements are required to have a clearer understanding of this process.

Chapter VII : General Conclusion

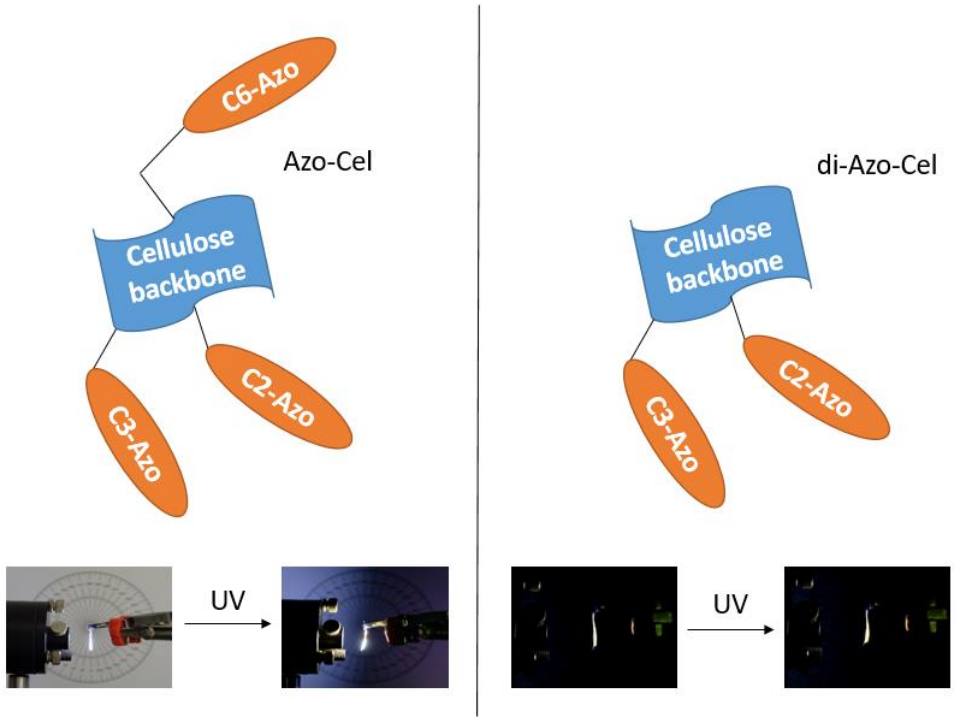

Microcrystalline cellulose was functionalized with Azo group with a high DS (DS_{azo} = 2.83) to obtain Azo-Cel. The chemical characteristics of the product were verified by ATR-FTIR, NMR, UV-Vis, TGA, and DSC. The electrospinning of Azo-Cel was studied in various solvent systems, notably in mixtures of DCM/DMF and acetone/DMAc, with different solvent ratios and polymer concentrations. It was found that regardless of the solvent system, an increase of polymer concentration, as well as the ratio of volatile solvent, favors the production of micro/nanofibers and eliminates beads. The self-standing Azo-Cel fabric was produced after stabilizing the electrospinning process by favoring a mixed solvent system consisting of the highly volatile poor solvent: acetone, and the low-volatile good solvent: DMAc. The self-standing fabric was consisted of uniaxially aligned microfibers that were gathered on a rotary drum collector. The Azo-Cel fabric demonstrated clear photo-responsive properties, *i.e.* (I) the light-driven wettability changes supported by the photo-isomerization of the less polar *trans* azo isomers to the more polar *cis* azo isomers under UV light and vice versa under visible light, and (II) the UV-induced actuation behavior observed as the asymmetric bending deformation toward a light source.

There are different methods to improve the photo-responsive response of polymer-based photo-actuators. Annealing and regioselective functionalization of the photo-responsive chromophores in the polymer are considered effective methods for the improvement of photo-responsive behavior [172–175]. In our case study we have found that annealing the polymer not only orders the azo side groups−which is desired to have faster response to light stimuli−but it also orders the polymer backbone as well, which in hindsight dampens the photo-responsivity. Hence, the higher rigidity of the thermally annealed Azo-Cel and negligible movement toward UV light source.

Regioselctively-functionalized di-Azo-Cel was produced by the means of the C6-protection, *i.e.* tritylation of the primary alcohol group of glucose units of cellulose. The remaining free C2 and C3 were then esterified and after this step, the primary hydroxyl groups were deprotected. The obtained product was then characterized by the following methods: ATR-FTIR, NMR, UV-Vis, TGA, and DSC. It was found that this product had free hydroxyl groups and a reduced amount of AB side groups (DS_{azo} = 1.66 for di-Azo-Cel compared to DS_{azo} = 2.83 for Azo-Cel). In terms of mechanical resistance to the stretching force (tensile properties), this product shows more strain and deformation, yet lower force required to break the textile. This phenomenon can be due to two factors: (I) the existence of free –OH groups in the backbone polymer chains that are able to form hydrogen bonds, and (II) reduced steric hindrance caused by the neighboring AB side groups, hence making the polymer chains flow upon each other more easily up to a point where less force (=less stress) is required to break the more elongated textile (more strain).

Reduced amount of AB side groups however, did not appear to dampen the wettability of the product, compared to that of Azo-Cel. As the product has a smoother surface, the changes of WCA are more homogenous between *trans* (under Vis) and *cis* (under UV) states.

The di-Azo-Cel demonstrated weaker response to UV light stimulus under the conditions tired in this study. Compared to Azo-Cel, this product showed about half UV-stimulated movements (in terms of its varied angle, observed *via* the angle sheet placed behind the textiles during the measurements) towards the light source because of the reduced amount of AB side groups, and possibly the presence of –OH groups that form intramolecular hydrogen bonds.

The entirety of this thesis study revolved around the fact that the AB groups that react to light stimuli are located on the side groups and are not a part of the polymer backbone. Numerous studies report much quicker and higher photoresponsivity to UV and visible light stimuli whenever

the chromophore act as a link inside the backbone of the product [27,28,136]. Interestingly, our study differs from its pioneering works because of several reasons, such as the fact that the very first electrospun polysaccharide-based photo-actuator was fabricated during this study, the light source is not optimized and can be improved, and other forms of regioselective-functionalized Azo-Cel could be produced to study their effects.

For the continuity of this study, another regioselectively-functionalized Azo-Cel can be produced where the C6 regions are esterified with AB groups and the C2 and C3 regions are free to form hydrogen bonds. The electrospinnability and photo-responsivity properties may differ from the present case, as well as the anticipated thermal and mechanical behaviors. Another possibility would be to produce polymers where the monomers are connected to one another *via* Azo pendants, displacing the chromophores that react to light stimuli from the side groups to the main chain of the polymer in order to possibly intensify the photo-actuation. Apart from cellulose, other starting materials such as alginate, amylose, etc., could be used to study their respective impacts on the thermal/mechanical/photo-responsive behaviors.

At last, it is imperative to mention the scientific accomplishments and milestones during this work of PhD thesis:

1) The author has validated 123 hours of various courses throughout this PhD thesis, naming Leadership et travail en équipe, Mobilisation vers l'emploi, Développer une posture de leader, Nanocellulose Winterschool 2019, Synchrotron X-ray and neutron applied to nano-electronics, *etc*.
2) During this thesis, the author has supervised an overall of 28 hours of lab courses in kinetics and thermodynamics of chemical reactions for bachelor students of Université Grenoble Alpes, (UGA).

3) The author has helped with the organization of the stand of Labex-Arcane during 30th anniversary of Fête de la Science at Minatec of Grenoble, and co-supervised two Master's interns during his thesis, whose results of works were published in ACS Macro Letters in 2021 [19].
4) The results of the first half of this work were published in Macromolecular Rapid Communication journal in March 2022 [50].
5) The author of this thesis has presented the results of this work as oral and poster presentations in several conferences, naming GFP2021 and DumBiop2022.
6) The author has been the winner of Concours Vidéo du Labex arcane, during which a short movie was prepared to present the current work revolving around electrospinning [176].
7) Furthermore, the author has been the representative of non-permanents at CERMAV-CNRS, as well as the vice-treasurer of Glob'Alps non-profit organization during his thesis, which is an assembly of the PhD candidates of UGA doctoral college that aims to assist PhD candidates in their personal and professional lives.

Appendix

During this study, several measurements were conducted to characterize some specific behaviors of Azo-Cel and trityl cellulose. For example, spin-coating of Azo-Cel was carried out to distinguish the WCA behavior of an Azo-Cel spin-coated film from textile. In addition, perpropionylation of trityl cellulose was carried out in order to measure the DS_{trityl} from the ^{1}H NMR spectrum, but this attempt was fruitless as it was unable to produce reliable results. That is why this section discusses the procedure and results of these measurements.

A.1. Spin-coating of Azo-Cel

According to the literature, for the spin coating of azo-containing polymers, a variety of 5-15 mg/mL solutions would be enough to study the effect of WCA [177,178]. A final thickness of at least 300 nm is required for the tests [179]. For the purpose of this study, two solutions of 5 mg/mL and 50 mg/mL Azo-Cel in dichloromethane (DCM) were prepared; the former was labelled S-1-135-1 and the latter S-1-135-2. A Tournette SPIN150 spin-coater was used to prepare thin films of Azo-Cel on a silicon substrate by spinning at 2000 rpm for 60 seconds.

Once thin film from each solution was prepared (Sp-135-1 and Sp-135-2 respectively), their thickness were measured by Filmetrics F20-UV apparatus, noting 35.9 nm for Sp-135-1 and 1157.3 ± 32.5 nm for Sp-135-2. WCAs of these two specimens were measured after each sample went through one full cycle of visible-UV-visible light irradiation. Firstly, WCA of each specimen was measured under visible light and before UV irradiation, the specimens were then placed inside the UV lamp at 60 mW/cm^2 for 15 minutes and again their WCAs were measured in a dark room. To end the cycle, the specimens were exposed to visible white light of the room for 30 minutes

and again their WCAs were measured. The data presented in table 2 shows a significant difference of WCA (from 30 to 40 degrees) of these thin films and those of self-standing micro fiber-mats of Azo-Cel (generally around 120° at visible light and 110° after UV irradiation).

According to Paik et al., 2007 [178], thins films of AB-functionalized co-polymers, where AB acts as a junction group between two polymers, could demonstrate an angle of 110 to 125 degrees under visible light, and an angle of 105 to 120 degrees after UV irradiation. However, Abrakhi et al. in 2013 [180] reported their results on the matter of AB acrylate-co-fluorinated acrylate, where they studied the water and diiodomethane contact angle of their polymers and how it changed when the molar proportion of AB side groups to fluorinated side groups changed. They argue that generally the contact angle (under visible light) decreased with the increase of the molar proportion of azo pendant to fluorinated side group.

Table A.1. WCA values (°) of silicon substrate under the visible light, alongside Sp-135-1 and Sp-135-2 after going through a full cycle of visible-UV-visible light irradiation.

Cycle / Specimen	**Before UV**	**UV**	**Vis**
Silicon substrate	56	-	-
Sp-135-1	87	87	88
Sp-135-2	81	83	88

As Figure 3 illustrates, there is a major difference of 25 to 31 degrees between the WCA of silicon and thin films, indicating that the water droplets are being superimposed on the surface of thin films, and not silicon substrate. Furthermore, each specimen reacted differently to the exposure of UV light. For Sp-135-1, having a finer thickness prevented the film from showing any

significant change of angle. In the case of Sp-135-2 however, a contact angle of 81° was noted before UV irradiation. After UV irradiation for 15 minutes, the angle increased to 83° whilst at the end of the cycle where the thin film has already been exposed for 30 minutes to visible light, an angle of 88° is recorded.

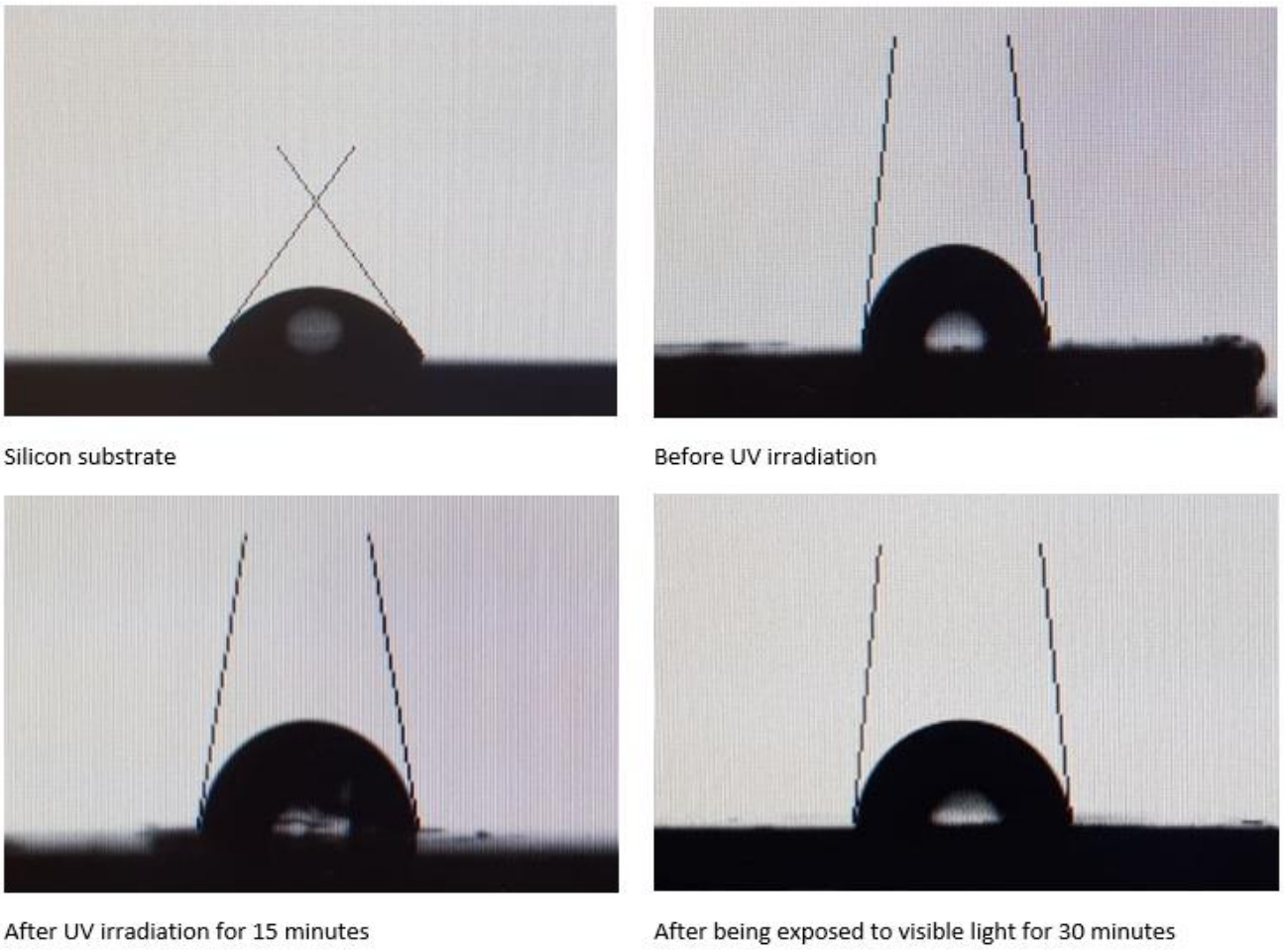

Figure A.1. Shapes and contact angles of water drop for Sp-135-2 and silicon substrate.

Moreover, the surface of Sp-135-2 was not homogenous because of the high concentration of the solution. Perhaps the concentration should be somewhere in between 5 and 50 mg mL^{-1}. For

having thicker film, the polymer can be applied to the silicon substrate several times to keep the homogeneity.

A.2. Determination of DS_{trityl} of 6OTC by Perpropionylation

One of the means to calculate the DS of the functional groups on cellulose-esters and cellulose-ethers is perpropionylation of the product in a system of propionic anhydride/pyridine and DMAP as catalyst and then calculate the DS by comparing the integrals of the H bands of the propionyl groups to the H bands of anhydroglucose unit (AGU) on ^{1}H NMR spectroscopy [181,182].

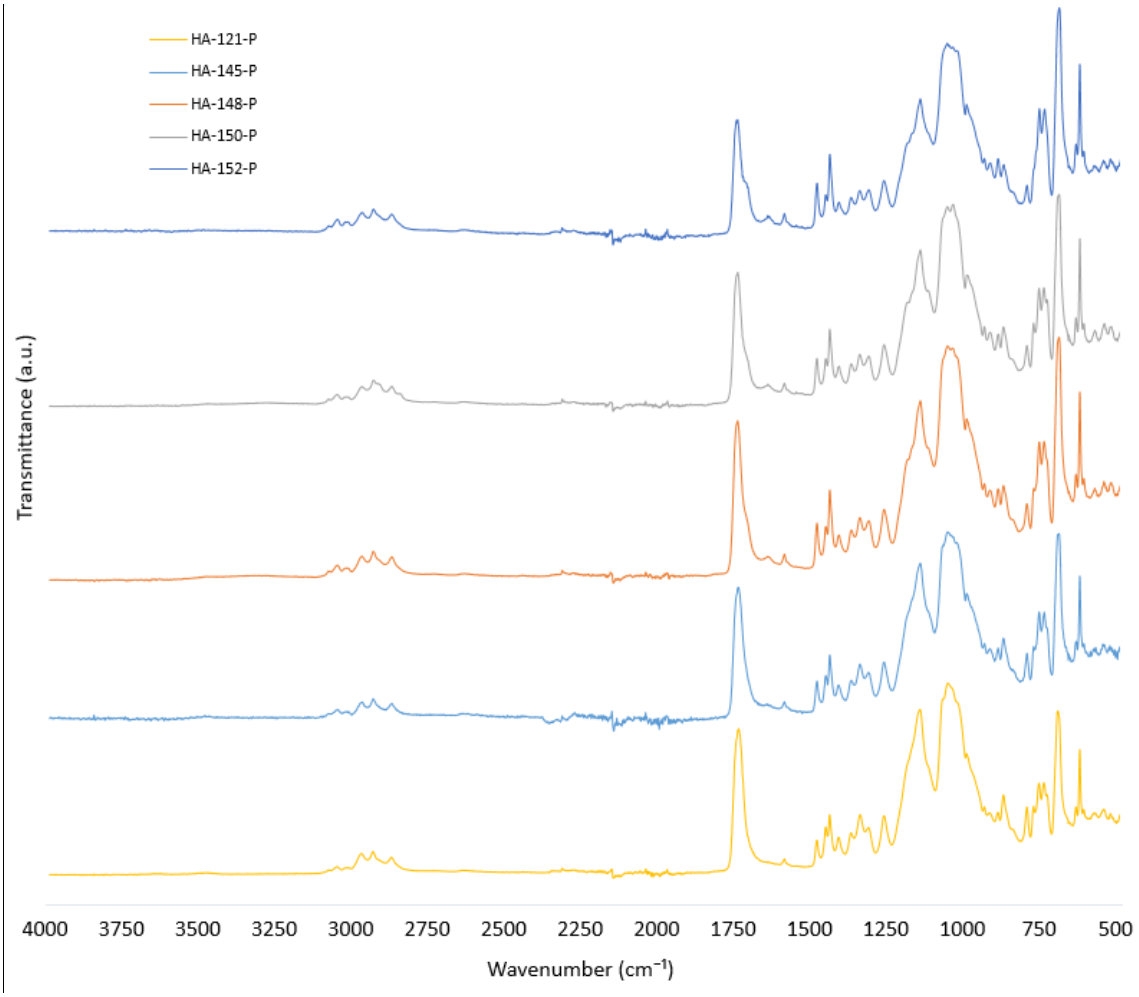

Figure A.2. IR spectra of HA-121-P, 145-P, 148-P, 150-P, and 152-P.

For our purpose we followed the procedure reported by Gräbner et al., 2002 [182] for the preparation of peracylated trityl cellulose and determination of DS by 1H NMR spectroscopy. Prior to perpropionylation, each product was prepared with different proportions of reaction components to study their effects on the tritylation. Table A.2 presents the details for each product.

Table A.2. Reaction parameters of the tritylated products.

Parameter / Product	Tr-Cl (mol equiv. per 1 mol AGU)	Reaction moiety	Pyridine (mol equiv. per 1 mol AGU)	Time of reaction (h)	Reaction's temperature (°C)
HA-1-121	6	[AMIM]Cl	10	6	80
HA-1-145	6	[BMIM]Cl	10	6	80
HA-1-148	6	[BMIM]Cl	10	3	80
HA-1-150	4	[BMIM]Cl	10	6	80
HA-1-152	6	[BMIM]Cl	10	6	100

0.3 g of each of the 5 trityl-cellulose products, *i.e.* HA-1-121 (synthesized in [AMIM]Cl), HA-1-145, HA-1-148, HA-1-150, and HA-1-152 (prepared in [BMIM]Cl), was added to a system of 6 mL propionic anhydride and 6 mL pyridine, with 50 mg of DMAP as catalyst. The reaction was carried out at 80 °C for 24, after which the mixture was precipitated into 50 mL of ethanol (EtOH) and filtered. For purification, each product was dissolved in chloroform and re-precipitated in EtOH and refiltered. Propionylated trityl-cellulose products were labelled HA-121-P, HA-145-P, HA-148-P, HA-150-P, and HA-152-P respectively. Figure 3 describes the IR spectra of these products. Along with the trityl bands at 3091, 3057, 3000, 1596, 1491, 1449, 601, and 635 cm^{-1} it is clear that new peaks have emerged that belong to propionyl groups. The sharp absorbance band at 1748 cm^{-1} belongs to the –C=O of ester group, while the peaks at 2977, 2941, and 2880 cm^{-1}

belong to the –CH of propionic. Furthermore, the absence of –OH stretching bands at 3464 cm^{-1} suggests the propionylation reactions were complete.

The ^{1}H NMR spectroscopy of all the five products were carried out in dichloromethane-d_2 (99.3% deuterium), by scanning the solution 128 times at room temperature. According to Erdmenger et al., 2007 [151], the broad band between 7.86 and 6.86 ppm stands for protons' chemical shifts of trityl, while the band between 5.24 and 2.65 ppm represents the protons' chemical shift of AGU. The chemical shift of $–CH_2$ of propionate can be observed between 2.49 to 1.49 ppm, alongside the band between 1.23 and 0.61 ppm, which represents the $–CH_3$ chemical shift of propionate. Figure 4 to 8 represent the ^{1}H NMR spectra of HA-121-p, 145-P, 148-P, 150-P, and 152-P respectively.

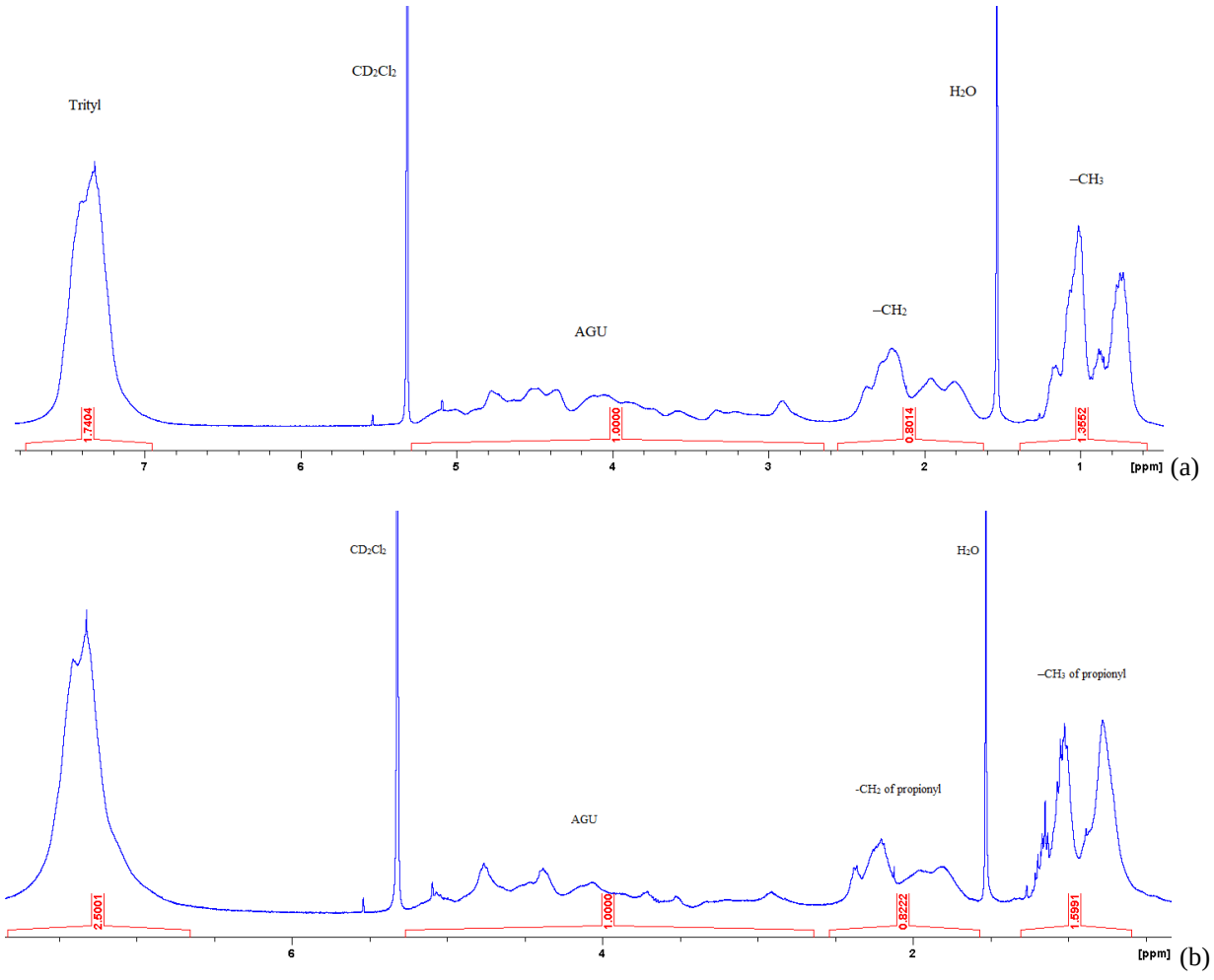

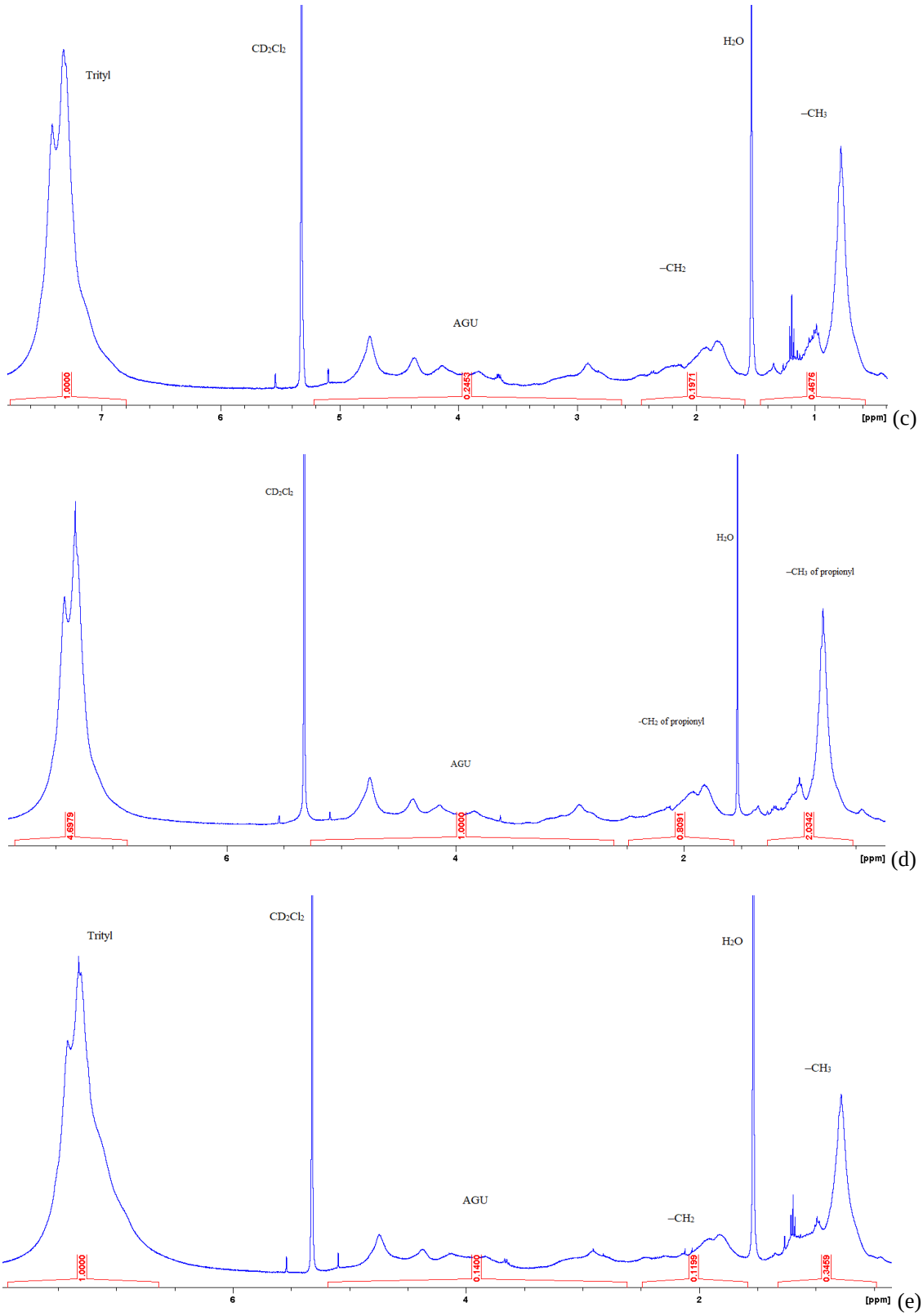

Figure A.3. [1]H NMR spectra of a) HA-121-P, b) HA-145-P, c) HA-148-P, d) HA-150-P, and e) HA-152-P.

The DS of trityl groups on the original trityl cellulose for each propionylated product can be calculated from ^{1}H NMR spectra by the following equation:

$$DS_{Trityl} = 3 - \frac{7 \times I_{Propyl}}{3 \times I_{H,AGU}}$$

Where I_{Propyl} is the peak integral of methyl protons of propionyl moieties and $I_{H,AGU}$ represents the peak integral of all protons of AGU [181–183]. The results obtained from perpropionylation differ from other methods of DS determination, *i.e.* ATR-FTIR and EA. Hence, EA of the products of the next steps were carried out to ensure the exactitude of the results.

References

(1) Li, J.; Zhou, X.; Liu, Z. Recent Advances in Photoactuators and Their Applications in Intelligent Bionic Movements. *Advanced Optical Materials* **2020**, *8* (18), 2000886. https://doi.org/10.1002/adom.202000886.

(2) Bhardwaj, N.; Kundu, S. C. Electrospinning: A Fascinating Fiber Fabrication Technique. *Biotechnology Advances* **2010**, *28* (3), 325–347. https://doi.org/10.1016/j.biotechadv.2010.01.004.

(3) Greiner, A.; Wendorff, J. H. Electrospinning: A Fascinating Method for the Preparation of Ultrathin Fibers. *Angewandte Chemie International Edition* **2007**, *46* (30), 5670–5703. https://doi.org/10.1002/anie.200604646.

(4) Li, D.; Xia, Y. Electrospinning of Nanofibers: Reinventing the Wheel? *Advanced Materials* **2004**, *16* (14), 1151–1170. https://doi.org/10.1002/adma.200400719.

(5) Huang, Z.-M.; Zhang, Y.-Z.; Kotaki, M.; Ramakrishna, S. A Review on Polymer Nanofibers by Electrospinning and Their Applications in Nanocomposites. *Composites Science and Technology* **2003**, *63* (15), 2223–2253. https://doi.org/10.1016/S0266-3538(03)00178-7.

(6) Isaac, B.; Taylor, R. M.; Reifsnider, K. Mechanical and Dielectric Properties of Aligned Electrospun Fibers. *Fibers* **2021**, *9* (1), 4. https://doi.org/10.3390/fib9010004.

(7) Lee, J.; Deng, Y. Increased Mechanical Properties of Aligned and Isotropic Electrospun PVA Nanofiber Webs by Cellulose Nanowhisker Reinforcement. *Macromolecular Research* **2012**, *20* (1), 76–83. https://doi.org/10.1007/s13233-012-0008-3.

(8) Shang, S.; Yang, F.; Cheng, X.; Walboomers, X.; Jansen, J. The Effect of Electrospun Fibre Alignment on the Behaviour of Rat Periodontal Ligament Cells. *European Cells and Materials* **2010**, *19*, 180–192. https://doi.org/10.22203/eCM.v019a18.

(9) Schiffman, J. D.; Schauer, C. L. A Review: Electrospinning of Biopolymer Nanofibers and Their Applications. *Polymer Reviews* **2008**, *48* (2), 317–352. https://doi.org/10.1080/15583720802022182.

(10) Sridhar, R.; Lakshminarayanan, R.; Madhaiyan, K.; Amutha Barathi, V.; Lim, K. H. C.; Ramakrishna, S. Electrosprayed Nanoparticles and Electrospun Nanofibers Based on Natural Materials: Applications in Tissue Regeneration, Drug Delivery and Pharmaceuticals. *Chemical Society Reviews* **2015**, *44* (3), 790–814. https://doi.org/10.1039/C4CS00226A.

(11) Padil, V. V. T.; Cheong, J. Y.; Kp, A.; Makvandi, P.; Zare, E. N.; Torres-Mendieta, R.; Wacławek, S.; Černík, M.; Kim, I.-D.; Varma, R. S. Electrospun Fibers Based on Carbohydrate Gum Polymers and

Their Multifaceted Applications. *Carbohydrate Polymers* **2020**, *247*, 116705. https://doi.org/10.1016/j.carbpol.2020.116705.

(12) Memic, A.; Abdullah, T.; Mohammed, H. S.; Navare, K. J.; Colombani, T.; Bencherif, S. A. Latest Progress in Electrospun Nanofibers for Wound Healing Applications. *ACS Applied Bio Materials* **2019**. https://doi.org/10.1021/acsabm.8b00637.

(13) Poshina, D.; Otsuka, I. Electrospun Polysaccharidic Textiles for Biomedical Applications. *Textiles* **2021**, *1* (2), 152–169. https://doi.org/10.3390/textiles1020007.

(14) Zhu, Q.; Liu, S.; Sun, J.; Liu, J.; Kirubaharan, C. J.; Chen, H.; Xu, W.; Wang, Q. Stimuli-Responsive Cellulose Nanomaterials for Smart Applications. *Carbohydrate Polymers* **2020**, *235*, 115933. https://doi.org/10.1016/j.carbpol.2020.115933.

(15) Toncheva, A.; Khelifa, F.; Paint, Y.; Voué, M.; Lambert, P.; Dubois, P.; Raquez, J.-M. Fast IR-Actuated Shape-Memory Polymers Using in Situ Silver Nanoparticle-Grafted Cellulose Nanocrystals. *ACS Applied Materials and Interfaces* **2018**, *10* (35), 29933–29942. https://doi.org/10.1021/acsami.8b10159.

(16) Kim, J.; Yun, S.; Ounaies, Z. Discovery of Cellulose as a Smart Material. *Macromolecules* **2006**, *39* (12), 4202–4206. https://doi.org/10.1021/ma060261e.

(17) Qiu, X.; Hu, S. "Smart" Materials Based on Cellulose: A Review of the Preparations, Properties, and Applications. *Materials* **2013**, *6* (3), 738–781. https://doi.org/10.3390/ma6030738.

(18) Sehaqui, H.; Morimune, S.; Nishino, T.; Berglund, L. A. Stretchable and Strong Cellulose Nanopaper Structures Based on Polymer-Coated Nanofiber Networks: An Alternative to Nonwoven Porous Membranes from Electrospinning. *Biomacromolecules* **2012**, *13* (11), 3661–3667. https://doi.org/10.1021/bm301105s.

(19) Otsuka, I.; Pandey, K.; Ahmadi-Nohadani, H.; Nono-Tagne, S. Electrospun Cellulosic Membranes toward Efficient Chiral Resolutions via Enantioselective Permeation. *ACS Macro Letters* **2021**, *10* (7), 921–925. https://doi.org/10.1021/acsmacrolett.1c00349.

(20) Otsuka, I.; Barrett, C. J. Electrospinning of Photo-Responsive Azo-Cellulose: Towards Smart Fibrous Materials. *Cellulose* **2019**, *26* (11), 6903–6915. https://doi.org/10.1007/s10570-019-02585-9.

(21) Bertrand, O.; Gohy, J.-F. Photo-Responsive Polymers: Synthesis and Applications. *Polymer Chemistry* **2017**, *8* (1), 52–73. https://doi.org/10.1039/C6PY01082B.

(22) Ercole, F.; P. Davis, T.; A. Evans, R. Photo-Responsive Systems and Biomaterials: Photochromic Polymers , Light-Triggered Self-Assembly , Surface Modification, Fluorescence Modulation and Beyond. *Polymer Chemistry* **2010**, *1* (1), 37–54. https://doi.org/10.1039/B9PY00300B.

(23) Du, W.; Liu, X.; Liu, L.; Lam, J. W. Y.; Tang, B. Z. Photoresponsive Polymers with Aggregation-Induced Emission. *ACS Applied Polymer Materials* **2021**, *3* (5), 2290–2309. https://doi.org/10.1021/acsapm.1c00182.

(24) Yu, H. Recent Advances in Photoresponsive Liquid-Crystalline Polymers Containing Azobenzene Chromophores. *Journal of Materials Chemistry C* **2014**, *2* (17), 3047–3054. https://doi.org/10.1039/C3TC31991A.

(25) Bushuyev, O. S.; Aizawa, M.; Shishido, A.; Barrett, C. J. Shape-Shifting Azo Dye Polymers: Towards Sunlight-Driven Molecular Devices. *Macromolecular Rapid Communications* **2018**, *39* (1), 1700253. https://doi.org/10.1002/marc.201700253.

(26) Pang, X.; Lv, J.; Zhu, C.; Qin, L.; Yu, Y. Photodeformable Azobenzene-Containing Liquid Crystal Polymers and Soft Actuators. *Advanced Materials* **2019**, *31* (52), 1904224. https://doi.org/10.1002/adma.201904224.

(27) Ikeda, T.; Nakano, M.; Yu, Y.; Tsutsumi, O.; Kanazawa, A. Anisotropic Bending and Unbending Behavior of Azobenzene Liquid-Crystalline Gels by Light Exposure. *Advanced Materials* **2003**, *15* (3), 201–205. https://doi.org/10.1002/adma.200390045.

(28) Yu, Y.; Nakano, M.; Ikeda, T. Directed Bending of a Polymer Film by Light. *Nature* **2003**, *425* (6954), 145–145. https://doi.org/10.1038/425145a.

(29) Finkelmann, H.; Nishikawa, E.; Pereira, G. G.; Warner, M. A New Opto-Mechanical Effect in Solids. *Physical Review Letters* **2001**, *87* (1), 015501. https://doi.org/10.1103/PhysRevLett.87.015501.

(30) Van Oosten, C. L.; Bastiaansen, C. W. M.; Broer, D. J. Printed Artificial Cilia from Liquid-Crystal Network Actuators Modularly Driven by Light. *Nature Materials* **2009**, *8* (8), 677–682. https://doi.org/10.1038/nmat2487.

(31) Iamsaard, S.; Aßhoff, S. J.; Matt, B.; Kudernac, T.; Cornelissen, J. J. L. M.; Fletcher, S. P.; Katsonis, N. Conversion of Light into Macroscopic Helical Motion. *Nature Chemistry* **2014**, *6* (3), 229–235. https://doi.org/10.1038/nchem.1859.

(32) White, T. J.; Tabiryan, N. V.; Serak, S. V.; Hrozhyk, U. A.; Tondiglia, V. P.; Koerner, H.; Vaia, R. A.; Bunning, T. J. A High Frequency Photodriven Polymer Oscillator. *Soft Matterials* **2008**, *4* (9), 1796. https://doi.org/10.1039/b805434g.

(33) Pilz da Cunha, M.; Debije, M. G.; Schenning, A. P. H. J. Bioinspired Light-Driven Soft Robots Based on Liquid Crystal Polymers. *Chemical Society Reviews* **2020**, *49* (18), 6568–6578. https://doi.org/10.1039/D0CS00363H.

(34) Won, S.; Kim, S.; Park, J. E.; Jeon, J.; Wie, J. J. On-Demand Orbital Maneuver of Multiple Soft Robots via Hierarchical Magnetomotility. *Nature Communications* **2019**, *10* (1), 4751. https://doi.org/10.1038/s41467-019-12679-4.

(35) Zhang, Q. M.; Serpe, M. J. Stimuli-Responsive Polymers for Actuation. *ChemPhysChem* **2017**, *18* (11), 1451–1465. https://doi.org/10.1002/cphc.201601187.

(36) Timothy J. White. Photomechanical Effects in Liquid Crystalline Polymer Networks and Elastomers. *Journal of polymer science* **2018**, *56* (9), 695–705. https://doi.org/10.1002/polb.24576.

(37) Rešetič, A.; Milavec, J.; Zupančič, B.; Domenici, V.; Zalar, B. Polymer-Dispersed Liquid Crystal Elastomers. *Nature Communications* **2016**, *7* (1), 13140. https://doi.org/10.1038/ncomms13140.

(38) Stoychev, G.; Kirillova, A.; Ionov, L. Light-Responsive Shape-Changing Polymers. *Advanced Optical Materials* **2019**, *7* (16), 1900067. https://doi.org/10.1002/adom.201900067.

(39) Shibaev, V. P.; Lam, L. *Liquid Crystalline and Mesomorphic Polymers*; Springer Science & Business Media, 2012.

(40) Donald, A. M.; Windle, A. H.; Hanna, S. *Liquid Crystalline Polymers*; Cambridge University Press, 2006.

(41) Collyer, A. A. *Liquid Crystal Polymers: From Structures to Applications*; Springer Science & Business Media, 2012.

(42) Acierno, D.; Collyer, A. A. *Rheology and Processing of Liquid Crystal Polymers*; Springer Science & Business Media, 2013.

(43) Shibaev, V. *Polymers as Electrooptical and Photooptical Active Media*; Springer Science & Business Media, 2012.

(44) Tschierske, C. Fluorinated Liquid Crystals: Design of Soft Nanostructures and Increased Complexity of Self-Assembly by Perfluorinated Segments. In *Liquid Crystals: Materials Design and Self-assembly*; Tschierske, C., Ed.; Topics in Current Chemistry; Springer: Berlin, Heidelberg, 2012; pp 1–108. https://doi.org/10.1007/128_2011_267.

(45) Thesis Manuscript: Pauline PACQUET. INSA Lyon. https://www.insa-lyon.fr/fr/evenement/soutenance-these-pauline-pacquet (accessed 2022-09-26).

(46) Bouas-Laurent, H.; Dürr, H. Organic Photochromism (IUPAC Technical Report). *Pure and Applied Chemistry* **2001**, *73* (4), 639–665. https://doi.org/10.1351/pac200173040639.

(47) Pieroni, O.; Fissi, A.; Angelini, N.; Lenci, F. Photoresponsive Polypeptides. *Accounts of Chemical Research* **2001**, *34* (1), 9–17. https://doi.org/10.1021/ar990141+.

(48) Zhuang, Y.; Ren, X.; Che, X.; Liu, S.; Huang, W.; Zhao, Q. Organic Photoresponsive Materials for Information Storage: A Review. *Advanced Photonics* **2020**, *3* (1), 014001. https://doi.org/10.1117/1.AP.3.1.014001.

(49) Welleman, I. M.; Hoorens, M. W. H.; Feringa, B. L.; Boersma, H. H.; Szymański, W. Photoresponsive Molecular Tools for Emerging Applications of Light in Medicine. *Chemical Science* **2020**, *11* (43), 11672–11691. https://doi.org/10.1039/D0SC04187D.

(50) Ahmadi-Nohadani, H.; Nono-Tagne, S.; Barrett, C. J.; Otsuka, I. Electrospun Azo-Cellulose Fabric: A Smart Polysaccharidic Photo-Actuator. *Macromolecular Rapid Communications* **2022**, *43* (9), 2200063. https://doi.org/10.1002/marc.202200063.

(51) Barrett, C. J.; Mamiya, J.; Yager, K. G.; Ikeda, T. Photo-Mechanical Effects in Azobenzene-Containing Soft Materials. *Soft Matterials* **2007**, *3* (10), 1249. https://doi.org/10.1039/b705619b.

(52) Mann, G. Encyclopedia of Polymer Science and Engineering. 2nd Edition. Vol. 1: A to Amorphous Polymers, Vol. 2: Anionic Polymerization to Cationic Polymerization. Hg. von HERMAN F. MARK NORBERT M. BIKALES CHARLES G. OVERBERGER GEORG MENGES New York/Chichester/Brisbane/Toronto/Singapore: A Wiley-Interscience Publication, John Wiley & Sons, 1985. LXII, 843 S. Und XXIV, 814 S. Vol. 1: ISBN 0-471-89540-7, £ 155.00; Vol. 2: ISBN 0-471-88786-2, £ 155.00. *Acta Polymerica* **1986**, *37* (6), 396–397. https://doi.org/10.1002/actp.1986.010370618.

(53) McArdle, C. B. *Side Chain Liquid Crystal Polymers*; Springer Science & Business Media, 1990.

(54) Rau, H.; Lueddecke, E. On the Rotation-Inversion Controversy on Photoisomerization of Azobenzenes. Experimental Proof of Inversion. 5.

(55) Crecca, C. R.; Roitberg, A. E. Theoretical Study of the Isomerization Mechanism of Azobenzene and Disubstituted Azobenzene Derivatives. *Journals of Physical Chemistry A* **2006**, *110* (26), 8188–8203. https://doi.org/10.1021/jp057413c.

(56) Magee, J. L.; Shand, W.; Eyring, H. Non-Adiabatic Reactions. Rotation about the Double Bond *. *Journal of the American Chemical Society* **1941**, *63* (3), 677–688. https://doi.org/10.1021/ja01848a012.

(57) Curtin, D. Y.; Grubbs, E. J.; McCarty, C. G. Uncatalyzed Syn-Anti Isomerization of Imines, Oxime Ethers, and Haloimines [1]. *Journal of the American Chemical Society* **1966**, *88* (12), 2775–2786. https://doi.org/10.1021/ja00964a029.

(58) Bandara, H. M. D.; Burdette, S. C. Photoisomerization in Different Classes of Azobenzene. *Chemical Society Reviews* **2012**, *41* (5), 1809–1825. https://doi.org/10.1039/C1CS15179G.

(59) Mitscherlich, E. Ueber Das Stickstoffbenzid. *Annalen der Physik* **1834**, *108* (15), 225–227. https://doi.org/10.1002/andp.18341081502.

(60) Hartley, G. S. The Cis-Form of Azobenzene. *Nature* **1937**, *140* (3537), 281–281. https://doi.org/10.1038/140281a0.

(61) Merino, E.; Ribagorda, M. Control over Molecular Motion Using the Cis–Trans Photoisomerization of the Azo Group. *Beilstein Journal of Organic Chemistry* **2012**, *8* (1), 1071–1090. https://doi.org/10.3762/bjoc.8.119.

(62) H, R. Photochromism. *Molecules and Systems* **1990**.

(63) Tiberio, G.; Muccioli, L.; Berardi, R.; Zannoni, C. How Does the Trans–Cis Photoisomerization of Azobenzene Take Place in Organic Solvents? *ChemPhysChem* **2010**, *11* (5), 1018–1028. https://doi.org/10.1002/cphc.200900652.

(64) Dokić, J.; Gothe, M.; Wirth, J.; Peters, M. V.; Schwarz, J.; Hecht, S.; Saalfrank, P. Quantum Chemical Investigation of Thermal Cis-to-Trans Isomerization of Azobenzene Derivatives: Substituent Effects, Solvent Effects, and Comparison to Experimental Data. *Journal of Physical Chemistry A* **2009**, *113* (24), 6763–6773. https://doi.org/10.1021/jp9021344.

(65) Fliegl, H.; Köhn, A.; Hättig, C.; Ahlrichs, R. Ab Initio Calculation of the Vibrational and Electronic Spectra of Trans- and Cis-Azobenzene. *Journal of the American Chemical Society* **2003**, *125* (32), 9821–9827. https://doi.org/10.1021/ja034433o.

(66) Beharry, A. A.; Woolley, G. A. Azobenzene Photoswitches for Biomolecules. *Chemical Society Reviews* **2011**, *40* (8), 4422. https://doi.org/10.1039/c1cs15023e.

(67) Dias, A. R.; Minas Da Piedade, M. E.; Martinho Simões, J. A.; Simoni, J. A.; Teixeira, C.; Diogo, H. P.; Meng-Yan, Y.; Pilcher, G. Enthalpies of Formation of Cis-Azobenzene and Trans-Azobenzene. *The Journal of Chemical Thermodynamics* **1992**, *24* (4), 439–447. https://doi.org/10.1016/S0021-9614(05)80161-2.

(68) Yitzchaik, S.; Marks, T. J. Chromophoric Self-Assembled Superlattices. *Accounts of Chemical Research* **1996**, *29* (4), 197–202. https://doi.org/10.1021/ar9501582.

(69) Levy, D.; Esquivias, L. Sol–Gel Processing of Optical and Electrooptical Materials. *Advanced Materials* **1995**, *7* (2), 120–129. https://doi.org/10.1002/adma.19950070204.

(70) Sisido, M.; Ishikawa, Y.; Itoh, K.; Tazuke, S. Helically Arranged Azobenzene Chromophores along a Polypeptide Chain. 1. Synthesis and Circular Dichroism. *Macromolecules* **1991**, *24* (14), 3993–3998. https://doi.org/10.1021/ma00014a004.

(71) Willner, I.; Rubin, S. Control of the Structure and Functions of Biomaterials by Light. *Angewandte Chemie International Edition in English* **1996**, *35* (4), 367–385. https://doi.org/10.1002/anie.199603671.

(72) Gallot, B.; Fafiotte, M.; Fissi, A.; Pieroni, O. Liquid-Crystalline Structure of Poly(L-Lysine) Containing Azobenzene Units in the Side Chain. *Macromolecular Rapid Communications* **1996**, *17* (8), 493–501. https://doi.org/10.1002/marc.1996.030170801.

(73) Shinkai, S.; Minami, T.; Kusano, Y.; Manabe, O. Photoresponsive Crown Ethers. 8. Azobenzenophane-Type Switched-on Crown Ethers Which Exhibit an All-or-Nothing Change in Ion-Binding Ability. *Journal of the American Chemical Society* **1983**, *105* (7), 1851–1856. https://doi.org/10.1021/ja00345a029.

(74) Jung, J. H.; Takehisa, C.; Sakata, Y.; Kaneda, T. P-(4-Nitrophenylazo)Phenol Dye-Bridged Permethylated α-Cyclodextrin Dimer: Synthesis and Self-Aggregation in Dilute Aqueous Solution. *Chemistry Letters* **1996**, *25* (2), 147–148. https://doi.org/10.1246/cl.1996.147.

(75) Yamamura, H.; Kawai, H.; Yotsuya, T.; Higuchi, T.; Butsugan, Y.; Araki, S.; Kawai, M.; Fujita, K. A Cyclodextrin Derivative with Cation Carrying Ability: Heptakis(3,6-Anhydro)-β-Cyclodextrin 2-O-p-Phenylazobenzoate. *Chemistry Letters* **1996**, *25* (9), 799–800. https://doi.org/10.1246/cl.1996.799.

(76) Singh, A. K.; Das, J.; Majumdar, N. Novel Bacteriorhodopsin Analogues Based on Azo Chromophores. *Journal of the American Chemical Society* **1996**, *118* (26), 6185–6191. https://doi.org/10.1021/ja954286x.

(77) Chen, S. H.; Mastrangelo, J. C.; Shi, H.; Bashir-Hashemi, A.; Li, J.; Gelber, N. Novel Glass-Forming Organic Materials. 1. Adamantane with Pendant Cholesteryl, Disperse Red 1, and Nematogenic Groups. *Macromolecules* **1995**, *28* (23), 7775–7778. https://doi.org/10.1021/ma00127a026.

(78) Chen, S. H.; Mastrangelo, J. C.; Shi, H.; Blanton, T. N.; Bashir-Hashemi, A. Novel Glass-Forming Organic Materials. 3. Cubane with Pendant Nematogens, Carbazole, and Disperse Red 1. *Macromolecules* **1997**, *30* (1), 93–97. https://doi.org/10.1021/ma961115j.

(79) Li, C.; Lo, C.-W.; Zhu, D.; Li, C.; Liu, Y.; Jiang, H. Synthesis of a Photoresponsive Liquid-Crystalline Polymer Containing Azobenzene. *Macromolecular Rapid Communications* **2009**, *30* (22), 1928–1935. https://doi.org/10.1002/marc.200900421.

(80) Zhao, M.; Li, B.; Wang, P.; Lu, L.; Zhang, Z.; Liu, L.; Wang, S.; Li, D.; Wang, R.; Zhang, F. Supramolecularly Engineered NIR-II and Upconversion Nanoparticles In Vivo Assembly and Disassembly to Improve Bioimaging. *Advanced Materials* **2018**, *30* (52), 1804982. https://doi.org/10.1002/adma.201804982.

(81) Qu, D.-H.; Wang, Q.-C.; Zhang, Q.-W.; Ma, X.; Tian, H. Photoresponsive Host–Guest Functional Systems. *Chemistry Reviews* **2015**, *115* (15), 7543–7588. https://doi.org/10.1021/cr5006342.

(82) Broichhagen, J.; Jurastow, I.; Iwan, K.; Kummer, W.; Trauner, D. Optical Control of Acetylcholinesterase with a Tacrine Switch. *Angewandte Chemie International Edition* **2014**, *53* (29), 7657–7660. https://doi.org/10.1002/anie.201403666.

(83) Chi, X.; Ji, X.; Xia, D.; Huang, F. A Dual-Responsive Supra-Amphiphilic Polypseudorotaxane Constructed from a Water-Soluble Pillar[7]Arene and an Azobenzene-Containing Random Copolymer. *Journal of the American Chemical Society* **2015**, *137* (4), 1440–1443. https://doi.org/10.1021/ja512978n.

(84) Lubbe, A. S.; Szymanski, W.; Feringa, B. L. Recent Developments in Reversible Photoregulation of Oligonucleotide Structure and Function. *Chemical Society Reviews* **2017**, *46* (4), 1052–1079. https://doi.org/10.1039/C6CS00461J.

(85) Zhang, J.; Ma, W.; He, X.-P.; Tian, H. Taking Orders from Light: Photo-Switchable Working/Inactive Smart Surfaces for Protein and Cell Adhesion. *ACS Applied Materials Interfaces* **2017**, *9* (10), 8498–8507. https://doi.org/10.1021/acsami.6b15599.

(86) Broichhagen, J.; Podewin, T.; Meyer-Berg, H.; von Ohlen, Y.; Johnston, N. R.; Jones, B. J.; Bloom, S. R.; Rutter, G. A.; Hoffmann-Röder, A.; Hodson, D. J.; Trauner, D. Optical Control of Insulin Secretion Using an Incretin Switch. *Angewandte Chemie International Edition* **2015**, *54* (51), 15565–15569. https://doi.org/10.1002/anie.201506384.

(87) Cheng, H.-B.; Zhang, S.; Qi, J.; Liang, X.-J.; Yoon, J. Advances in Application of Azobenzene as a Trigger in Biomedicine: Molecular Design and Spontaneous Assembly. *Advanced Materials* **2021**, *33* (26), 2007290. https://doi.org/10.1002/adma.202007290.

(88) Wang, J.; Song, Q.; Guo, X.; Cui, X.; Tan, L.; Dong, L. Precise Cross-Dimensional Regulation of the Structure of a Photoreversible DNA Nanoswitch. *Analytical Chemistry* **2019**, *91* (22), 14530–14537. https://doi.org/10.1021/acs.analchem.9b03547.

(89) Srinivasan, B.; Forouhar, F.; Shukla, A.; Sampangi, C.; Kulkarni, S.; Abashidze, M.; Seetharaman, J.; Lew, S.; Mao, L.; Acton, T. B.; Xiao, R.; Everett, J. K.; Montelione, G. T.; Tong, L.; Balaram, H. Allosteric Regulation and Substrate Activation in Cytosolic Nucleotidase II from Legionella Pneumophila. *The FEBS Journal* **2014**, *281* (6), 1613–1628. https://doi.org/10.1111/febs.12727.

(90) Ikeda, T.; Mamiya, J.; Yu, Y. Photomechanics of Liquid-Crystalline Elastomers and Other Polymers. *Angewandte Chemie International Edition* **2007**, *46* (4), 506–528. https://doi.org/10.1002/anie.200602372.

(91) Li, M.-H.; Keller, P.; Li, B.; Wang, X.; Brunet, M. Light-Driven Side-On Nematic Elastomer Actuators. *Advanced Materials* **2003**, *15* (7–8), 569–572. https://doi.org/10.1002/adma.200304552.

(92) Camacho-Lopez, M.; Finkelmann, H.; Palffy-Muhoray, P.; Shelley, M. Fast Liquid-Crystal Elastomer Swims into the Dark. *Nature Materials* **2004**, *3* (5), 307–310. https://doi.org/10.1038/nmat1118.

(93) Wang, J.; Jiang, Q.; Hao, X.; Yan, H.; Peng, H.; Xiong, B.; Liao, Y.; Xie, X. Reversible Photo-Responsive Gel–Sol Transitions of Robust Organogels Based on an Azobenzene-Containing Main-Chain Liquid Crystalline Polymer. *RSC Advances* **2020**, *10* (7), 3726–3733. https://doi.org/10.1039/C9RA10161F.

(94) Linkov, I.; Bates, M. E.; Canis, L. J.; Seager, T. P.; Keisler, J. M. A Decision-Directed Approach for Prioritizing Research into the Impact of Nanomaterials on the Environment and Human Health. *Nature Nanotechnology* **2011**, *6* (12), 784–787. https://doi.org/10.1038/nnano.2011.163.

(95) Colvin, V. L. The Potential Environmental Impact of Engineered Nanomaterials. *Nature Biotechnology* **2003**, *21* (10), 1166–1170. https://doi.org/10.1038/nbt875.

(96) Ishihara, K.; Hamada, N.; Kato, S.; Shinohara, I. Photoinduced Swelling Control of Amphiphilic Azoaromatic Polymer Membrane. *Journal of Polymer Science: Polymer Chemistry Edition* **1984**, *22* (1), 121–128. https://doi.org/10.1002/pol.1984.170220112.

(97) Ishihara, K.; Matsuo, T.; Tsunemitsu, K.; Shinohara, I.; Negishi, N. Photoinduced Reversible PH Change in Aqueous Solution of Azoaromatic Poly(Carboxylic Acid). *Journal of Polymer Science: Polymer Chemistry Edition* **1984**, *22* (12), 3687–3695. https://doi.org/10.1002/pol.1984.170221206.

(98) Yamamoto, H.; Nishida, A. Light-Induced Reversible Conformational Changes in Poly(L-Lysine) with Photochromic Side Chains. *Macromolecules* **1986**, *19* (3), 943–944. https://doi.org/10.1021/ma00157a085.

(99) Crawford, R. L. *Lignin Biodegradation and Transformation*; Wiley, 1981.

(100) Updegraff, D. M. Semimicro Determination of Cellulose Inbiological Materials. *Analytical Biochemistry* **1969**, *32* (3), 420–424. https://doi.org/10.1016/S0003-2697(69)80009-6.

(101) Ebrahimi, E.; Babaeipour, V.; Meftahi, A.; Alibakhshi, S. Effects of Bio-Production Process Parameters on Bacterial Cellulose Mechanical Properties. *Journal of Chemical Engineering of Japan* **2017**, *50* (11), 857–861. https://doi.org/10.1252/jcej.15we301.

(102) Klemm, D.; Heublein, B.; Fink, H.-P.; Bohn, A. Cellulose: Fascinating Biopolymer and Sustainable Raw Material. *Angewandte Chemie International Edition* **2005**, *44* (22), 3358–3393. https://doi.org/10.1002/anie.200460587.

(103) Cai, G.; Ciou, J.-H.; Liu, Y.; Jiang, Y.; Lee, P. S. Leaf-Inspired Multiresponsive MXene-Based Actuator for Programmable Smart Devices. *Science Advances* **2019**, *5* (7), eaaw7956. https://doi.org/10.1126/sciadv.aaw7956.

(104) Arai, K.; Udagawa, H. Application of Photoresponsive Groups-Containing Cellulose as an Adsorbent for Thin Layer Chromatography. *Die Makromolekulare Chemie, Rapid Communications* **1988**, *9* (12), 797–800. https://doi.org/10.1002/marc.1988.030091203.

(105) Arai, K.; Udagawa, H. Influence of DP of Cellulose Backbone on Liquid Crystalline Phase of Cellulose P-Phenylazobenzoate. *Sen-i Gakkaishi* **1990**, *46* (11), 491–495. https://doi.org/10.2115/fiber.46.11_491.

(106) *ATR-FTIR Spectroscopy, FTIR Sampling Techniques | Agilent*. https://www.agilent.com/en/product/molecular-spectroscopy/ftir-spectroscopy/atr-ftir-spectroscopy (accessed 2022-09-20).

(107) *Varian Cary 50 Bio UV-Visible Spectrophotometer*. https://americanlaboratorytrading.com/lab-equipment-products/varian-cary-50-bio-uv-visible-spectrophotometer_6069 (accessed 2022-10-03).

(108) Gómez-Carracedo, A.; Alvarez-Lorenzo, C.; Gómez-Amoza, J. L.; Concheiro, A. Chemical Structure and Glass Transition Temperature of Non-Ionic Cellulose Ethers. *Journal of Thermal Analysis and Calorimetry* **2003**, *73* (2), 587–596. https://doi.org/10.1023/A:1025434314396.

(109) Kondo, T. The Relationship between Intramolecular Hydrogen Bonds and Certain Physical Properties of Regioselectively Substituted Cellulose Derivatives. *Journal of Polymer Science Part B: Polymer Physics* **1997**, *35* (4), 717–723. https://doi.org/10.1002/(SICI)1099-0488(199703)35:4<717::AID-POLB18>3.0.CO;2-J.

(110) Kondo, T. Hydrogen Bonds in Regioselectively Substituted Cellulose Derivatives. *Journal of Polymer Science Part B: Polymer Physics* **1994**, *32* (7), 1229–1236. https://doi.org/10.1002/polb.1994.090320710.

(111) Kondo, T.; Sawatari, C. Intermolecular Hydrogen Bonding in Cellulose/Poly(Ethylene Oxide) Blends: Thermodynamic Examination Using 2,3-Di-O- and 6-O-Methylcelluloses as Cellulose Model Compounds. *Polymer* **1994**, *35* (20), 4423–4428. https://doi.org/10.1016/0032-3861(94)90102-3.

(112) Kondo, T.; Sawatari, C. A Fourier Transform Infra-Red Spectroscopic Analysis of the Character of Hydrogen Bonds in Amorphous Cellulose. *Polymer* **1996**, *37* (3), 393–399. https://doi.org/10.1016/0032-3861(96)82908-9.

(113) Kondo, T.; Sawatari, C.; Manley, R. St. J.; Gray, D. G. Characterization of Hydrogen Bonding in Cellulose-Synthetic Polymer Blend Systems with Regioselectively Substituted Methylcellulose. *Macromolecules* **1994**, *27* (1), 210–215. https://doi.org/10.1021/ma00079a031.

(114) Ziabicki, A. *Fundamentals of Fibre Formation: The Science of Fibre Spinning and Drawing*; Wiley, 1976.

(115) Khajavi, R.; Abbasipour, M. Electrospinning as a Versatile Method for Fabricating Coreshell, Hollow and Porous Nanofibers. *Scientia Iranica* **2012**, *19* (6), 2029–2034. https://doi.org/10.1016/j.scient.2012.10.037.

(116) Frey, M. W. Electrospinning Cellulose and Cellulose Derivatives. *Polymer Reviews* **2008**, *48* (2), 378–391. https://doi.org/10.1080/15583720802022281.

(117) Forouharshad, M.; Saligheh, O.; Arasteh, R.; Farsani, R. E. Manufacture and Characterization of Poly (Butylene Terephthalate) Nanofibers by Electrospinning. *Journal of Macromolecular Science, Part B* **2010**, *49* (4), 833–842. https://doi.org/10.1080/00222341003609377.

(118) Lancuški, A.; Fort, S.; Bossard, F. Electrospun Azido-PCL Nanofibers for Enhanced Surface Functionalization by Click Chemistry. *ACS Applied Materials Interfaces* **2012**, *4* (12), 6499–6504. https://doi.org/10.1021/am301458y.

(119) Bourourou, M.; Holzinger, M.; Bossard, F.; Hugenell, F.; Maaref, A.; Cosnier, S. Chemically Reduced Electrospun Polyacrilonitrile–Carbon Nanotube Nanofibers Hydrogels as Electrode Material

for Bioelectrochemical Applications. *Carbon* **2015**, *87*, 233–238. https://doi.org/10.1016/j.carbon.2015.02.026.

(120) Celebioglu, A.; Demirci, S.; Uyar, T. Cyclodextrin-Grafted Electrospun Cellulose Acetate Nanofibers via "Click" Reaction for Removal of Phenanthrene. *Applied Surface Science* **2014**, *305*, 581–588. https://doi.org/10.1016/j.apsusc.2014.03.138.

(121) Nicosia, A.; Keppler, T.; Müller, F. A.; Vazquez, B.; Ravegnani, F.; Monticelli, P.; Belosi, F. Cellulose Acetate Nanofiber Electrospun on Nylon Substrate as Novel Composite Matrix for Efficient, Heat-Resistant, Air Filters. *Chemical Engineering Science* **2016**, *153*, 284–294. https://doi.org/10.1016/j.ces.2016.07.017.

(122) Inukai, S.; Kurokawa, N.; Hotta, A. Annealing and Saponification of Electrospun Cellulose-Acetate Nanofibers Used as Reinforcement Materials for Composites. *Composites Part A: Applied Science and Manufacturing* **2018**, *113*, 158–165. https://doi.org/10.1016/j.compositesa.2018.07.028.

(123) Tidjarat, S.; Winotapun, W.; Opanasopit, P.; Ngawhirunpat, T.; Rojanarata, T. Uniaxially Aligned Electrospun Cellulose Acetate Nanofibers for Thin Layer Chromatographic Screening of Hydroquinone and Retinoic Acid Adulterated in Cosmetics. *Journal of Chromatography A* **2014**, *1367*, 141–147. https://doi.org/10.1016/j.chroma.2014.09.043.

(124) Ma, W.; Guo, Z.; Zhao, J.; Yu, Q.; Wang, F.; Han, J.; Pan, H.; Yao, J.; Zhang, Q.; Samal, S. K.; De Smedt, S. C.; Huang, C. Polyimide/Cellulose Acetate Core/Shell Electrospun Fibrous Membranes for Oil-Water Separation. *Separation and Purification Technology* **2017**, *177*, 71–85. https://doi.org/10.1016/j.seppur.2016.12.032.

(125) Ismail, N.; Junior Maksoud, F.; Ghaddar, N.; Ghali, K.; Tehrani-Bagha, A. A Mathematical Model to Predict the Effect of Electrospinning Processing Parameters on the Morphological Characteristic of Nano-Fibrous Web and Associated Filtration Efficiency. *Journal of Aerosol Science* **2017**, *113*, 227–241. https://doi.org/10.1016/j.jaerosci.2017.08.013.

(126) Badmus, M.; Liu, J.; Wang, N.; Radacsi, N.; Zhao, Y. Hierarchically Electrospun Nanofibers and Their Applications: A Review. *Nano Materials Science* **2021**, *3* (3), 213–232. https://doi.org/10.1016/j.nanoms.2020.11.003.

(127) Shi, X.; Zhou, W.; Ma, D.; Ma, Q.; Bridges, D.; Ma, Y.; Hu, A. Electrospinning of Nanofibers and Their Applications for Energy Devices. *Journal of Nanomaterials* **2015**, *16* (1), 122:122. https://doi.org/10.1155/2015/140716.

(128) Huang, C.-L.; Wang, P.-Y.; Li, Y.-Y. Fabrication of Electrospun CO2 Adsorption Membrane for Zinc-Air Battery Application. *Chemical Engineering Journal* **2020**, *395*, 125031. https://doi.org/10.1016/j.cej.2020.125031.

(129) Thenmozhi, S.; Dharmaraj, N.; Kadirvelu, K.; Kim, H. Y. Electrospun Nanofibers: New Generation Materials for Advanced Applications. *Materials Science and Engineering: B* **2017**, *217*, 36–48. https://doi.org/10.1016/j.mseb.2017.01.001.

(130) Mahdavi, M.; Mahmoudi, N.; Anaran, F. R.; Simchi, A. Electrospinning of Nanodiamond-Modified Polysaccharide Nanofibers with Physico-Mechanical Properties Close to Natural Skins. *Marine Drugs* **2016**, *14* (7), 128. https://doi.org/10.3390/md14070128.

(131) Stevanovic, D. Mode I and Mode II Delamination Properties of Glass/Vinyl-Ester Composite Toughened by Particulate Modified Interlayers. *Composites Science and Technology* **2003**, *63* (13), 1949–1964. https://doi.org/10.1016/S0266-3538(03)00162-3.

(132) Khashaba, U. A.; Sebaey, T. A.; Alnefaie, K. A. Failure and Reliability Analysis of Pinned-Joints Composite Laminates: Effects of Stacking Sequences. *Composites Part B: Engineering* **2013**, *45* (1), 1694–1703. https://doi.org/10.1016/j.compositesb.2012.09.066.

(133) 14:00-17:00. *ISO 13934-1:2013*. ISO. https://www.iso.org/cms/render/live/en/sites/isoorg/contents/data/standard/06/06/60676.html (accessed 2022-09-20).

(134) Fryer, C.; Scharnagl, M.; Helms, C. Electrostatic Alignment of Electrospun PEO Fibers by the Gap Method Increases Individual Fiber Modulus in Comparison to Non-Aligned Fibers of Similar Diameter. *AIP Advances* **2018**, *8* (6), 065023. https://doi.org/10.1063/1.5027812.

(135) Ube, T.; Ikeda, T. Photomobile Polymer Materials with Crosslinked Liquid-Crystalline Structures: Molecular Design, Fabrication, and Functions. *Angewandte Chemie International Edition* **2014**, *53* (39), 10290–10299. https://doi.org/10.1002/anie.201400513.

(136) Yu, H.; Ikeda, T. Photocontrollable Liquid-Crystalline Actuators. *Advanced Materials* **2011**, *23* (19), 2149–2180. https://doi.org/10.1002/adma.201100131.

(137) White, T. J.; Broer, D. J. Programmable and Adaptive Mechanics with Liquid Crystal Polymer Networks and Elastomers. *Nature Materials* **2015**, *14* (11), 1087–1098. https://doi.org/10.1038/nmat4433.

(138) Li, M.-H.; Keller, P. Artificial Muscles Based on Liquid Crystal Elastomers. *Philosophical Transactions of the Royal Society A* **2006**, *364* (1847), 2763–2777. https://doi.org/10.1098/rsta.2006.1853.

(139) Ohm, C.; Brehmer, M.; Zentel, R. Liquid Crystalline Elastomers as Actuators and Sensors. *Advanced Materials* **2010**, *22* (31), 3366–3387. https://doi.org/10.1002/adma.200904059.

(140) Ikeda, T.; Ube, T. Photomobile Polymer Materials: From Nano to Macro. *Materials Today* **2011**, *14* (10), 480–487. https://doi.org/10.1016/S1369-7021(11)70212-7.

(141) Yang, H.; Ye, G.; Wang, X.; Keller, P. Micron-Sized Liquid Crystalline Elastomer Actuators. *Soft Matter* **2011**, *7* (3), 815–823. https://doi.org/10.1039/C0SM00734J.

(142) Jiang, H.; Li, C.; Huang, X. Actuators Based on Liquid Crystalline Elastomer Materials. *Nanoscale* **2013**, *5* (12), 5225. https://doi.org/10.1039/c3nr00037k.

(143) Li, S.; Tu, Y.; Bai, H.; Hibi, Y.; Wiesner, L. W.; Pan, W.; Wang, K.; Giannelis, E. P.; Shepherd, R. F. Simple Synthesis of Elastomeric Photomechanical Switches That Self-Heal. *Macromolecular Rapid Communications* **2019**, *40* (4), 1800815. https://doi.org/10.1002/marc.201800815.

(144) Zhang, P.; Lan, Z.; Wei, J.; Yu, Y. Photodeformable Azobenzene-Containing Polyimide with Flexible Linkers and Molecular Alignment. *ACS Macro Letters* **2021**, *10* (4), 469–475. https://doi.org/10.1021/acsmacrolett.1c00040.

(145) Sun, S.; Liang, S.; Xu, W.-C.; Xu, G.; Wu, S. Photoresponsive Polymers with Multi-Azobenzene Groups. *Polymer Chemistry* **2019**, *10* (32), 4389–4401. https://doi.org/10.1039/C9PY00793H.

(146) Wang, S.; Song, Y.; Jiang, L. Photoresponsive Surfaces with Controllable Wettability. *Journal of Photochemistry and Photobiology C: Photochemistry Reviews* **2007**, *8* (1), 18–29. https://doi.org/10.1016/j.jphotochemrev.2007.03.001.

(147) Siewierski, L. M.; Brittain, W. J.; Petrash, S.; Foster, M. D. Photoresponsive Monolayers Containing In-Chain Azobenzene. *Langmuir* **1996**, *12* (24), 5838–5844. https://doi.org/10.1021/la960506o.

(148) Delorme, N.; Bardeau, J.-F.; Bulou, A.; Poncin-Epaillard, F. Azobenzene-Containing Monolayer with Photoswitchable Wettability. *Langmuir* **2005**, *21* (26), 12278–12282. https://doi.org/10.1021/la051517x.

(149) Pinto, L. F. V.; Kundu, S.; Brogueira, P.; Cruz, C.; Fernandes, S. N.; Aluculesei, A.; Godinho, M. H. Cellulose-Based Liquid Crystalline Photoresponsive Films with Tunable Surface Wettability. *Langmuir* **2011**, *27* (10), 6330–6337. https://doi.org/10.1021/la200422q.

(150) Huang, Y.; Kang, H.; Li, G.; Wang, C.; Huang, Y.; Liu, R. Synthesis and Photosensitivity of Azobenzene Functionalized Hydroxypropylcellulose. *RSC Advances* **2013**, *3*, 15909–15916. https://doi.org/10.1039/C3RA43031F.

(151) Erdmenger, T.; Haensch, C.; Hoogenboom, R.; Schubert, U. S. Homogeneous Tritylation of Cellulose in 1-Butyl-3-Methylimidazolium Chloride. *Macromolecular Bioscience* **2007**, *7* (4), 440–445. https://doi.org/10.1002/mabi.200600253.

(152) Dupont, A.-L.; Mortha, G. Comparative Evaluation of Size-Exclusion Chromatography and Viscometry for the Characterisation of Cellulose. *Journal of Chromatography A* **2004**, *1026* (1–2), 129–141. https://doi.org/10.1016/j.chroma.2003.11.002.

(153) Erler, U.; Klemm, D.; Nehls, I. Homogeneous Synthesis of Diphenylmethyl Ethers of Cellulose in N,N-Dimethylacetamide/LiCl Solvent System. *Die Makromolekulare Chemie, Rapid Communications* **1992**, *13* (4), 195–201. https://doi.org/10.1002/marc.1992.030130401.

(154) Gömez, J. A. C.; Erler, U. W.; Klemm, D. O. 4-Methoxy Substituted Trityl Groups in 6-O Protection of Cellulose: Homogeneous Synthesis, Characterization, Detritylation. *Macromolecular Chemistry and Physics* **1996**, *197* (3), 953–964. https://doi.org/10.1002/macp.1996.021970316.

(155) Heinze, T.; Schwikal, K.; Barthel, S. Ionic Liquids as Reaction Medium in Cellulose Functionalization. *Macromolecular Bioscience* **2005**, *5* (6), 520–525. https://doi.org/10.1002/mabi.200500039.

(156) Gale, R. J.; Gilbert, B.; Osteryoung, R. A. Raman Spectra of Molten Aluminum Chloride: 1-Butylpyridinium Chloride Systems at Ambient Temperatures. *Inorganic Chemistry* **1978**, *17* (10), 2728–2729. https://doi.org/10.1021/ic50188a008.

(157) Wilkes, J. S.; Levisky, J. A.; Wilson, R. A.; Hussey, C. L. Dialkylimidazolium Chloroaluminate Melts: A New Class of Room-Temperature Ionic Liquids for Electrochemistry, Spectroscopy and Synthesis. *Inorganic Chemistry* **1982**, *21* (3), 1263–1264. https://doi.org/10.1021/ic00133a078.

(158) Swatloski, R. P.; Spear, S. K.; Holbrey, J. D.; Rogers, R. D. Dissolution of Cellose with Ionic Liquids. *Journal of the American Chemical Society* **2002**, *124* (18), 4974–4975. https://doi.org/10.1021/ja025790m.

(159) Liebert, T.; Heinze, T. INTERACTION OF IONIC LIQUIDS WITH POLYSACCHARIDES. 5. SOLVENTS AND REACTION MEDIA FOR THE MODIFICATION OF CELLULOSE. *BioResources* **2008**, *3* (2), 576–601.

(160) Sescousse, R.; Le, K. A.; Ries, M. E.; Budtova, T. Viscosity of Cellulose−Imidazolium-Based Ionic Liquid Solutions. *Journal of Physical Chemistry B* **2010**, *114* (21), 7222–7228. https://doi.org/10.1021/jp1024203.

(161) Gericke, M.; Schlufter, K.; Liebert, T.; Heinze, T.; Budtova, T. Rheological Properties of Cellulose/Ionic Liquid Solutions: From Dilute to Concentrated States. *Biomacromolecules* **2009**, *10* (5), 1188–1194. https://doi.org/10.1021/bm801430x.

(162) Lv, Y.; Chen, Y.; Shao, Z.; Zhang, R.; Zhao, L. Homogeneous Tritylation of Cellulose in 1-Allyl-3-Methylimidazolium Chloride and Subsequent Acetylation: The Influence of Base. *Carbohydrate Polymers* **2015**, *117*, 818–824. https://doi.org/10.1016/j.carbpol.2014.10.041.

(163) Klemm, D.; Heinze, T.; Philipp, B.; Wagenknecht, W. New Approaches to Advanced Polymers by Selective Cellulose Functionalization. *Acta Polymerica* **1997**, *48* (8), 277–297. https://doi.org/10.1002/actp.1997.010480801.

(164) Heinze, T. J.; Erler, U.; Klemm, D. 21 - Investigations on Homogeneous Synthesis of Carboxy Group-Containing Cellulose Derivatives and the Determination of the Substituent Distribution Using HPLC. In *Cellulose and Cellulose Derivatives*; Kennedy, J. F., Phillips, G. O., Williams, P. A., Eds.; Woodhead Publishing, 1995; pp 161–168. https://doi.org/10.1533/9781845698539.3.161.

(165) Hearon, W. M.; Hiatt, G. D.; Fordyce, C. R. *Cellulose Trityl Ether1a*. ACS Publications. https://pubs.acs.org/doi/pdf/10.1021/ja01252a064 (accessed 2022-09-21). https://doi.org/10.1021/ja01252a064.

(166) Koschella, A.; Fenn, D.; Illy, N.; Heinze, T. Regioselectively Functionalized Cellulose Derivatives: A Mini Review. *Macromolecular Symposia* **2006**, *244* (1), 59–73. https://doi.org/10.1002/masy.200651205.

(167) Cantero, D. A.; Sánchez Tapia, Á.; Bermejo, M. D.; Cocero, M. J. Pressure and Temperature Effect on Cellulose Hydrolysis in Pressurized Water. *Chemical Engineering Journal* **2015**, *276*, 145–154. https://doi.org/10.1016/j.cej.2015.04.076.

(168) Tosh, B.; Saikia, C. N.; Dass, N. N. Homogeneous Esterification of Cellulose in the Lithium Chloride–N,N-Dimethylacetamide Solvent System: Effect of Temperature and Catalyst. *Carbohydrate Research* **2000**, *327* (3), 345–352. https://doi.org/10.1016/S0008-6215(00)00033-1.

(169) Frilette, V. J.; Hanle, J.; Mark, H. Rate of Exchange of Cellulose with Heavy Water. *Journal of the American Chemical Society* **1948**, *70* (3), 1107–1113. https://doi.org/10.1021/ja01183a071.

(170) Hajaligol, M. R.; Howard, J. B.; Longwell, J. P.; Peters, W. A. Product Compositions and Kinetics for Rapid Pyrolysis of Cellulose. *Industrial and Engineering Chemistry Process Design and Development* **1982**, *21* (3), 457–465. https://doi.org/10.1021/i200018a019.

(171) Zhuang, G.-L.; Wey, M.-Y.; Tseng, H.-H. The Density and Crystallinity Properties of PPO-Silica Mixed-Matrix Membranes Produced via the in Situ Sol-Gel Method for H2/CO2 Separation. II: Effect of Thermal Annealing Treatment. *Chemical Engineering Research and Design* **2015**, *104*, 319–332. https://doi.org/10.1016/j.cherd.2015.08.020.

(172) Hu, J.; Li, X.; Ni, Y.; Ma, S.; Yu, H. A Programmable and Biomimetic Photo-Actuator: A Composite of a Photo-Liquefiable Azobenzene Derivative and Commercial Plastic Film. *Journal of Materials Chemistry C* **2018**, *6* (40), 10815–10821. https://doi.org/10.1039/C8TC03693D.

(173) Prasannalakshmi, P.; Shanmugam, N.; Kannadasan, N.; Sathishkumar, K.; Viruthagiri, G.; Poonguzhali, R. Influence of Thermal Annealing on the Photo Catalytic Properties of TiO2 Nanoparticles under Solar Irradiation. *Journal of Materials Sciences: Materials in Electronics* **2015**, *26* (10), 7987–7996. https://doi.org/10.1007/s10854-015-3453-x.

(174) Geng, J.; Mei, L.; Liang, Y.; Yuan, L.; Yu, J.; Hu, K.; Yuan, L.; Feng, W.; Chai, Z.; Shi, W. Controllable Photomechanical Bending of Metal-Organic Rotaxane Crystals Facilitated by

Regioselective Confined-Space Photodimerization. *Nature Communications* **2022**, *13* (1), 2030. https://doi.org/10.1038/s41467-022-29738-y.

(175) Porcu, P.; Estrada-Montaño, A. S.; Vonlanthen, M.; Cuétara-Guadarrama, F.; González-Méndez, I.; Sorroza-Martínez, K.; Zaragoza-Galán, G.; Rivera, E. Azobenzene Dyads Containing Fullerene, Porphyrin and Pyrene Chromophores: Molecular Design and Optical Properties. *Dyes and Pigments* **2022**, *197*, 109858. https://doi.org/10.1016/j.dyepig.2021.109858.

(176) *#Expelab // Zoom Vidéo Sur Une Manip' Scientifique !*; Ahmadi-Nohadani, H. **2021**. https://www.youtube.com/watch?v=hN-ZYgZ5rVs&t=3s&ab_channel=HauteursUGA

(177) Groten, J.; Bunte, C.; Rühe, J. Light-Induced Switching of Surfaces at Wetting Transitions through Photoisomerization of Polymer Monolayers. *Langmuir* **2012**, *28* (42), 15038–15046. https://doi.org/10.1021/la302764k.

(178) Paik, M. Y.; Krishnan, S.; You, F.; Li, X.; Hexemer, A.; Ando, Y.; Kang, S. H.; Fischer, D. A.; Kramer, E. J.; Ober, C. K. Surface Organization, Light-Driven Surface Changes, and Stability of Semifluorinated Azobenzene Polymers. *Langmuir* **2007**, *23* (9), 5110–5119. https://doi.org/10.1021/la0634138.

(179) Bobrovsky, A.; Ryabchun, A.; Shibaev, V. Liquid Crystals Photoalignment by Films of Side-Chain Azobenzene-Containing Polymers with Different Molecular Structure. *Journal of Photochemistry and Photobiology A: Chemistry* **2011**, *218* (1), 137–142. https://doi.org/10.1016/j.jphotochem.2010.12.013.

(180) Abrakhi, S.; Péralta, S.; Fichet, O.; Teyssié, D.; Cantin, S. Poly(Azobenzene Acrylate-Co-Fluorinated Acrylate) Spin-Coated Films: Influence of the Composition on the Photo-Controlled Wettability. *Langmuir* **2013**, *29* (30), 9499–9509. https://doi.org/10.1021/la400938j.

(181) Heinze, T.; Dicke, R.; Koschella, A.; Kull, A. H.; Klohr, E.-A.; Koch, W. Effective Preparation of Cellulose Derivatives in a New Simple Cellulose Solvent. *Macromolecular Chemistry and Physics* **2000**, *201* (6), 627–631. https://doi.org/10.1002/(SICI)1521-3935(20000301)201:6<627::AID-MACP627>3.0.CO;2-Y.

(182) Gräbner, D.; Liebert, T.; Heinze, T. Synthesis of Novel Adamantoyl Cellulose Using Differently Activated Carboxylic Acid Derivatives. *Cellulose* **2002**, *9* (2), 193–201. https://doi.org/10.1023/A:1020120427308.

(183) Goodlett, V. W.; Dougherty, J. T.; Patton, H. W. Characterization of Cellulose Acetates by Nuclear Magnetic Resonance. *Journal of Polymer Science Part A-1: Polymer Chemistry* **1971**, *9* (1), 155–161. https://doi.org/10.1002/pol.1971.150090114.

(184) Ahmadi-Nohadani, H. influence des conditions de fabrication sur les propriétés mécaniques d'un composite de fibres de lin uniderectionnelles/matrice polypropylène. *Master's thesis dissertation.* Ensait/Drive/Isat. **2019**.

(185) Xie J, Li X, Lipner J, Manning CN, Schwartz AG, Thomopoulos S, Xia Y. "Aligned-to-random" nanofiber scaffolds for mimicking the structure of the tendon-to-bone insertion site. *Nanoscale*. **2010**;2(6):923-6.

Abstract

A polysaccharide-based smart photo-actuator is fabricated *via* electrospinning of cellulose 4-phenyl azobenzoate (Azo-Cel) from its organic solution in a mixture of high-volatile acetone, a poor solvent of Azo-Cel, and low-volatile *N*,*N*-dimethylacetamide (DMAc), a good solvent of Azo-Cel. Stable electrified polymer jets are generated at an ideal polymer concentration (17 wt%) and solvent mixing ratio (acetone/DMAc = 3/2 (v/v)) so that continuous nanofibers can be drawn on a cylinder-shaped rotating drum electrode under a strong electric field (25 kV) and the non-woven fabric can be produced. The Azo-Cel fabric is confirmed to be made up of uniaxially aligned nanofibers *via* scanning electron microscopy. The water contact angle of the Azo-Cel fabric reversibly decreases and increases in response to alternate irradiation with UV and visible light to geometric deformation of the azobenzene moiety between the trans and cis isomers, resulting in lower and higher surface free energies, respectively. Furthermore, self-standing Azo-Cel fabric shows a photomechanical asymmetric bending deformation toward the light source caused by UV light. Regioselectively functionalized Azo-Cel was synthesized through protection of C6 of AGU by tritylation, then esterifying the C2 and C3 regions, then eventually deprotecting the C6 regions to obtain di-Azo-Cel. Although this method shows no change in WCA of the new product compared to Azo-Cel, the photo-responsive bending is heavily impacted and dampened probably due to a molar decrease of functionalized Azo side groups and the presence of –OH groups that form intramolecular hydrogen bonds.

Résumé

Un photo-actionneur intelligent à base de polysaccharide est fabriqué par électrofilage de 4-phényl azobenzoate de cellulose (Azo-Cel) à partir de sa solution organique dans un mélange d'acétone hautement volatile, qui est un solvant pauvre d'Azo-Cel, et de *N*,*N*-diméthylacétamide (DMAc), peu volatil mais bon solvant d'Azo-Cel. Des jets de polymère électrifiés stables sont générés à une concentration de polymère idéale (17 % en poids) et un rapport de mélange de solvants optimisé (acétone/DMAc = 3/2 (v/v)) afin que des nanofibres continues puissent être dessinées sur une électrode à tambour rotatif en forme de cylindre sous un fort champ électrique (25 kV), et ainsi un textile non-tissé peut être produit. Il est confirmé par microscopie électronique à balayage que le tissu à base d'Azo-Cel est composé de nanofibres uniaxialement alignées. L'angle de contact avec l'eau du tissu à base d'Azo-Cel diminue et augmente, de manière réversible, en réponse à une irradiation alternée avec la lumière UV et visible, comme suite à la déformation géométrique du motif azobenzène entre les isomères *trans* et *cis*, entraînant respectivement des énergies libres de surface basses et hautes. De plus, le tissu à base d'Azo-Cel autoportant présente une déformation de flexion asymétrique photomécanique en direction de la source lumineuse UV. De l'Azo-Cel régiosélectivement fonctionnalisée a été synthétisée par protection du C6 d'AGU par tritylation, puis estérification des régions C2 et C3, puis finalement déprotection du carbone C6 pour obtenir du di-Azo-Cel. Bien que cette espèce chimique ne montre aucun changement dans le WCA du nouveau produit par rapport à Azo-Cel, la flexion photosensible est fortement impactée et atténuée, possiblement en raison d'une diminution de masse molaire des groupes latéraux Azo fonctionnalisés, ainsi que de la présence des groupements –OH qui peuvent former des liaisons hydrogène intramoléculaires.